UNIVERSITY OF CALIFORNIA
Los Angeles

Electromagnetic Turbulence and Transport in Increased β LAPD Plasmas

A dissertation submitted in partial satisfaction
of the requirements for the degree
Doctor of Philosophy in Physics

by

Giovanni Di Gangi Rossi

2021

ABSTRACT OF THE DISSERTATION

Electromagnetic Turbulence and Transport
in
Increased β LAPD Plasmas

by

Giovanni Di Gangi Rossi
Doctor of Philosophy in Physics
University of California, Los Angeles, 2021
Professor Troy A Carter, Chair

The effect of increasing β on pressure-gradient driven turbulence and transport on the Large Plasma Device (LAPD) is explored for the first time. A recently installed $\mathrm{LaB_6}$ cathode source produces higher plasma pressure plasmas, which when used in conjunction with lowered magnetic field, enables access to moderate β values ($\sim 0.1-1$) while still maintaining ion magnetization. For this experiment the background magnetic field, B_0, is varied from 175G to 1000G, resulting in a plasma β range from $\approx 0.2\%$ up to $\approx 15\%$. Utilizing a wide array of magnetic and Langmuir probe diagnostics, the modification of plasma parameter profiles, fluctuation amplitudes, and radial transport are recorded at various β. From the scan, the magnitude of magnetic fluctuations is observed to increase substantially from $\delta B/B_0 \sim 0.06\%$ to $\delta B/B_0 \sim 1\%$ with increasing β. More importantly, parallel magnetic fluctuations are observed to dominate at higher β values, with $\delta B_{||}/\delta B_{\perp} \approx 2$ and $\delta B/B_0 \approx 1\%$. Parallel magnetic fluctuations are strongly correlated with density fluctuations and the relative magnitude and cross-phase between density and parallel magnetic field fluctuations is consistent with dynamic pressure balance ($P + \frac{B_0^2}{2\mu_0} = \text{constant}$). 2D cross-correlation analysis of the turbulent structure shows a global coherent low-m eigenmode that has strong perpendicular magnetic fluctuations localized to the core and parallel magnetic fluctuations localized to the density gradient region of the plasma. Polarization of the perpendicular magnetic field fluctuations is shown to be predominantly left-handed at low β and transitions to predominantly right-handed at higher β. Many of these observations are consistent with the characteristics of resistive drift-Alfvén waves as previously observed in LAPD. Thus one can hypothesize that the additional observations of parallel magnetic field fluctuations are modifications to resistive drift-Alfvén waves at higher β. In order to test this hypothesis, a local slab model theory for electromagnetic, modified drift Alfvén waves, including parallel magnetic fluctuations and diamagnetic corrections to the background field, is developed. Numerical solutions to the derived dispersion relation with experimental profile parameters are then computed to reveal growing modes. Tracking the fastest growing mode, comparisons of fluctuation amplitude ratios between the model and experimental observations show good agreement for for $\beta < 2\%$ while differences at higher β indicate that other mechanisms such as finite Larmor radius (FLR) effects may be becoming dominant.

The dissertation of Giovanni Di Gangi Rossi is approved.

Walter N Gekelman

Frank S Jenko

Marco CM Velli

Troy A Carter, Committee Chair

University of California, Los Angeles

2021

To Mike Meyers & the Number One Boys . . .
who—among so many other things—
helped me "do a good job" in physics
while still living the dream.

TABLE OF CONTENTS

LIST OF FIGURES

ACKNOWLEDGMENTS

While the journey to get to this point has been long and sometimes arduous, it has not been without the support and guidance from some of the best and brightest characters in my life. I am forever grateful for the experiences we have shared and honored to acknowledge them below.

I would first like to thank my advisor, Troy Carter, for being the best "physics dad" one could ever ask for. I am very lucky to find such an inspiring and knowledgeable advisor who could foster my growth as an experimental plasma physicist while I also experimented with different colors of hair dye. Thank you for always having my back and supporting my sometimes unconventional methods of conducting research (e.g. blue tape). I deeply appreciate all of the conferences and meetings that you enabled me to attend across the globe which was essential to my worldview today.

I want to acknowledge my PhD committee members - Walter Gekelman, Frank Jenko, and Marco Velli - for their review of this dissertation as well as the discussions on my research over the years. I will always remember my first APS-DPP conference in 2010, waking up early for the 8:00 am Monday talk that Walter gave. I was only an undergraduate at the time, but after witnessing the caliber of research and flair of showmanship Walter had while presenting data with 3D glasses, I was inspired to work my hardest to gain acceptance into UCLA for grad school.

I first came to UCLA as a volunteer while taking a year off from my undergraduate studies. Knowing very little about plasma physics, I was very fortunate to find myself under the wing of an older graduate student, my "physics older brother", David Schaffner. Thank you David for being my mentor and giving invaluable hands-on experience that taught me almost everything I know about running plasma experiments. Thank you also for bequeathing your beloved couch to me which would later become my second home during run weeks and studying for the comp.

I would also like to thank all the scientists and staff of BAPSF for their support and company throughout the years: Steve Vincena, for being the only one brave enough to admit he could code in LabVIEW and showing me how to balance physics and actual life; Shreekrishna Tripathi, for always staying late to help with opening ball valves and being a friendly face at the gym; Zoltan Lucky, for always knowing where to find the right tool and allowing me to fix my car in the loading dock on countless weekends; Marvin Drandell, for being a master manufacturer and always encouraging my passion projects; Pat Pribyl, for helping me design my first diagnostic and being a wizard with electronics. Saving the best for last, I'd like to thank my incredibly patient and wonderful office administrator, Meg Murphy, for somehow tolerating all of my antics and while still making sure I got paid enough money for rent each month. I will always treasure our conversations on the frustrations of the world and thank you for putting up with me during my tumultuous growth as a young adult.

I would not have survived my formative years of grad school if not for the camaraderie and companionship of my peers. First and foremost, I'd like to acknowledge Mike Meyers for being my brother in the trenches and always encouraging me to do a good job as we fought through lengthy problem sets. While I imagined that Mike would still be here today to celebrate the end of an era, he is forever in my heart and my hiking boots as a celebration of the life we lived together. For the nights I can't remember with friends I'll never forget, I would like to thank the Number One Boys: Nick Sudar (founder), Claudio Emma, David Bauer, and David Chester for our mutual love of Los Tacos sweaty burritos and being the best physics tutors I could ever ask for. For teaching me how to calculate β and actually taking the time to read my papers, I am especially grateful to Jeffrey Robertson (sorry about the nose job).

To the people who have only ever had my best interests at heart, I'd like to show gratitude for my family in being incredibly patient and supportive throughout my years at UCLA. While we may have been a thousand miles apart, I am ever grateful to my five wonderful sisters, Alessandra, Vittoria, Francesca, Maria, and Isabella for always making me feel like the golden child with their letters and messages of encouragement. For their countless sacrifices and teaching me the value of perseverance which has led me to where I am today, I am forever thankful for my parents, John and Marienza.

I have been blessed to share this journey with so many amazing people, but none have been more crucial towards ensuring its final success than my partner, Rachel Moss. Thank you for being so incredibly supportive and therapeutic towards me during my final years of spiritual soul searching. I love you and I appreciate you.

Finally I would like to thank the US DOE for their support of this work through awards DE-FC02-07ER54918:0023 and DE-SC0014113:0003 as well as the NSF with award PHY-1561912:004.

CURRICULUM VITAE

2008 – 2012	B.S. Physics, University of Texas at Austin
2012 – 2014	M.S Physics, University of California, Los Angeles

PUBLICATIONS

Schaffner, D. A., Carter, T. A., **Rossi, G. D.**, Guice, D. S., Maggs, J. E., Vincena, S., & Friedman, B. (2012). Modification of turbulent transport with continuous variation of flow shear in the large plasma device. *Physical Review Letters, 109*(13), 135002.

Schaffner, D. A., Carter, T. A., **Rossi, G. D.**, Guice, D. S., Maggs, J. E., Vincena, S., & Friedman, B. (2013). Turbulence and transport suppression scaling with flow shear on the Large Plasma Device. *Physics of Plasmas, 20*(5), 055907.

Fisher, D. M., Rogers, B. N., **Rossi, G. D.**, Guice, D. S., & Carter, T. A. (2015). Three-dimensional two-fluid Braginskii simulations of the large plasma device. *Physics of Plasmas, 22*(9), 092121.

Pueschel, M. J., **Rossi, G.**, Told, D., Terry, P. W., Jenko, F., & Carter, T. A. (2017). A basic plasma test for gyrokinetics: GDC turbulence in LAPD. *Plasma Physics and Controlled Fusion, 59*(2), 024006.

Rossi, G.D, Carter, T.A., Seo, B., Roberston, J., Pueschel, M.J., & Terry, P.W. (2021). Electromagnetic turbulence in increased-β plasmas in the Large Plasma Device. *Journal of Plasma Physics*. (Submitted)

CHAPTER 1

Introduction

1.1 Motivation

Described by Richard Feynman as “the most important unsolved problem of classical physics”, turbulence is a fascinating phenomenon that has been the subject countless scientific investigations for more than a century. Specifically, the physics of the interaction between plasmas and turbulence is critical to understanding many areas of space and plasma physics. In the case of astrophysical phenomena, turbulence plays an important role with phenomena such as Keplerian flow driving magnetorotational instabilities in acretion disks[1] and K-H instabilities driving transport between the earth’s magnetosphere and the solar wind[44]. In the development of plasma physics, understanding turbulence is vital to the development of fusion as a viable alternative energy source. While on paper fusion energy is a relatively simple reaction that has the potential to be the sole source of our long-term energy needs, these reactions require extreme temperatures and pressures such that confinement of these high-energy fuels has been the primary struggle over the last seventy years. A variety of confinement approaches have been proposed to mitigate particle and energy loss due to cross-magnetic-field transport, but almost all break down or become energetically inefficient as the cross-magnetic-field pressure gradients that are created subsequently drive turbulence and instabilities that increase plasma transport loss[52]. Thus, further investigation on the mechanisms that drive turbulence brings the potential to improve confinement in fusion plasma devices.

For commercial fusion reactors to be economical and viable, the production and stability of plasmas with a high ratio of thermal energy density to magnetic energy density, referred to as $\beta = P/(B^2/2\mu_0)$, is highly desirable. Plasma β can be thought of as an efficiency rating for a reactor, as the thermal energy output that enables ignition is compared to the magnetic energy input required to confine the plasma as it burns. Multiple scaling studies[11, 30, 19] have shown that the cost for the large magnets required for plasma confinement scale as $\beta^{1/2}$ and that in order for a fusion reactor to be compact and economically attractive, a minimum β in the range of 5 to 10% is required[51]. In addition, in order for fusion plasmas to operate continuously with adequate confinement, the ratio of self-generated current to total current in the core of a plasma, known as the bootstrap fraction, must be large[26] and can only occur when plasma β is finite[55, 7].

Achieving this minimum β requirement, however, can be difficult as β is self-limiting. As β increases in a plasma, the role of magnetic fluctuations become significant in driving and changing the character of instabilities such as the kinetic ballooning mode (KBM), ion temperature gradient (ITG), and trapped electron mode (TEM)[45, 3, 57]. Additionally, finite magnetic shear and/or strong magnetic hill configurations can destabilize the interchange mode[47] and lead to the stochastization of the magnetic field structure at the periphery, which reduces the available region for plasma confinement[53]. All together, these MHD instabilities degrade plasma confinement by driving anomalous transport and thus lead to a significant reduction in β.

In the past two decades major advances have been seen in reactor design such that the maximum β, commonly referred to as the Troyon beta limit, has been increased by a factor of 10[18]. However, the understanding of the mechanisms behind electromagnetic turbulence that lead to modified linear/nonlinear stability, changes in turbulent flow generation, and novel electromagnetic transport effects at higher β are still not fully understood[27, 50]. So far, laboratory investigations of pressure-gradient-driven turbulence have almost exclusively focused on plasmas with a low β where most of the instabilities, such as drift waves, involved with driving turbulence are largely electrostatic[28, 4, 9, 20].

With finite β ($> 1\%$), turbulence is expected to be electromagnetic and there are important quantitative and qualitative changes to the underlying instabilities. First, unstable drift waves couple to Alfvén waves, which can substantially modify linear mode properties and the nature of the resulting turbulence[25]. Second, the nonlinear saturation mechanisms are changed, modifying the turbulence amplitudes and wavenumber spectra[38, 37, 58]. Third, inherently electromagnetic structures of the turbulence like zonal fields or magnetic streamers can develop at a wide range of β

values[49]. Fourth, the relative importance of electromagnetic transport processes with respect to electrostatic ones increase with β as the electron heat flux along fluctuating magnetic field lines can carry a substantial part of the overall cross-field heat fluxes at high β [45, 3, 57, 39]. Fifth, new instabilities can develop as electromagnetic terms that were previously ignored become significant; for example, in tokamaks a transition from electrostatic instabilities such as the ion temperature gradient (ITG) to electromagnetic instabilities like the kinetic ballooning mode (KBM) as β is increased.

In addition to fusion, laboratory plasma experiments at finite β are also crucial to understanding problems in space physics. With the Sun, β has been observed to approach unity around the mid-corona region and thus placed new constraints on the modeling of its respective magnetic field and interpretations of the associated solar dynamics[13]. In the heliosphere, interactions between the Earth's magnetic field and the solar wind occur at finite β and exhibit unique effects such as energetic particle transport[59] and enhanced magnetic reconnection in the presence of pressure gradients[41].

1.2 Drift Waves at Low β

Occurring almost universally in magnetized plasmas, drift waves have been shown to be the dominant mechanism for the transport of particles, energy, and momentum across magnetic field lines[21]. Unlike the MHD flute instability or resistive tearing instability, drift waves easily become unstable and the growth of the instability requires neither a curved magnetic field nor a magnetic configuration for which lower magnetic-energy states exist. Simply a plasma with a non-uniform density profile and a strong background magnetic field is enough to trigger the drift-wave instability as the waves tap into the thermal energy of a plasma when expanding across magnetic field lines. Since by definition almost all plasma confinement strategies involve a non-uniform density profile, the study of drift waves and their low-frequency fluctuations that control transport is paramount to improving plasma confinement.

The drift-wave instability at its heart is similar to that of a simple Rayleigh–Taylor instability in which the magnetic field acts as a light fluid supporting a heavy fluid (the plasma). In the case of curved magnetic fields, the centrifugal force from particle motion within the plasma acts as an equivalent ”gravitational” force on the system. For a toroidal geometry, this radial force drives the MHD flute instability by which flute-like density structures grow at the boundary of the plasma and propagate in a wave-like behavior in the θ direction.

The drift-wave instability differs from that of the MHD flute instability in that the wavenumber $k_{\|}$ parallel to the background magnetic field B_0 is nonzero. As seen in Figure 1.1, this can be visualized as the same flute instability but with a modest helical twist in the parallel direction[5].

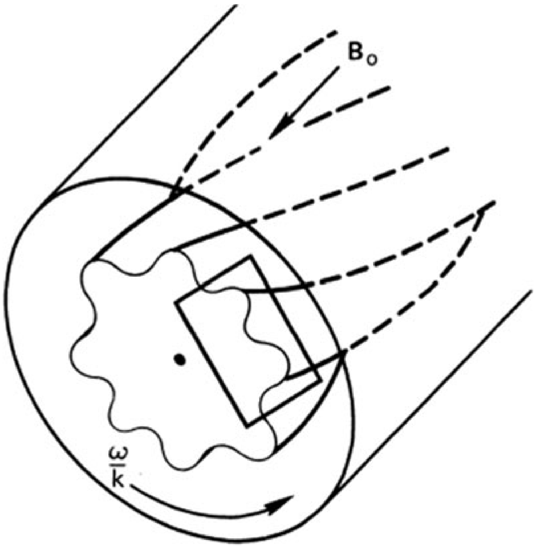

Figure 1.1: From Chen[5]. Visualization of the drift-wave instability in cylindrical geometry. Similar to a flute instability but with a slight helical twist in the parallel direction.

Focusing on the area outlined by the rectangle in Figure 1.1 and extending to slab Cartesian geometry we can briefly detail the mechanisms responsible for drift wave production. As seen in Figure 1.2, it begins with a zeroth order density gradient ∇n_0 pointing in the $-\hat{x}$ direction. Now one can imagine that there is a density perturbation such that the the line of constant density moves further outward in the $\hat{x}$ direction in some areas and further inward for others. With $k_{\|}$ being finite, this means that ions and electrons are allowed to travel freely across the background magnetic field

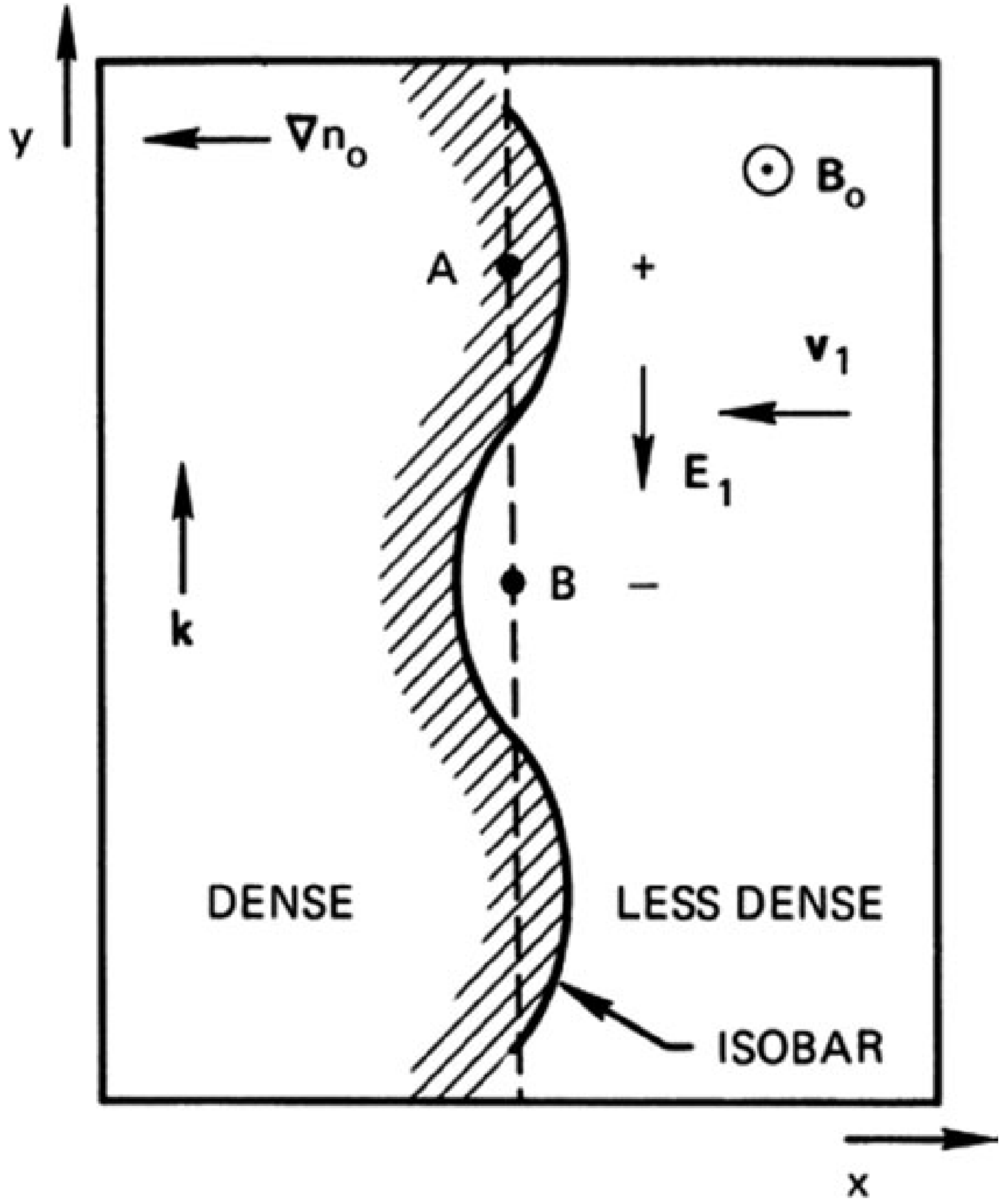

Figure 1.2: From Chen[5]. Visualization of the mechanisms behind drift wave production in Cartesian geometry extended from the rectangular area in Figure 1.1

lines in order re-establish thermal equilibrium. Since the electrons are much lighter than the ions, this means that electrons will be able to move faster down the field lines. This movement happens until parallel electron pressure balance is satisfied from the Boltzmann relation:

$$\frac{\partial p_e}{\partial t} = enE_{\parallel} \tag{1.1}$$

$$\frac{\delta n_e}{n_e} = \frac{e\delta\phi}{T_e} \tag{1.2}$$

where the electron pressure is defined $p_e = n_e T_e$ and first order fluctuations in temperature $\delta T_e \sim 0$. Because of this relationship, areas where the density has increased from equilibrium ($\delta n_e > 0$) such as point A in Figure 1.2 will see a higher electric potential than those areas where density has decreased from equilibrium ($\delta n_e < 0$), such as point B. This in turn creates an electric field in the $-\hat{y}$ direction between point A and B which then leads to a first order drift $\delta \mathbf{v} = (\delta \mathbf{E} \times \mathbf{B})/\mathrm{B}^2$ in the $\hat{x}$ direction. From Faraday's ($\mathbf{E} = -\nabla\phi$) and assuming all any perturbation quantity δN can be written as $\approx \delta N e^{(i\mathbf{k}-i\omega t)}$ one can write the magnitude of this first order drift velocity:

$$\delta v_x = -ik_y \delta\phi / B \tag{1.3}$$

and so while δn_e is in phase with $\delta\phi$, they are both $\frac{\pi}{2}$ out of phase with δv_x. This means that while the plasma fluid oscillates in the $\hat{x}$ direction, there is no net transport of plasma in the $\hat{x}$ direction although from the finite k_y it is known that the wave travels in the $\hat{y}$ direction. Now looking to the density fluctuations, one can invoke the plasma continuity equation ($\frac{\partial n}{\partial t} + \nabla \cdot n\mathbf{v} = 0$) and assuming an incompressible fluid arrive to first order at

$$-i\omega\delta n_e = -\delta v_x \frac{\partial n}{\partial x} \tag{1.4}$$

which now combining Equation 1.3 and Equation 1.4 can be rearranged to solve for the phase velocity of the drift wave $v = \omega/k_y$:

$$\frac{\omega}{k_y} = -\frac{T_e}{eB}\frac{\frac{\partial n_e}{\partial x}}{n_e} = v_{De} \tag{1.5}$$

Thus these drift waves travel at the electron diamagnetic drift velocity and are considered stable as the amplitude of the perturbation remains constant such that there is no growth. However, this stability is easily broken as corrections to δv_x for the ions cause the response in the potential profile $\delta\phi$ to be delayed relative to the density profile δn_e. The first correction, as seen in Equation 1.6, is due to finite-Larmor-radius (FLR) effects where r_L is much bigger for ions than the electrons and $\mathbf{E}\times\mathbf{B}$ flow is no longer independent of species.

$$\mathbf{v}_{\mathbf{E}\times\mathbf{B}} = (1 + \frac{1}{4}r_L^2\nabla^2)\frac{\mathbf{E}\times\mathbf{B}}{B^2} \tag{1.6}$$

Additionally, as seen in Equation 1.7, polarization drift due to the time varying **E** fields as the wave travels in the $\hat{y}$ direction will disproportionately affect the ions more than the electrons, further delaying the potential profile response.

$$\mathbf{v_p} = \pm\frac{1}{\omega_c B}\frac{d\mathbf{E}}{dt} \tag{1.7}$$

Resistivity due to electron-ion collisions ν_{ei} can also cause electron response to be delayed as it modifies the parallel electron pressure balance from Equation 1.1 to now be

$$\frac{\partial p_e}{\partial t} = enE_{\parallel} - nm\nu_{ei}v_{\parallel} \tag{1.8}$$

In total, these corrections cause the potential profile to shift out of phase with density such that the δv_x becomes in phase with the density perturbations. When this occurs, areas of outwardly perturbed density are carried out even further from outward pointing δv_x and the perturbation grows indefinitely. The resulting dispersion relation can thus be written as:

$$\omega \approx \omega_* + i\nu_{ei}\left(\frac{k_y}{k_{\parallel}}\right)^2\left(\frac{{\omega_*}^2}{\omega_{ce}\Omega_{ci}}\right) \tag{1.9}$$

where $\omega_* = k_y v_{de}$.

1.3 Drift-Alfvén Waves at Increased β

Another fundamental wave for magnetized plasmas is the shear Alfvén wave. First proposed by Hannes Alfvén in 1945, shear Alfvén waves have been discovered in many many astrophysical, heliospheric, and magnetic fusion phenomena. These hydrodynamic waves exist only at relatively low frequencies $\omega < \omega_{ci}$ and propagate along magnetic field lines at the the Alvén speed, V_A whereby:

$$V_A = \frac{\omega}{k_\parallel} = \frac{B}{\sqrt{4\pi n M}} \tag{1.10}$$

with M being the mass of the ions, n being the plasma density, and B being the magnetic field.

Under the assumption of $\beta << 1$, shear Alfvén waves ($\omega_A \sim k_z, v_A$) are very distinct from lower frequency drift waves ($\omega_{\text{drift}} \sim k_y v_{de}, k_z C_S$)[17]. However, in large magnetized plasmas where β greater than the mass ratio (m/M)[31] or where significant pressure gradients are present[2], the diamagnetic drift can cause shear Alfvén waves to couple to electrostatic drift waves and form electromagnetic drift-Alfvén waves. These drift-Alfvén waves are characterized by both density and perpendicular magnetic field fluctuations and that grow unstable via electron Landau damping and/or collisions[16]. Regarding the 2D structure of these waves, as shown in Figure 1.3, previous experiments have shown that drift-Alfvén waves driven by pressure gradients to have a low-m ($m < 6$) eigenmode structure for density and $B_\perp$ fluctuations.

While there have been many experiments on the excitation of drift-Alfvén waves and associated turbulence driven by pressure-gradients[31, 34, 2, 33], these have been done on predominantly lower-β plasmas. With the modifications at higher-β still relatively unknown, this dissertation seeks to explore the novel effects of β up to $\sim 10\%$ and is detailed in the following section.

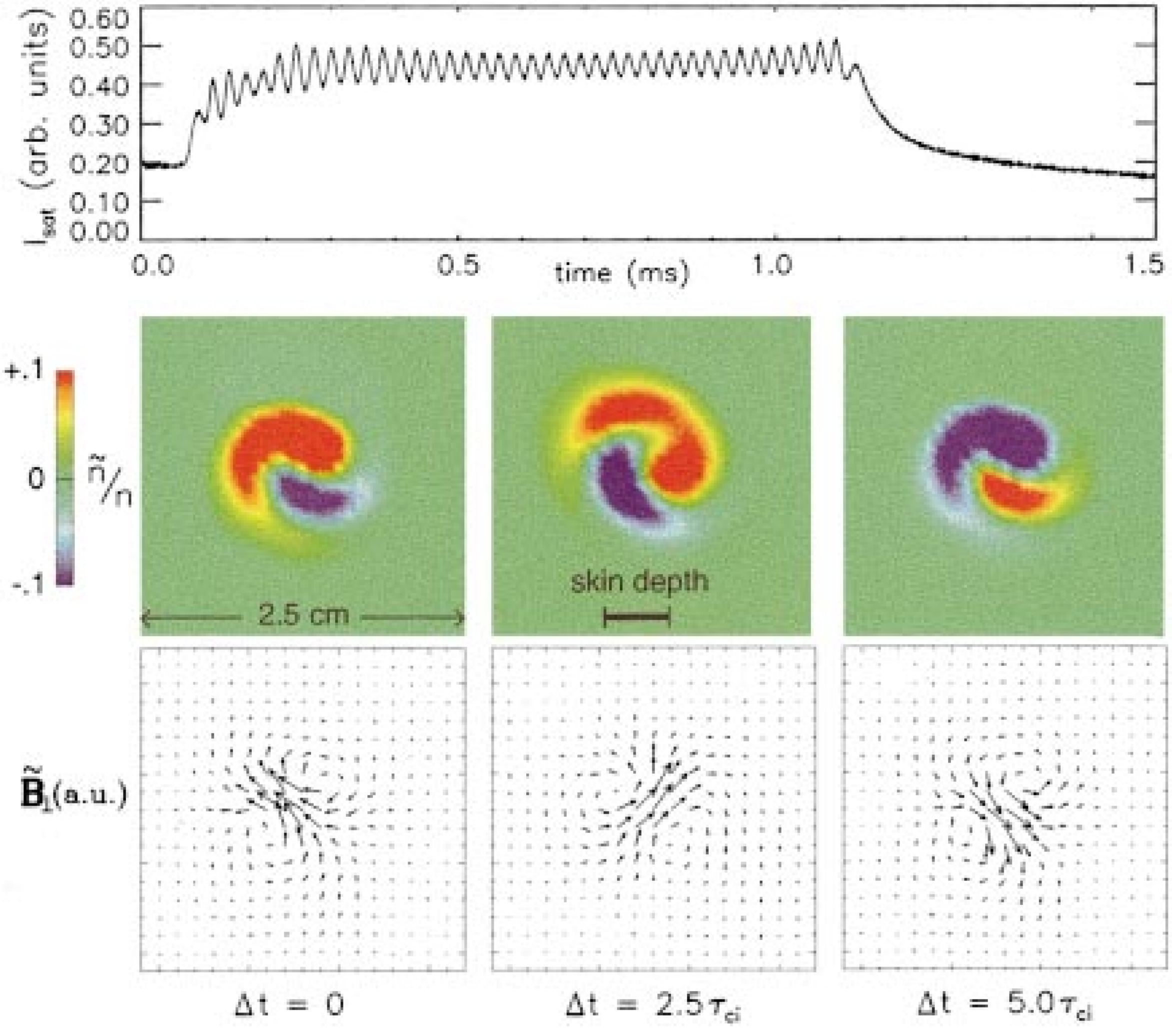

Figure 1.3: Figure taken from Morales and Maggs[2], (Color) Middle: Time evolution of structure across the confining magnetic field of high-frequency density fluctuations. Red color denotes a density increase, and blue a decrease, relative to the average value. Bottom: Self-consistent magnetic fluctuations having shear-mode polarization. Rotation is in the direction of the electron diamagnetic drift. Top: Temporal variation of the ion saturation current at a radial location near the steepest gradient in the temperature profile. The ion cyclotron period is τ_{ci}.

1.4 Dissertation Objective and Outline

The objective of this dissertation is to investigate the electromagnetic modifications to turbulence and transport that occur as β increases. In order to transition mostly electrostatic plasma turbulence into partially electromagnetic, β is increased by lowering the background magnetic field and holding other parameters such as density and temperature fairly constant. This increase in β causes fundamental changes to the turbulence mechanisms and introduces the possibility for new instabilities to grow. To better understand and classify these instabilities, volumetric measurements of mean plasma profiles and fluctuations for temperature, density, and magnetic field, are made at different β conditions.

A review of the motivation and derivation of drift waves in increased β plasmas has been covered in this chapter. Chapter 2 contains information on the experimental setup, diagnostics, and methodology for increasing β. Chapter 3 documents the modifications to various plasma properties as β varies with the surprising observation of increasing parallel magnetic fluctuations. Chapter 4 then explores the possibility that these modifications are the result of an electromagnetic drift-Alfvén wave by making comparisons between computational results from a developed simple-slab model theory and experimental observations.

CHAPTER 2

Experimental Setup

2.1 The Large Plasma Device

The experimental data for this thesis was collected in the LArge Plasma Device (LAPD) at UCLA. Originally constructed in 1991[14] with numerous upgrades in the last two decades to plasma sources and diagnostics[15], LAPD is an excellent general-purpose research device for conducting laboratory physics. The range of plasma parameters have been carefully selected in order to facilitate ease of use with simple diagnostics that allow for direct measurements of plasma properties. These parameters are advantageous compared to those of most fusion-level devices where extreme plasma temperatures destroy most direct measurement diagnostics and thus only spectroscopic[29] or fast reciprocating probe[35] techniques are available for data collection.

Pictured in Figure 2.1, LAPD is an 24m long, 1m diameter cylindrical vacuum chamber which utilizes two turbomolecular pumps on either side to achieve a base pressure of 5×10^{-7} Torr. Mass flow controllers then regulate filling the device with a variety of working gas options (H_2, He, Ne, or Ar). The rate of gas released reaches an equilibrium with the rate of gas removed from the turbomolecular pumps such that the overall fill pressure within the devices is approximately 3×10^{-5} Torr. The working gas is then ionized and turned into plasma using two cathode sources located at opposite ends of the chamber 17m apart. The first source, a large barium oxide cathode (BaO), has an input power source of ≈ 0.5 MW that produces a .60m diameter plasma column with a discharge duration of ≈ 10ms and a duty cycle of 1 Hz[36]. The second, a smaller lanthanum hexaboride cathode (LaB_6), has an input power source of ≈ 0.1 MW that produces a 0.2m diameter plasma column with a similar discharge duration of ≈ 10ms[8]. The LaB_6 is mounted on a screw drive system such that it can be removed from the machine when not in use or when aligning probes.

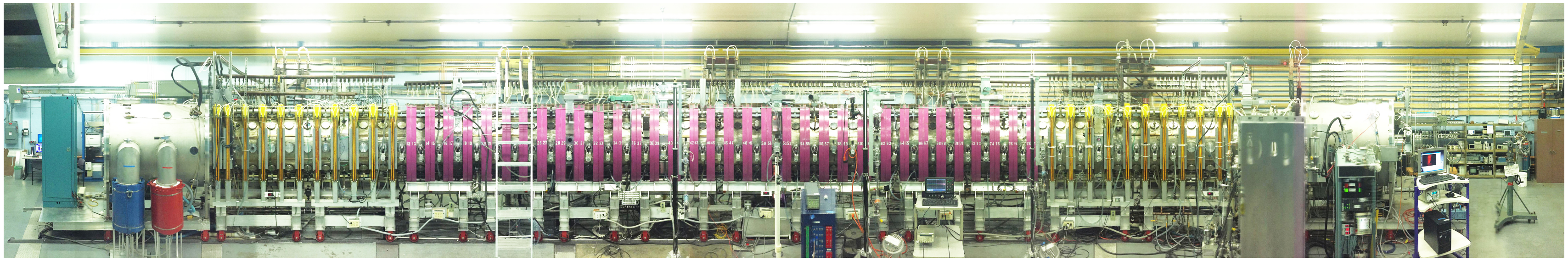

Figure 2.1: Panoramic photography of the Large Plasma Device (LAPD) at UCLA. Plasma sources are located on opposite ends of the chamber directly adjacent to the yellow colored electromagnets. Two of the four turbomolecular pumps can be seen on the left side of the device (by the BaO source) as red and blue cylinders. Plasma measurements are taken primarily in the middle of the device where the purple colored electromagnets control the axial background magnetic field.

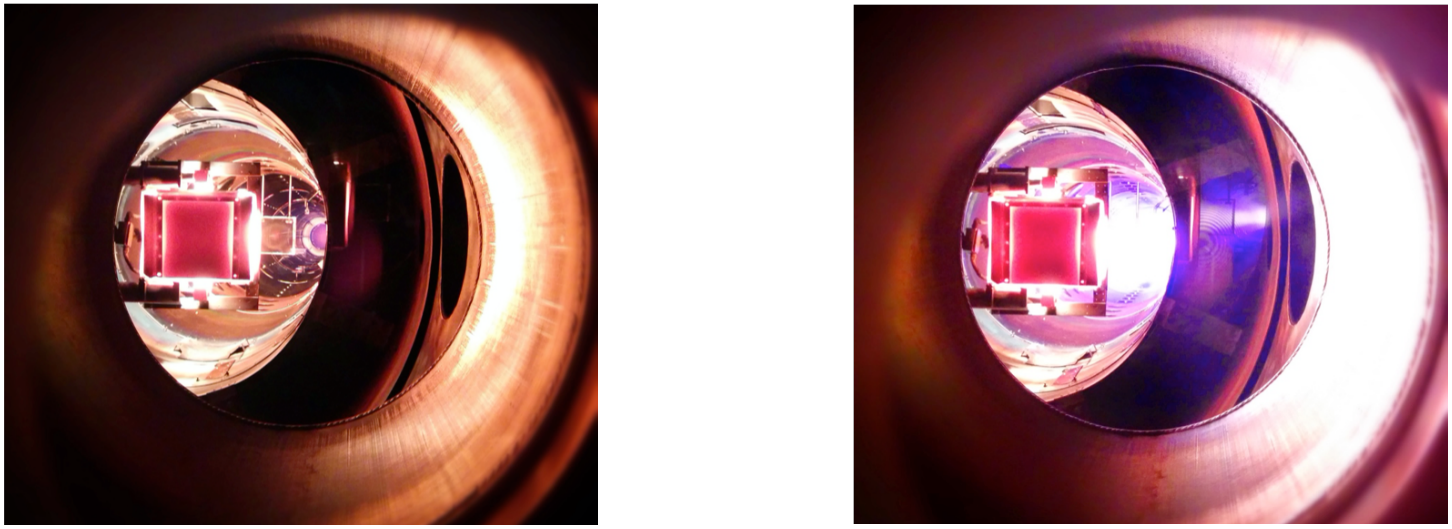

(a) BaO source discharge

(b) LaB_6 source discharge

Figure 2.2: Photographs of the different cathode sources during their respective discharges in a Helium plasma. Photograph is taken from a view port close to the LaB_6 source with the BaO source visible in the background.

The access to two different plasma discharge sources allows for unique configurations to be used in different experimental setups. The BaO source, as seen in Figure 2.2a, produces a larger diameter plasma column while the LaB_6 source, as seen in Figure 2.2b produces a smaller but much hotter and denser plasma column. In order to reach the finite values of $\beta = P_{plasma}/P_{magnetic}$ for this experiment, both sources were utilized. Doing so has been shown to enable up to a 100x increase in plasma pressure than what would be possible with only the BaO cathode while also providing a more reliable and reproducible plasma discharge than would be possible with only the LaB_6 cathode. In addition, as seen in Figure 2.3, the discharges were staggered to provide an isolated steady state region where it was possible to study instabilities of interest without having to filter out circuit effects of two competing plasma sources running simultaneously. For the purposes of this experiment, the majority of data analysis is performed on the flat-top region of the LaB_6 discharge, from t = 43ms to t = 50 ms in Figure 2.3, where the plasma is determined to be the most steady-state. The plasma discharges are reproducible with minimal variation between shots such that data can be analyzed by taking the average of many shots at a single position. This helps to eliminate signal noise and distinguish persisting features in the plasma.

90 electromagnets surround the machine and allow for variable axial background magnetic field profiles, B_0, with field strengths between 175 and 3000 Gauss. This background field guides nearly fully ionized helium plasma with core electron temperatures from 1 to 15 eV and densities $\approx 10^{13}$ cm^{-3}. Typical plasma parameters for helium discharges at 1kG, the main gas and a starting field used for this experiment, are shown in Table 2.1. A key characteristic, LAPD has an extensive set of diagnostic ports, 450 in total, with 60 of these ports being ball-valve vacuum feedthroughs that allow three dimensional placement of probes inside the plasma. Probes are positioned using a series of stepper motors which offers simultaneous movement in two dimensions. Figure 2.4 details the geometry for probe placement and data collection. A large portion of the data analysis consists of “radial lines” by which the probes are fixed to y = 0 and z = 0 but traverse the $\hat{x}$ direction which will be referred to as the radial position $r = x$. An advanced computer controlled data acquisition and motion system allows for autonomous control of probes, antennas, and even additional plasma sources. Thus, under 24 hour, 1 Hz operation of the device, an enormous amount of data (86,400

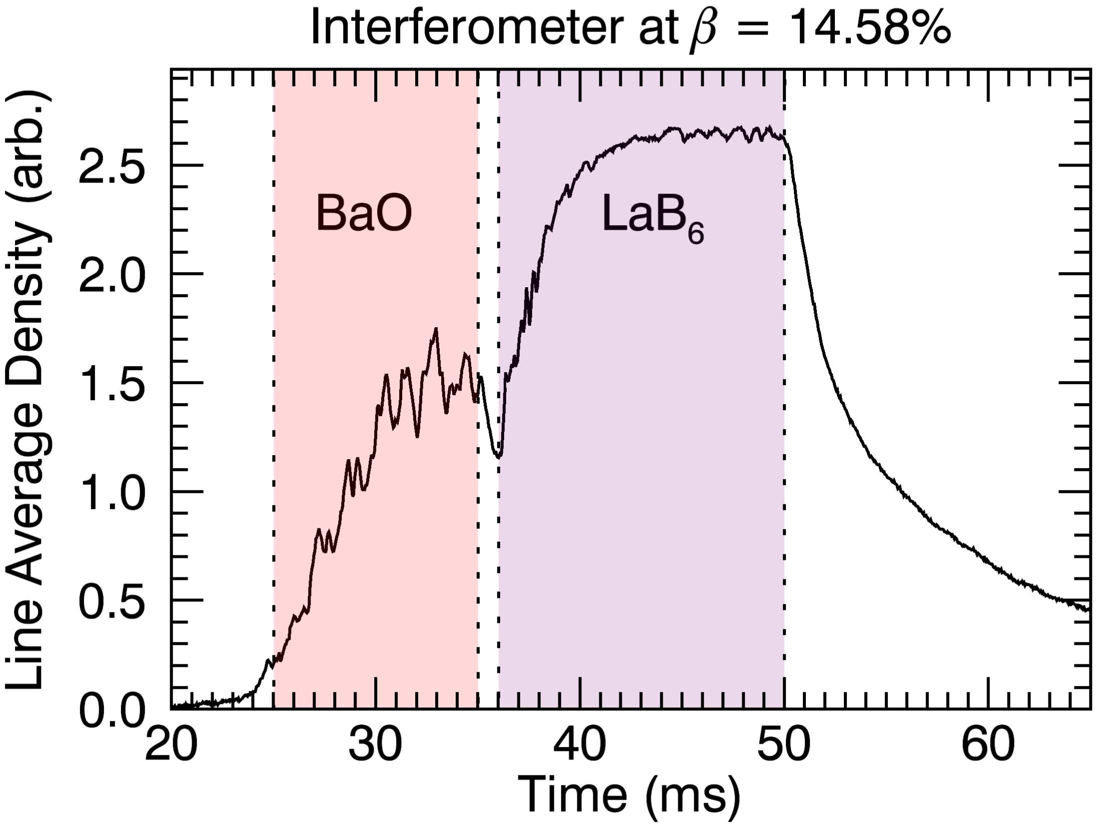

Figure 2.3: Line averaged density from interferometer showing the temporal placement of BaO and LaB_6 plasma source discharges at increased β. Shaded region represents the discharge time window for each source.

shots or 432 seconds of steady state plasma per day) can be collected on much shorter time frames than conventional human operated experiments.

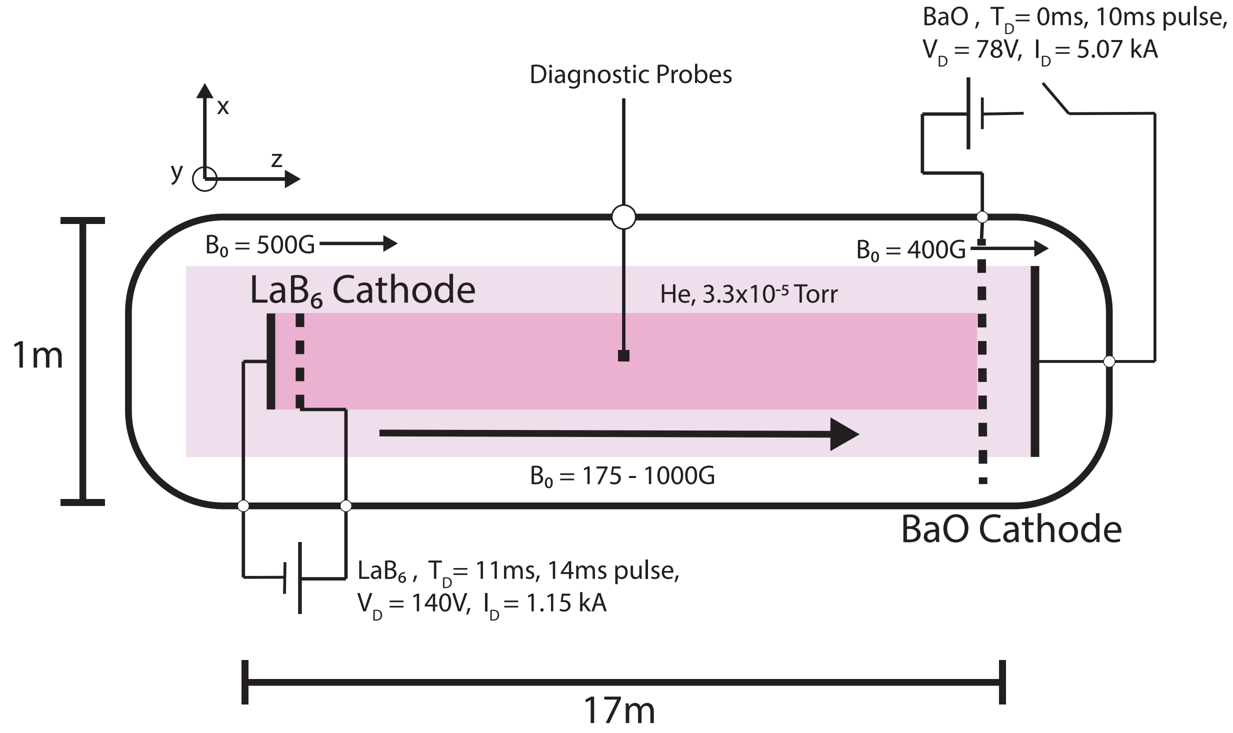

Figure 2.4: Experimental setup with magnetic field profiles. Data for this experiment was measured in the center of the machine where the background magnetic field profile is uniform.

2.2 Diagnostics

An extensive set of diagnostics were used in order to characterize the turbulence and transport of the plasma in this experiment. Measurements of electron density n_e, electron temperature T_e, floating potential V_f and their corresponding fluctuations ($\delta n_e, \delta T_e, \delta V_f$) were made using triple Langmuir probes. The first probe, referred to as the Rossi-6 probe (Figure 2.5), is a double sided probe consisting of 3, 0.76 mm diameter, tantalum tips each side that are arranged in a triangle pattern. Tips 1 and 2 are separated 3 mm along the magnetic field lines and used as a double probe to measure ion saturation current by applying a bias of 70v, needed to reject primary electrons,

Parameter	**Discharge Value**
Discharge time	$\approx 10ms$
Axial plasma length	17 m
Azimuthal plasma diameter	$\leq .6m$
Plasma density	1×10^{13}
Electron temperature	5-15 eV
Ion temperature	≤ 1 eV
Magnetic field	.2-3 kG
Electron gyroradius at 1 kG	0.08 mm
Ion gyroradius at 1 kG	2mm
Ion sound speed	$\approx 10^4$m/s
Ion sound gyroradius at 1 kG	.5 cm
Collisionless skin depth	4 mm
Ion cyclotron frequency at 1kG for He	380 kHz
Electron collision time	$.5\mu s$
Electron mean free path	.5 m
Parallel loss time	≈ 1 ms
Ionization fraction	$\gtrapprox 50\%$
Ion-neutral collision frequency	≈ 5 kHz
Typical frequency in drift-wave spectrum	$\lessapprox 50$ kHz

Table 2.1: Typical parameters for helium discharges in LAPD

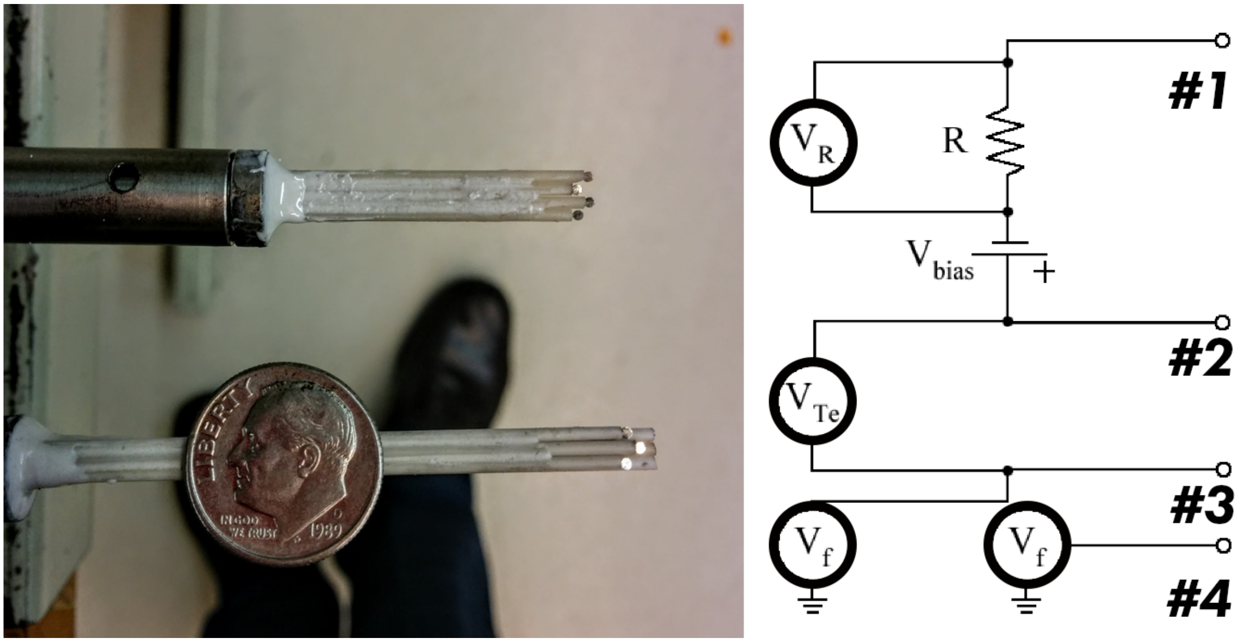

Figure 2.5: Rossi-4 (Top left) and Rossi-6 (Bottom left) Langmuir probes with a dime for size reference. (Right) a circuit diagram of how tips were used to make measurements of I_{sat}, V_f, and T_e.

and measuring the voltage across the resistor. This ion saturation current is used as a for a proxy for plasma density, $I_{sat} \propto n_e\sqrt{T_e}$ as one can assume a Maxwellian plasma. The mean profiles were determined by normalizing averaged I_{sat} profiles to multiple line-averaged interferometer measurements of the plasma column located axially along the device. Tips 3 and 4 are separated 3mm perpendicular to the magnetic field lines and used to measure floating potentials such to derive azimuthal electric field fluctuations δE_θ and temperature δT_e using the triple Langmuir probe method[6] (potential difference between the electron collecting tip 2 and tip 3). This probe can also be rewired to a sweeper box that uses fast sweeps of potential and measured current to obtain an IV curve for deriving plasma potential and electron temperature at specific locations with less time resolution. Plasma density (n_e) and potential (ϕ_p) fluctuations are inferred from fluctuations in ion saturation current (I_{sat}) and in floating potential (v_f) from a Langmuir probe by the relationship

$$V_f = \phi_p - \frac{1}{2}T_e \ln\left(\frac{2M}{\pi m}\right) \tag{2.1}$$

such that under the assumption that temperature fluctuations are negligible one can infer characteristics of density and potential fluctuation from δI_{sat} and δv_f.

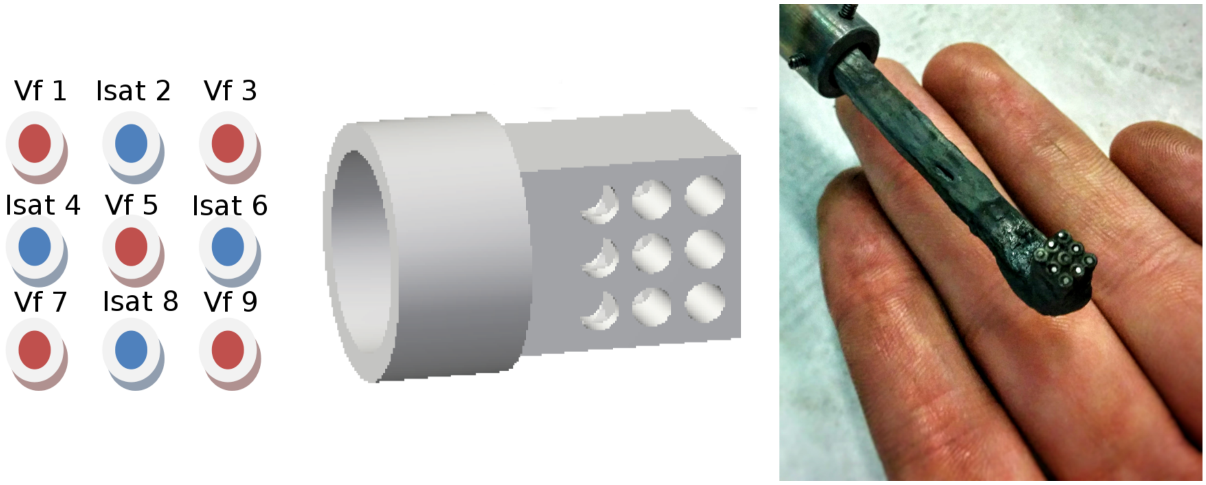

Figure 2.6: 9 Tip Reynolds probe in the alternating V_f and I_{sat} configuration for measuring 2D flux.

Pictured in Figure 2.6, another Langmuir diagnostic used in the experiment was a 3x3 array of 9 flush surface tantalum tips which is hereon referred to as the Reynolds probe. The tips are .508 mm in diameter, spaced .787 mm apart, and can be individually set to measure either floating potential (V_f) or ion saturation current (I_{sat}). A highly versatile probe, the Reynolds probe can be arranged such that all the tips record V_f and be used in pairs to calculate different electric fields (E_r, E_θ) and thus quantities such as Reynolds stress ($\langle \delta v_r \delta v_\theta \rangle$) and vorticity ($\nabla \times \mathbf{v}$)[22]. The tips can also be set alternating to measure both V_f and I_{sat} and thus calculate quantities such as radial particle flux ($\langle \delta n_e \delta v_r \rangle$)[48] and momentum flux ($\langle \delta n_e \delta v_r \delta v_\theta \rangle$)[32].

A key focus of this experiment, measurements of magnetic field fluctuations were made with three-axis magnetic induction (or B-dot) probes. As pictured in Figure 2.7, these small, high frequency probes consist of different pairs of magnetic pickup coils oriented in various axes such that one can integrate the signals from differential amplifiers and use Faraday's law ($\varepsilon = -\frac{d\Phi_B}{dt}$) to calculate magnetic field fluctuations $\delta B_\perp, \delta B_\parallel$[10].

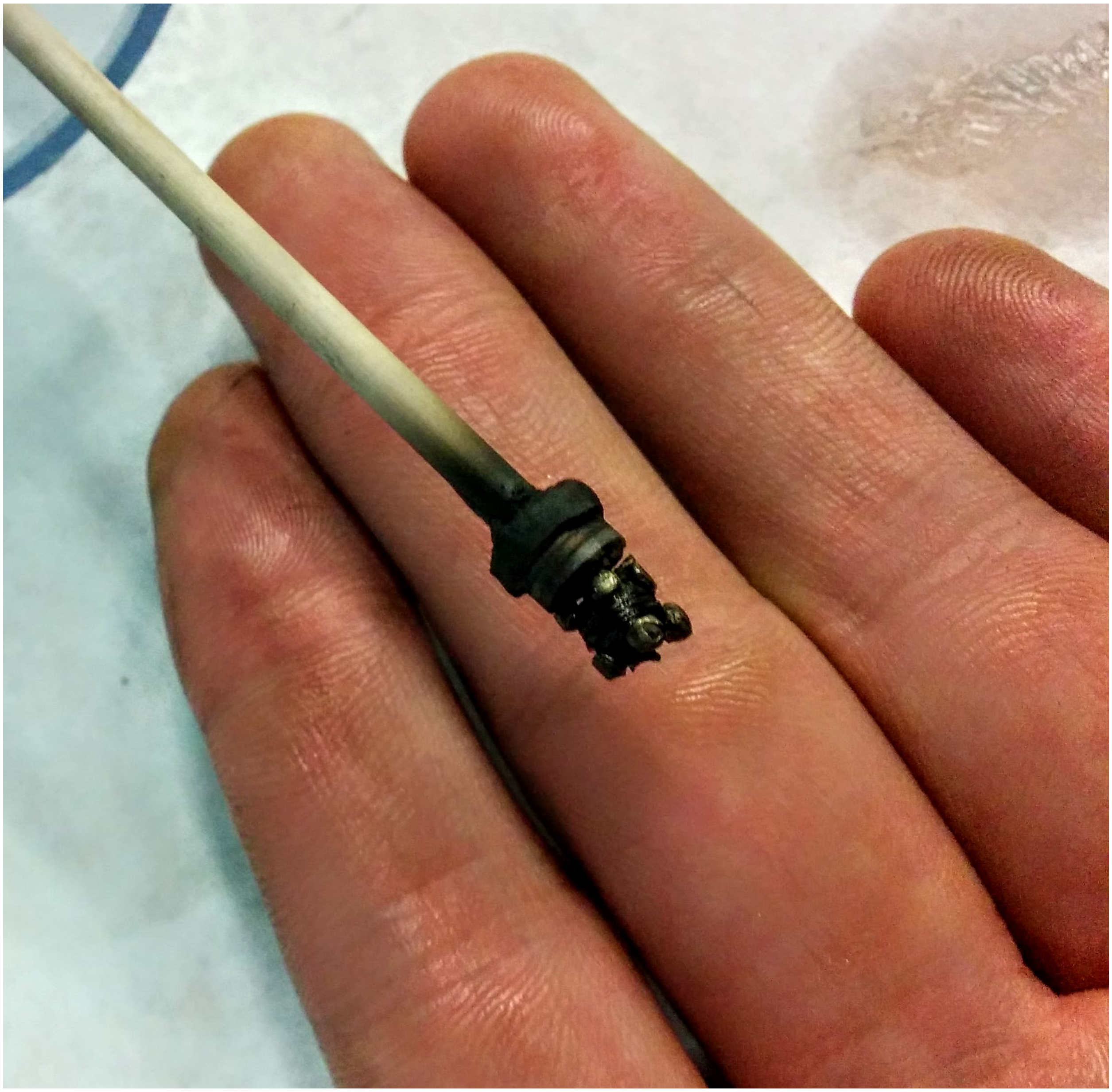

Figure 2.7: B-Dot probe after many hours in the machine. The protective cap has been removed, exposing the Vespel cube core and coil windings.

2.3 Continuous Control of β

The primary goal of this experiment was to document changes to turbulence and transport at various β regimes (purely electrostatic vs. partially electromagnetic). As previously discussed in Chapter 1, plasma β is defined as the ratio of the plasma pressure ($n_e K_B T_e$) to magnetic pressure ($\frac{{B_0}^2}{2\mu_0}$). From this expression, one can see that n_e, T_e, and B are possible parameters that can be varied in order to study different β conditions of a plasma. When considering the operational design of LAPD, one can immediately eliminate using n_e or T_e to vary β conditions. Firstly, there are no inputs to the experiment that allow for independent control of either n_e or T_e as they are closely connected to one another. Secondly, while inputs on the machine that control n_e and T_e together do exist, such as discharge current/voltage of sources and gas fill pressure, these inputs are considered too dangerous to be controlled by the data acquisition system. Thus, controlling these inputs manually would require an exorbitant amount of time to collect data on multiple β conditions compared to choosing an input that can be controlled by a computer. Thirdly, the precision on the manually controlled machine inputs for n_e and T_e is not as high as those controlled by a computer and thus it would be nearly impossible to return to the exact same β conditions between data runs. This leaves B_0, the background magnetic field in the plasma, which has many advantages for setting β in the experiment. Firstly, as will be detailed later, B_0 is relatively easily to control with high precision via the data acquisition system which allows for reproducible β conditions between experimental runs. Secondly, because $\beta \propto B_0^{-2}$, the inverse exponential relationship enables a much wider range of β conditions that can be accessed for relatively small changes in B_0 compared to the linear relationship of n_e and T_e.

In LAPD, B_0 is set by an array of 90 magnetic coils that produces a solenoidal background magnetic field 17.54m long down the center of the chamber. These coils are spaced at 32cm from center to center with a magnetic ripple error of $\approx 0.1\%$. The magnets are divided into four distinct groups. First, there are the yellow BaO magnets which control the field around the BaO cathode source at the south end of the machine. Moving further north, the purple magnets control the field in the center of the machine and is where the majority of data is recorded. Thirdly, there are the yellow LaB_6 magnets which control the field around the LaB_6 cathode source at the north end of the machine. Lastly, a set of black magnets are located behind the $\mathrm{LaB_6}$ cathode source and primarily used when auxiliary instruments such as ion beams are attached to the north end of the machine. Within each group, the magnets are controlled by separate power supplies which can be individually set to different currents to produce an unlimited variety of non-uniform magnetic field profiles.

The intellectual merit of this experiment was founded in the novel ability to study plasma at higher values of β than had been previously achieved in LAPD. Due to the inverse relationship between B_0 and β, reaching these unexplored β required lowering the background magnetic field significantly (<200G compared to the usual 1000G). While a uniform solenoidal field throughout LAPD was desired, operational limits prevented the BaO source from discharging reliably below $B_0 = 400$G at the axial location of the source. Through an extensive amount of trial and error, it was determined that the magnetic field at the sources (the yellow magnets) should be kept at 400G and 500G for the BaO and $\mathrm{LaB_6}$ source respectively. This ensured reliable and reproducible discharges while allowing the magnetic field in the center of the machine (purple magnets) to be varied from a range of 175-1000G with the least changes to the discharge current and voltages of the sources.

With a finite amount of time allocated on LAPD to collect data ($\approx$ 2 weeks) came the need to maximize the range and resolution of β conditions to measure. As detailed in Table 2.2, 10 background fields (B_0) were chosen for the primary campaign where probes traveled over a large radial section of the plasma (r = -20 to r = +35cm). A quicker secondary campaign scanned a smaller radial section of the plamsa (r = 0 to r = +20cm) and included 6 additional $B_{||}$ conditions (625, 225, 215, 205, 195, and 185G).

As B_0 is varied, measurements of density (n_e) and temperature (T_e) using swept Langmuir probe and line-averaged interferometer data confirmed that the mean pressure profile remained nearly constant for the different B_0 conditions. These measurements were then taken at the core of the plasma and used to calculate the value of β associated with each B_0 condition (see Table 2.2). Varying the field in the center of the machine from 175G to 1000G resulted in a β range of $\approx 15\%$ to 0.17% respectively with marginal magnetization at the highest β as ≈ 4 ion gyroradii were able to fit into the diameter of the $\mathrm{LaB_6}$ plasma column. Diamagnetic modifications of the mean field were measured (discussed later) and at the highest β represented less than 5% the background field.

Field (G)	Beta (%)
1000	0.17
750	0.39
500	0.88
450	1.1
400	1.5
350	1.9
300	3.1
250	5.1
200	8.4
175	15

Table 2.2: Primary background magnetic field settings and measured β conditions

Using the background field strength to vary plasma β however does have its drawbacks as other dimensionless parameters are not able to be held fixed in the scan. In particular, parameters such as $\rho^* = \rho_s/a$, where ρ_s is the ion sound gyroradius and a is scale length in the plasma, here taken to be the plasma diameter (20cm). This parameter was seen to vary from $\rho^* \sim 0.02$ to $\rho^* \sim 0.1$ over the range of magnetic field used in the experiment.

When plotting the relationship between B_0 and β in this experiment, as seen in Figure 2.8, a power-law fit can be applied to the data. This fit is close to the expected $\beta \propto 1/B_{\parallel}^2$ and also allows one to extrapolate that a $B_0 \approx 75$G would be required to achieve order unity for β.

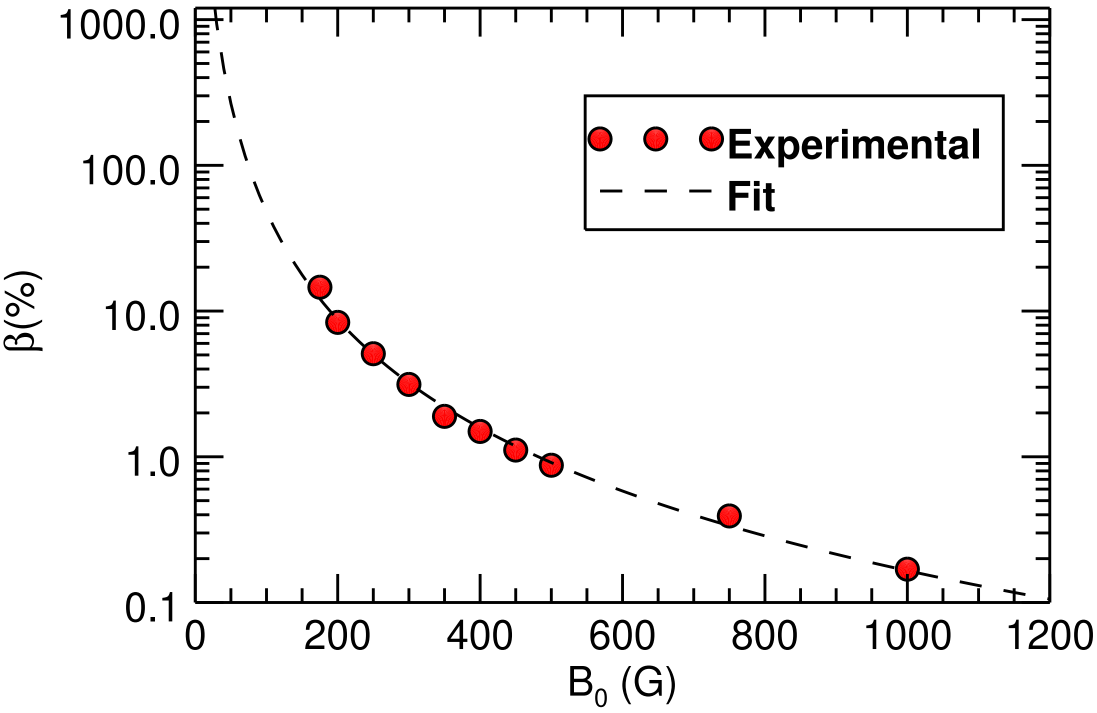

Figure 2.8: Measured plasma β for different background magnetic fields within the middle purple magnet section of the device. A power-law fit $\beta(\%) = (4\times10^6)(B_0)^{-2.46}$ to the data is also included.

CHAPTER 3

Modifications to Turbulence and Transport with β

The details of modifying the background magnetic field and its effect on plasma β are discussed in this chapter. With different β conditions come modifications to the mean and fluctuation profiles for various diagnostics. An analysis of these changes and their effect on turbulence and transport is examined.

3.1 Turbulence at Low β

For the following radial profiles in this experiment, Langmuir and magnetic diagnostic probes are used to measure the plasma at many different x for $y = 0$. These probes have a spatial resolution of 0.5 cm and measurements are averaged over 15 shots per position. Mean plasma potential and electron temperature profiles are determined from high spatial resolution (0.5cm) floating potential measurements and electron temperature by using the triple-probe technique described in Figure 2.5. These measurements are then calibrated to swept Langmuir probe measurements at specific radial locations with a lower spatial resolution.

As seen in Figure 3.1, strong pressure gradients along the radial direction are already present in LAPD even before increasing β. These naturally occurring pressure gradients can be also accompanied by $\mathbf{E} \times \mathbf{B}$ azimuthal flow which together provide free energy for the growth of instabilities[48]. In this experiment, initial evidence for the presence of gradient-driven instabilities is observed when looking at the density fluctuation profiles in Figure 3.2. A peak in fluctuation amplitude happens to be localized to the same radial region (r = 5cm) as the peak pressure gradient in Figure 3.1.

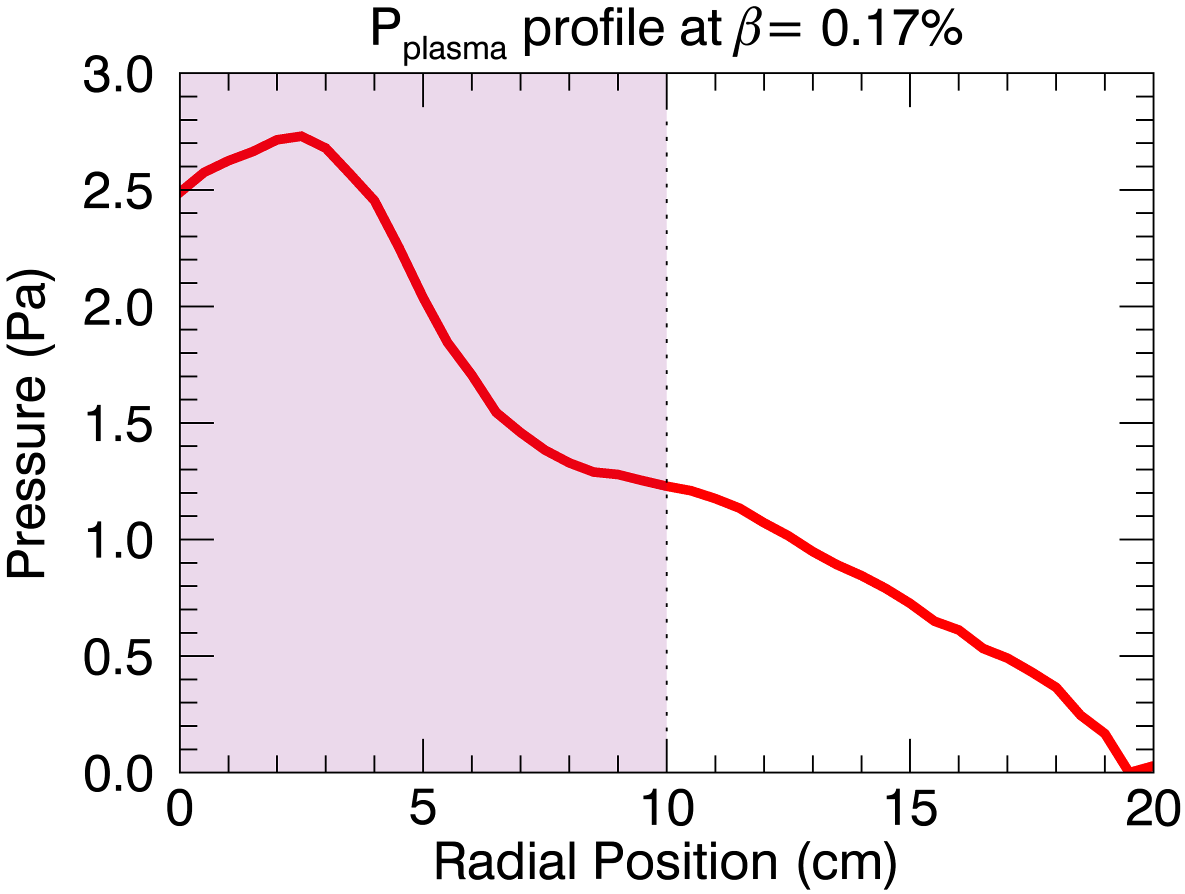

Figure 3.1: Plasma pressure ($n_e k_B T_e$) profile for the lowest β = 0.17% condition. Electron temperature is calculated from high spatial resolution triple probe analysis calibrated to swept Langmuir measurements at a few radial positions. Shaded area in purple represents the radial extent of the LaB$_6$ source.

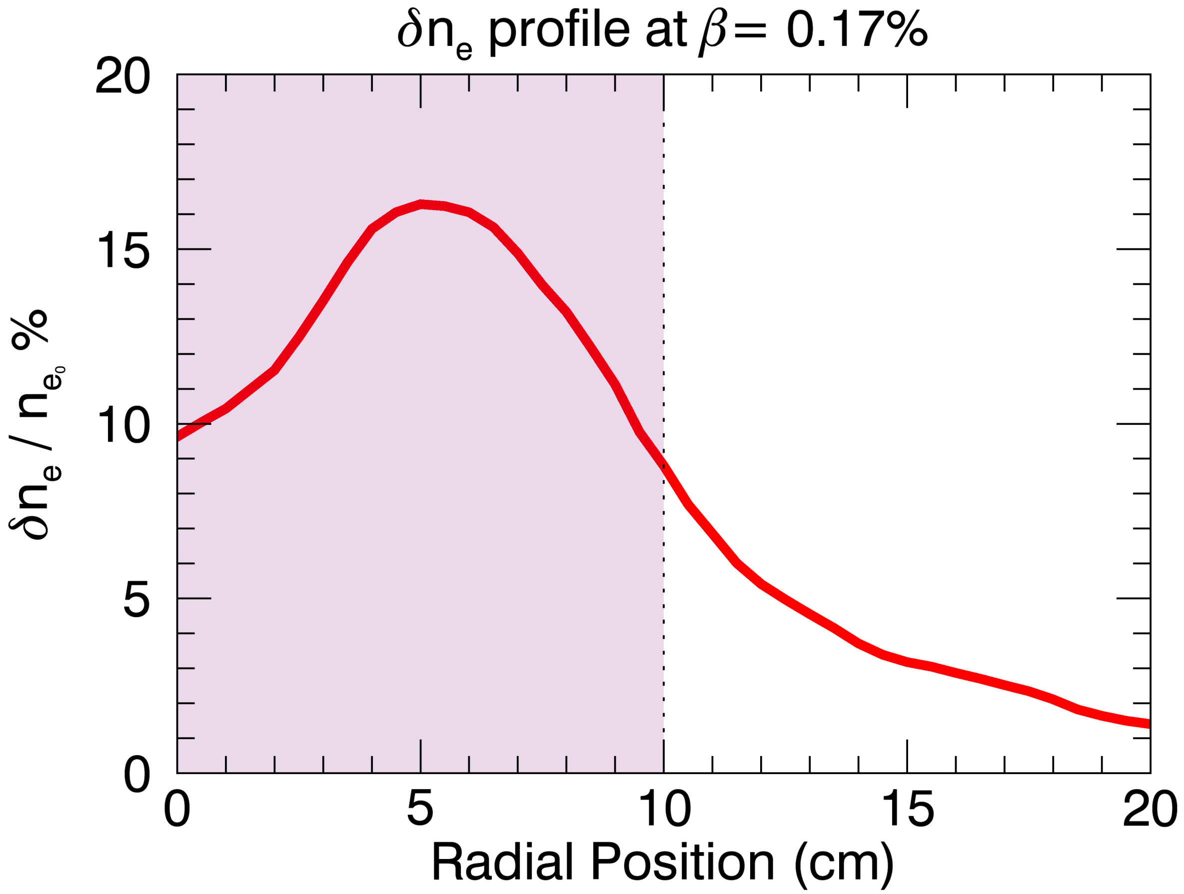

Figure 3.2: RMS density fluctuation profile for the lowest $\beta = 0.17\%$ condition. Shaded area in purple represents the radial extent of the LaB_6 source. Fluctuations peak around the same radial location of the peak pressure gradient seen in Figure 3.1

A wide variety of electrostatic instabilities such as Kelvin-Helmholtz or rotational interchange are prevalent in LAPD plasmas. While at higher β electromagnetic instabilities can exist[12], for low β the resistive drift-Alfvén wave generally has the fastest growth rate and is thus dominant. Initial evidence for drift-Alfvén waves in the experiment can be seen by examining the spectra of the fluctuations peaking on the pressure gradient region. As seen in Figure 3.3, the spectra appears to have semi-coherent low-frequency peaks that are suggestive of low-m drift-Alfvén waves.

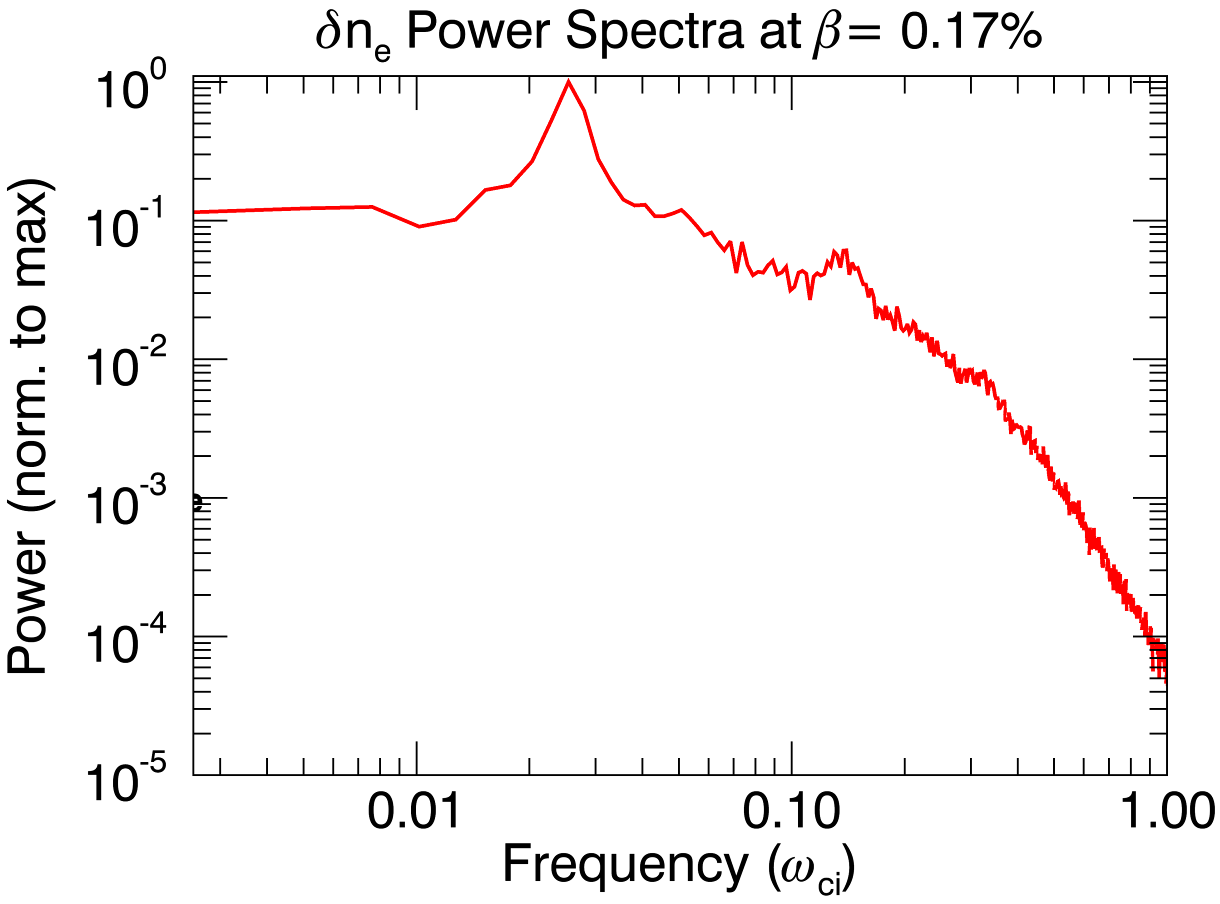

Figure 3.3: FFT of density fluctuations for the lowest β = 0.17% condition located at r = 5cm from Figure 3.2. Semi-coherent peaks in the spectra at 0.025, 0.15, and $0.3\omega_{ci}$ are suggestive of m = 1,2, and 3 modes respectively.

Expanding the analysis to magnetic fluctuations in the parallel and perpendicular directions

($\delta B_{\parallel}, \delta B_{\perp}$), Figure 3.4 shows these magnetic profiles overlaid on top of the mean density profile and density temporal root-mean-square (RMS) fluctuations. A slight increase in $\delta B_{\perp}$ fluctuations are observed to be localized to the core of the plasma with an even smaller increase in $\delta B_{\parallel}$ fluctuations in a similar region.

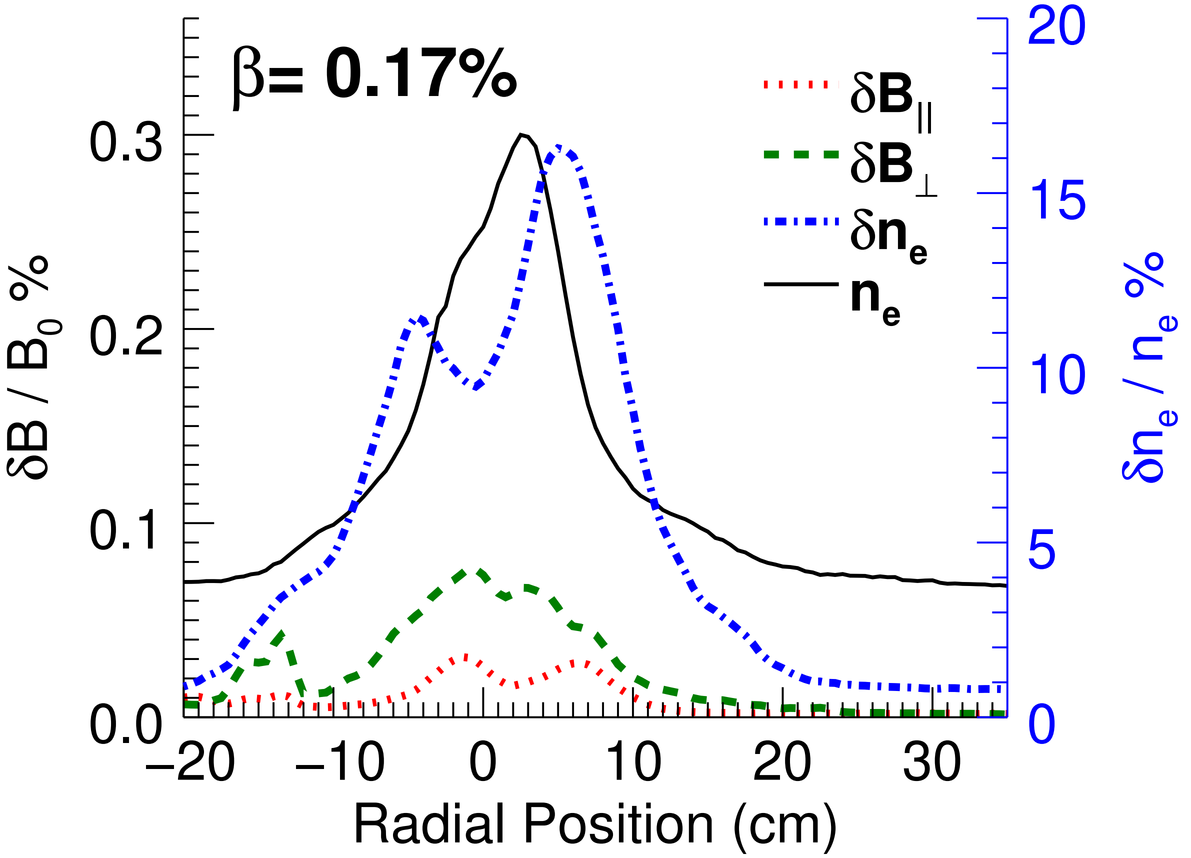

Figure 3.4: Mean density radial profile and density / magnetic RMS fluctuation profiles at a low plasma $\beta = 0.17\%$. δn_e fluctuations are localized to the gradient region while a slight concentration of $\delta B_{\perp}$ fluctuations are localized to the core.

As a side note, one might immediately notice that there seems to be slight asymmetry in the fluctuation profiles between the left ($r < 0$) and right ($r > 0$) of the cathode source, as well as the center of the density profile being slightly shifted to the right. This asymmetry is two fold; the left vs. right difference in amplitude of fluctuation profiles is due to perturbing nature of the diagnostic probes. Diagnostics enter from the $r = 30$ side and must traverse the entire plasma column to measure the $r = -20$ side of the dataset. Since having too many diagnostics or length of diagnostics in the plasma column has been shown to disrupt and mitigate instabilities, data analysis will focus on the $r > 0$ region. The density profile being slightly off-center at $r = 3$ is due to the engineering mechanics of the LaB$_6$ source. As previously mentioned, in order to allow for probe alignment the LaB$_6$ source is movable and thus there are slight errors on the order of cm in getting it to the exact center of the machine. Fortunately, the axial magnetic field is mostly uniform throughout the device and with the total diameter of the machine being 100 cm, this 3% shift should be negligible. Additionally, probe alignment is only required at the beginning of the experiment, so the source remains in same position for all data taken afterwards and thus all the data discussed in this thesis should be self-consistent.

3.2 Turbulence at Higher β

By using the technique described in Section 2.3, β is sequentially increased up to $\approx 15\%$ and changes to the plasma are documented for many intermediate cases of core β. Much of analysis will focus on four β conditions $(0.17\%, 1.1\%, 3.1\%, \text{and} 8.4\%)$ that were chosen to highlight key changes in the turbulence as the relative amplitudes between $\delta B_{\|}, \delta B_{\perp}$, and δn_e change with β.

3.2.1 Diamagnetic Corrections to B_0

A key indicator of achieving higher β plasmas is the presence of a diamagnetic response. For this experiment, a magnetic pick-up probe was used to measure the low-frequency variation of the background magnetic field due to diamagnetism; time traces of the the reduction of the magnetic field in the core plasma at four different β are shown in Fig. 3.5 with the reduction becoming more prominent with increasing β. Radial profiles of the background magnetic fields, including their diamagnetic reductions, at different β are represented as the magnetic pressure ($P_{mag} = \frac{B_0^2}{2\mu_0}$) in Fig. 3.6. By also overlaying the plasma pressure ($P_{plasma} \approx n_e t_e$) and total pressure ($P_{plasma} + P_{mag}$)

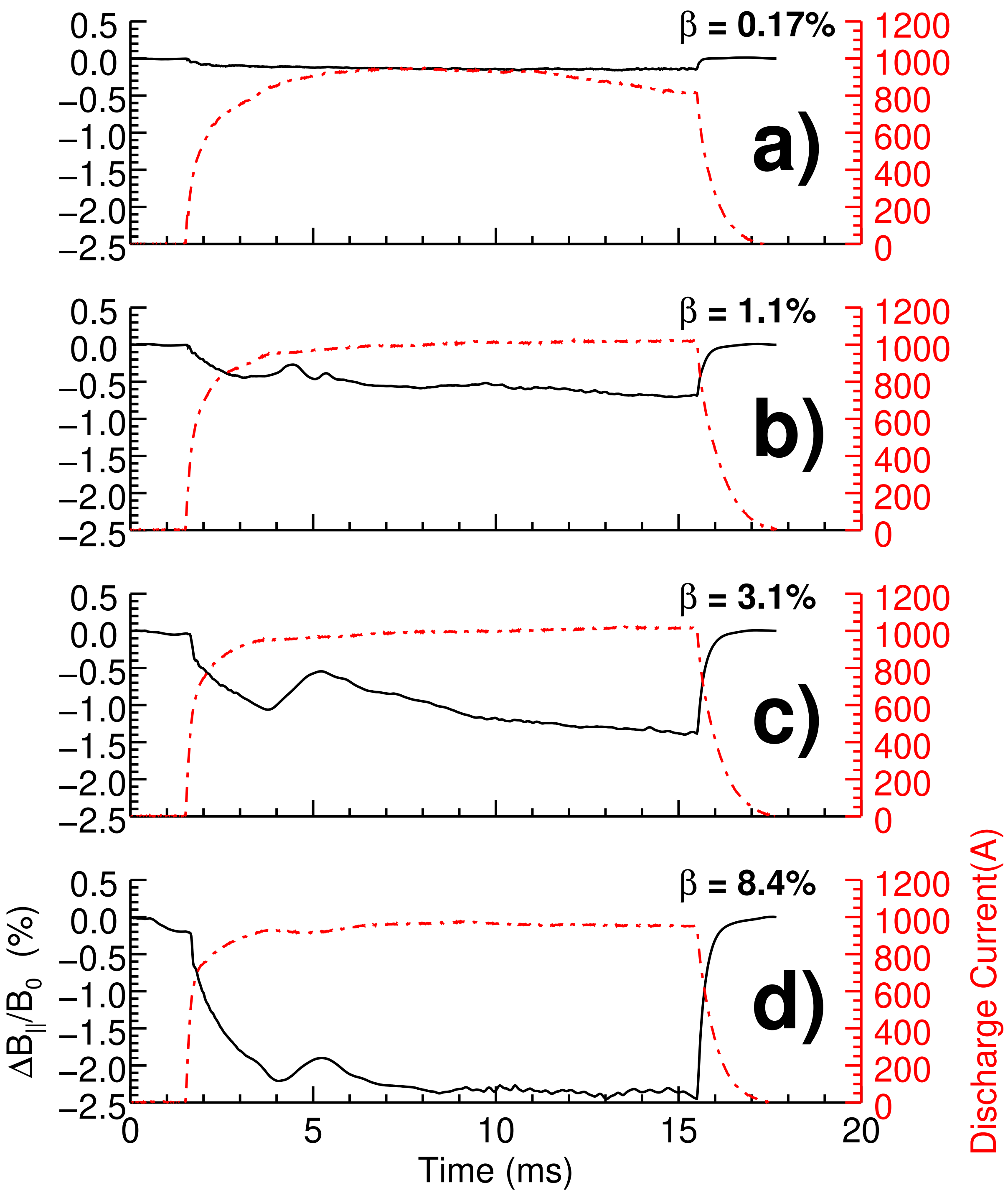

Figure 3.5: Time traces of normalized diamagnetic reductions to the background field (solid line) and discharge current to the LaB_6 cathode source (dashed line) at 4 different plasma β conditions, a) 0.17%, b) 1.1%, c) 3.1%, and d) 8.4%. Reduction increases with β

one can confirm that zeroth order radial pressure balance:

$$P_{plasma} + P_{mag} = constant \tag{3.1}$$

is satisfied to within 2%.

One can also look at the time evolution of pressure balance as seen in Figure 3.7. With the exception of the immediate beginning and end of the discharge, total pressure balance is seen to be conserved. Also of note, the $\delta B_{\parallel}$ fluctuation amplitude grows with β. At the highest $\beta = 8.4\%$, fluctuations are not seen to develop until the later half of the discharge, which also corresponds to the time period used when temporally averaging different quantities.

3.2.2 Mean Profiles

Zeroth order changes to the profiles of the mean plasma density and electron temperature for different values of core beta (different values of applied magnetic field) can be seen in Figure 3.8. The core plasma density and steepness of the edge gradient are similar for all beta values. Electron temperature grows significantly in width as lowering B_0 in the center of the machine while holding B_0 constant at the cathode sources to reach higher β causes flaring. As mentioned previously, a slight asymmetry in the profiles can be attributed to the perturbing nature of probe effects with a small target plasma. Diagnostics enter from the $r = 30$ cm side and must traverse the entire plasma column to measure the $r = -20$ cm side of the dataset. Thus, the majority of analysis in this thesis will focus on the right side of the column where $r > 0$ cm.

3.2.3 Fluctuation Profiles

The same analysis of fluctuation profiles at the lowest $\beta = 0.17\%$ condition in Figure 3.4 is now extended to a higher value of $\beta = 1.1\%$ in Figure 3.10. Here the same peak in density fluctuations is observed to be localized to the maximum density gradient region, around $r = 8$ cm. Focusing on the magnetic fluctuation profiles, parallel magnetic fluctuations are more prominent and also localized to the density gradient whereas the perpendicular fluctuations grow and peak spatially

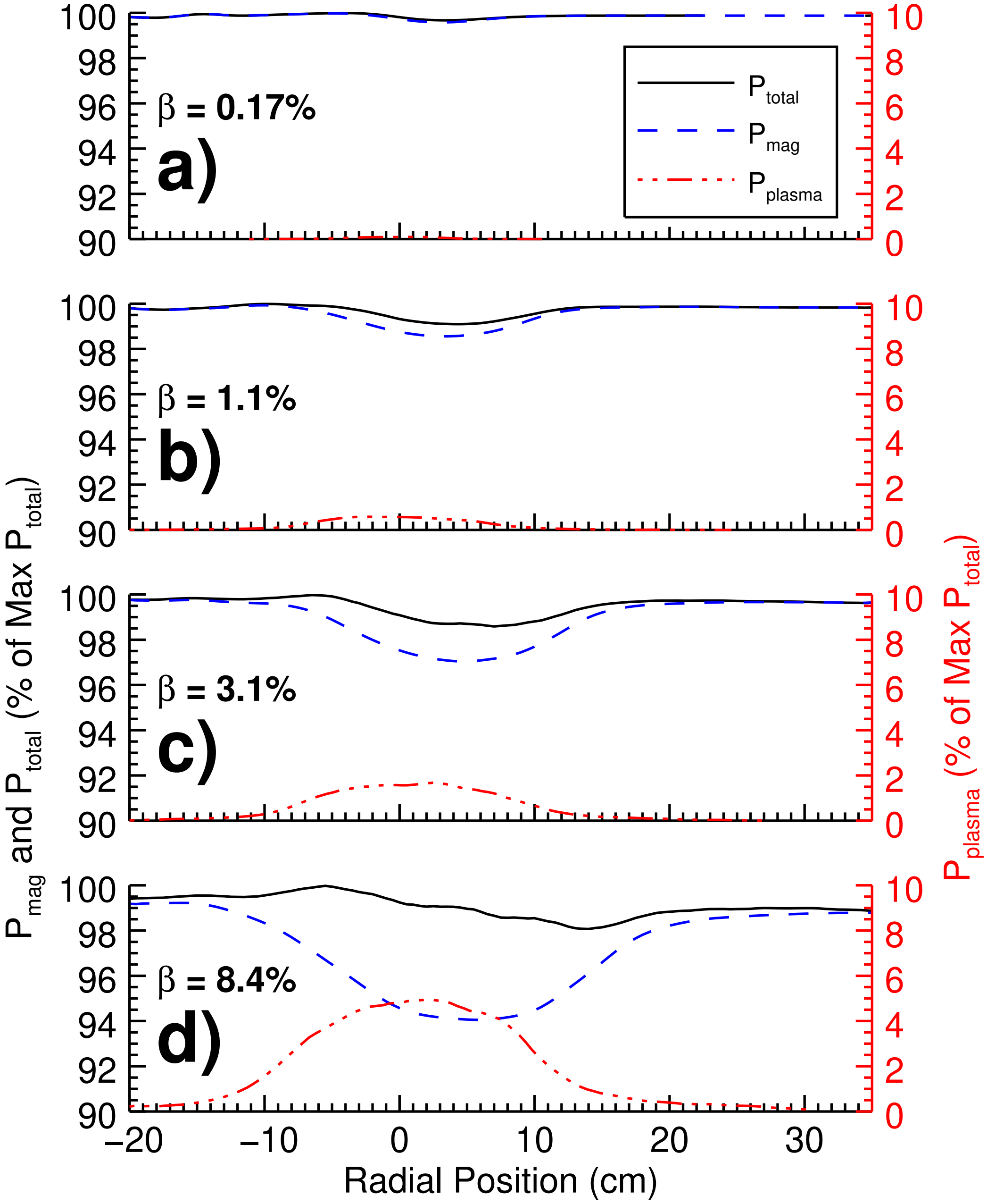

Figure 3.6: Radial profiles of magnetic and plasma pressure (dashed) as well as the sum (solid) normalized to the maximum total pressure at 4 different plasma β conditions, a) 0.17%, b) 1.1%, c) 3.1%, and d) 8.4%. Pressure balance holds (within 2%) as radial localization of increases in plasma pressure are matched with decreases in magnetic pressure.

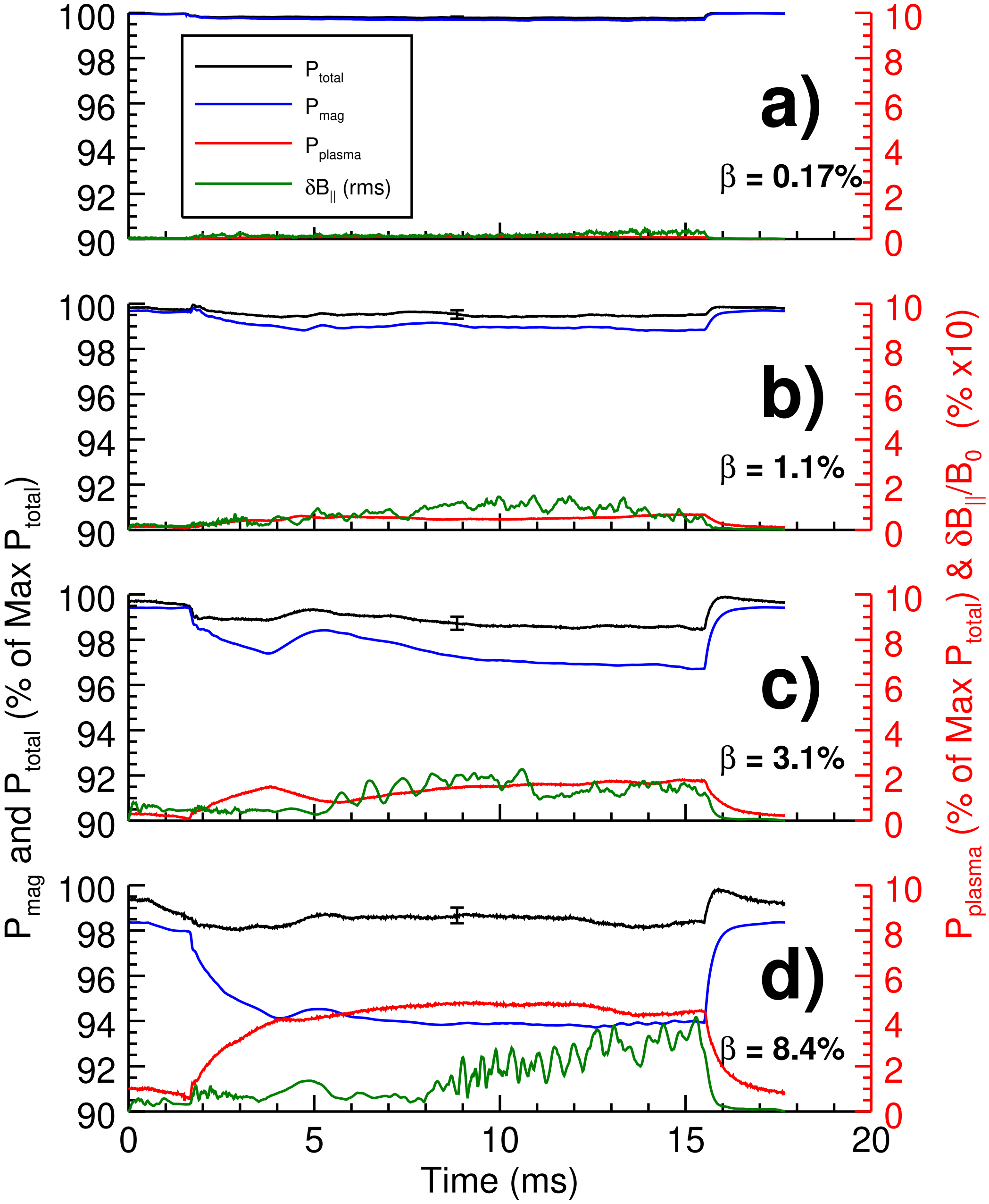

Figure 3.7: Time traces taken at core of magnetic (blue) and plasma pressure (red) as well as the sum (black) normalized to the maximum total pressure and RMS $\delta B_{\|}/B_0$ in the edge at 4 different plasma β conditions, a) 0.17%, b) 1.1%, c) 3.1%, and d) 8.4%. Pressure balance holds with $\delta B_{\|}$ fluctuations increasing with β and towards the end of the discharge.

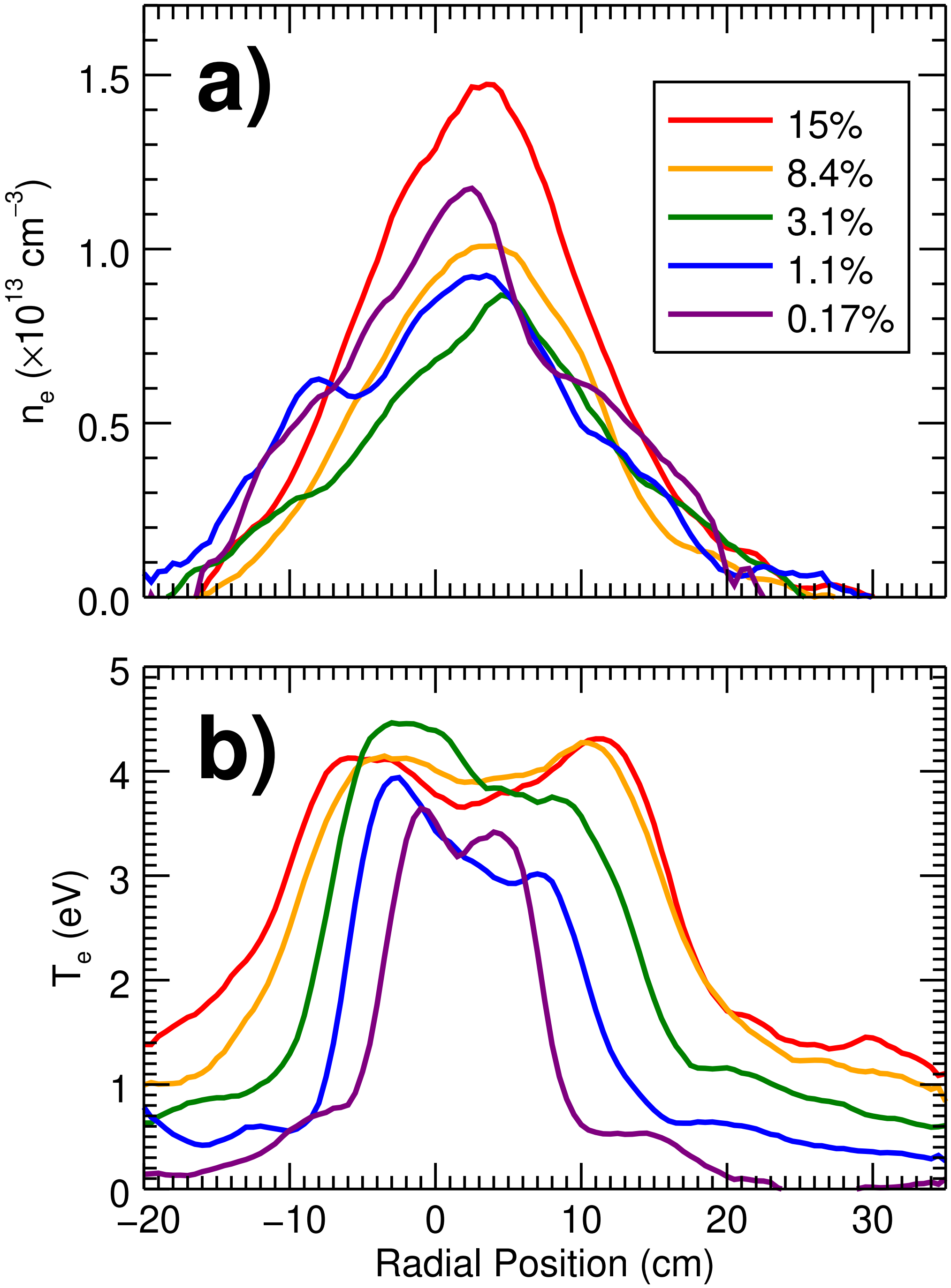

Figure 3.8: a) Density and b) electron temperature mean radial profile measurements for different values of core β. Core density is similar for all β whereas electron temperature grows significantly in width as the background field in the center of the machine is lowered to reach higher β.

closer to $r = 3$ cm. This location lines up with the peak in the density profile, what will be referred to as the core-region of the plasma.

Taking a quick look at the $\delta B_{\parallel}$ fluctuation spectra for $\beta = 1.1\%$, shown in Figure 3.9, reveals that most of the power is concentrated at a low frequency peak ($\omega \sim .003\omega_{ci}$ where ω_{ci} is the ion cyclotron frequency) with additional semi-coherent peaks at higher frequencies. Also shown in Figure 3.9, the fluctuation spectra for δn_e and $\delta B_{\perp}$ are also very similar to that of $\delta B_{\parallel}$ and strongly correlated. This suggests that while the radial localization is different for some fluctuating quantities, these fluctuations are created by the same global mechanism. This combination of correlated on-axis $B_{\perp}$ and off-axis $B_{\parallel}$ peaks is similar to low-m drift-Alfvén wave fluctuations.

As β is increased even further, as seen going from $\beta = 1.1\%$ in Figure 3.11b) to $\beta = 3.1\%$ in Figure 3.11c), the radial locations of the fluctuation peaks remain constant relative to the density profile. Focusing on the amplitude of the peaks, density fluctuations are seen to modestly decrease while both the parallel and perpendicular magnetic fluctuations increase with higher β. Of particular interest, at the highest β condition, as seen in Fig. 3.11d), the relative magnitude of $B_{\parallel}$ fluctuations exceeds that of $B_{\perp}$.

One can quantify the fluctuation amplitude trends by tracking the peak amplitude of the different types of fluctuations for additional intermediate plasma β conditions. As shown in Fig. 3.12a), this analysis demonstrates that both parallel and perpendicular fluctuations increase rapidly with increasing β until they diverge from one another at $\beta \sim 2\%$. For $\beta > 2\%$ peak parallel fluctuation level continues to increase, albeit at a slower rate, while perpendicular fluctuations saturate and remain mostly constant until reaching the highest $\beta > 10\%$ conditions of the data set.Figure 3.12(b) quantifies this trend by analyzing the ratio of parallel to perpendicular magnetic RMS (temporal) fluctuation levels. This ratio is shown to grow beyond order unity for $\beta \geq 2\%$ and reach a factor of 2 at the highest β.

3.2.4 2D Structure

Core-localization of perpendicular magnetic fluctuations is consistent with previous observations of low-m drift-Alfvén waves in smaller plasma columns in LAPD [2]. One can demonstrate that

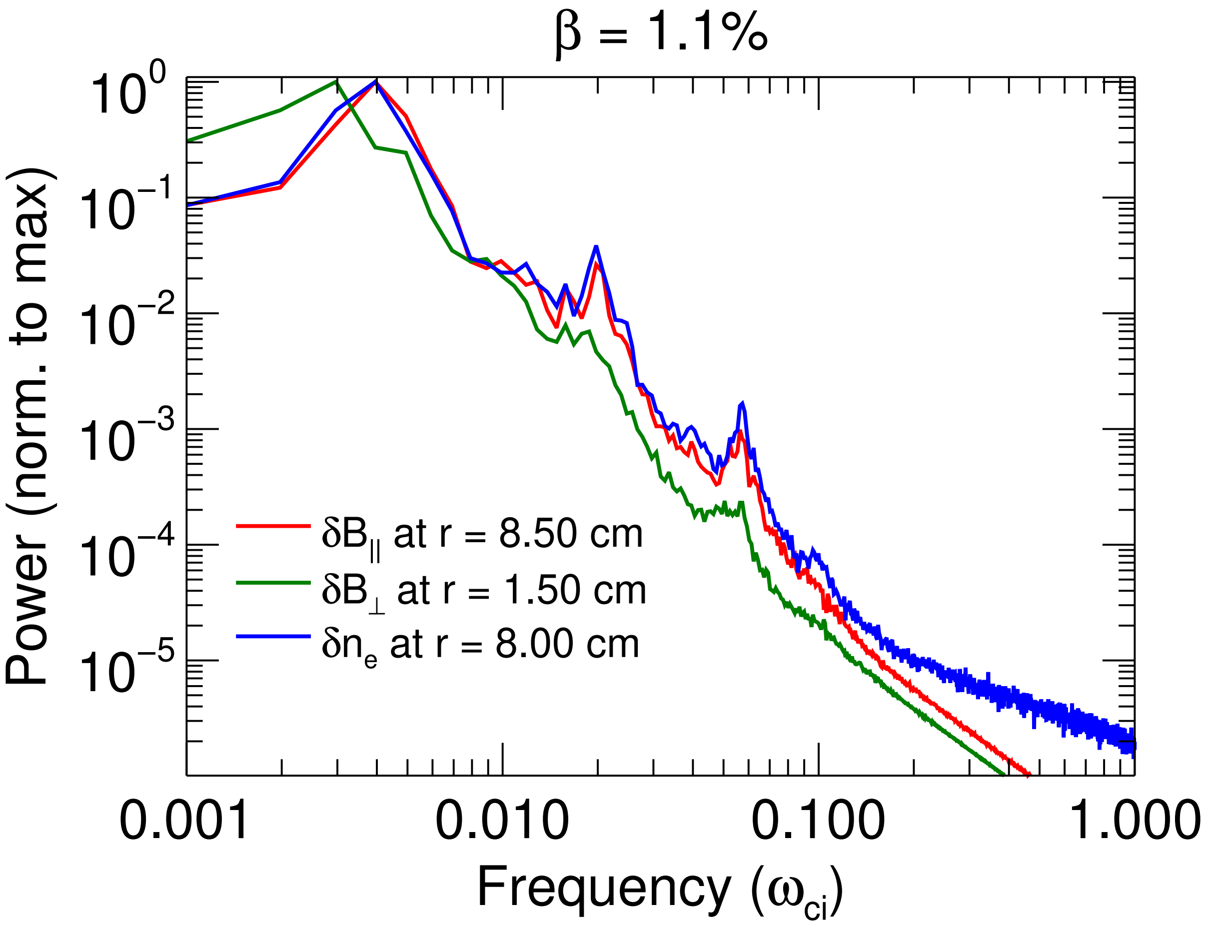

Figure 3.9: Power spectra of $\delta B_{\|}$, $\delta B_{\perp}$, and δn_e fluctuations for $\beta = 1.1\%$ condition taken at radial locations of peak power. Despite the different radial localization, spectra are very similar between the three diagnostics.

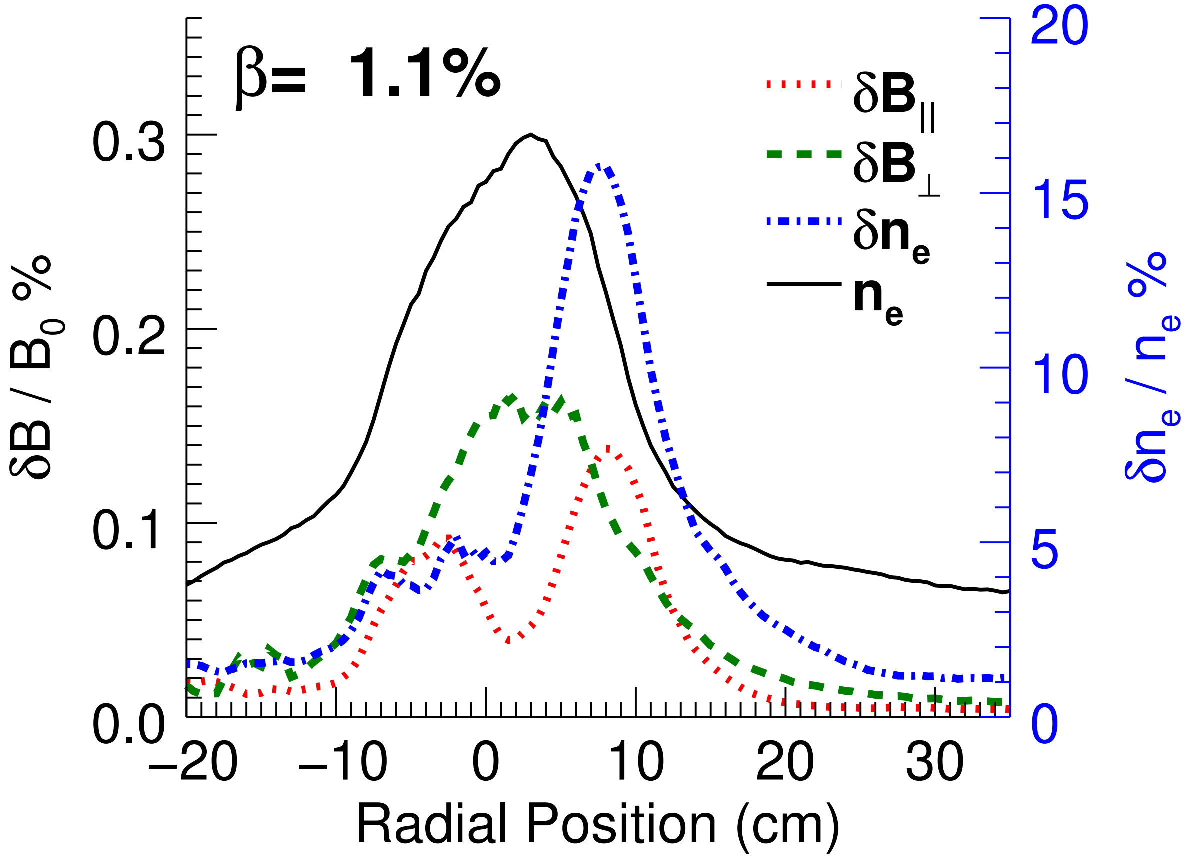

Figure 3.10: Mean density radial profile and density / magnetic RMS fluctuation profiles at a slightly higher plasma $\beta = 1.1\%$. $\delta B_{\|}$ fluctuations are now prominent localized to the gradient region with δn_e fluctuations. $\delta B_{\perp}$ fluctuations have also grown and are still localized to the core.

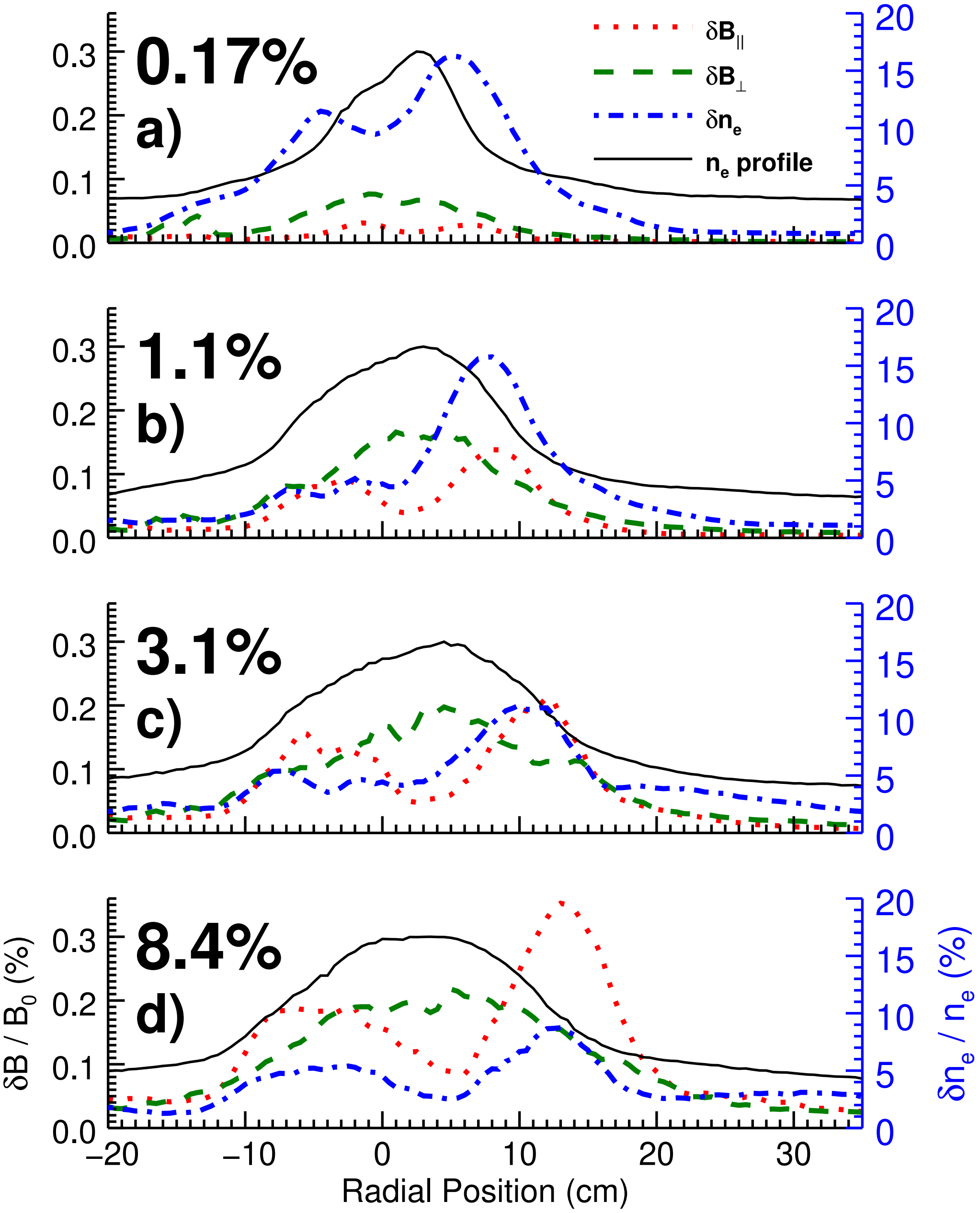

Figure 3.11: Mean density radial profile and density / magnetic RMS fluctuation profiles at 4 different plasma β conditions,a) 0.17%, b) 1.1%, c) 3.1%, and d) 8.4%. $\delta B_{||}$ and δn_e fluctuations are localized to the gradient region while $\delta B_{\perp}$ fluctuations are localized to the core for all β conditions.

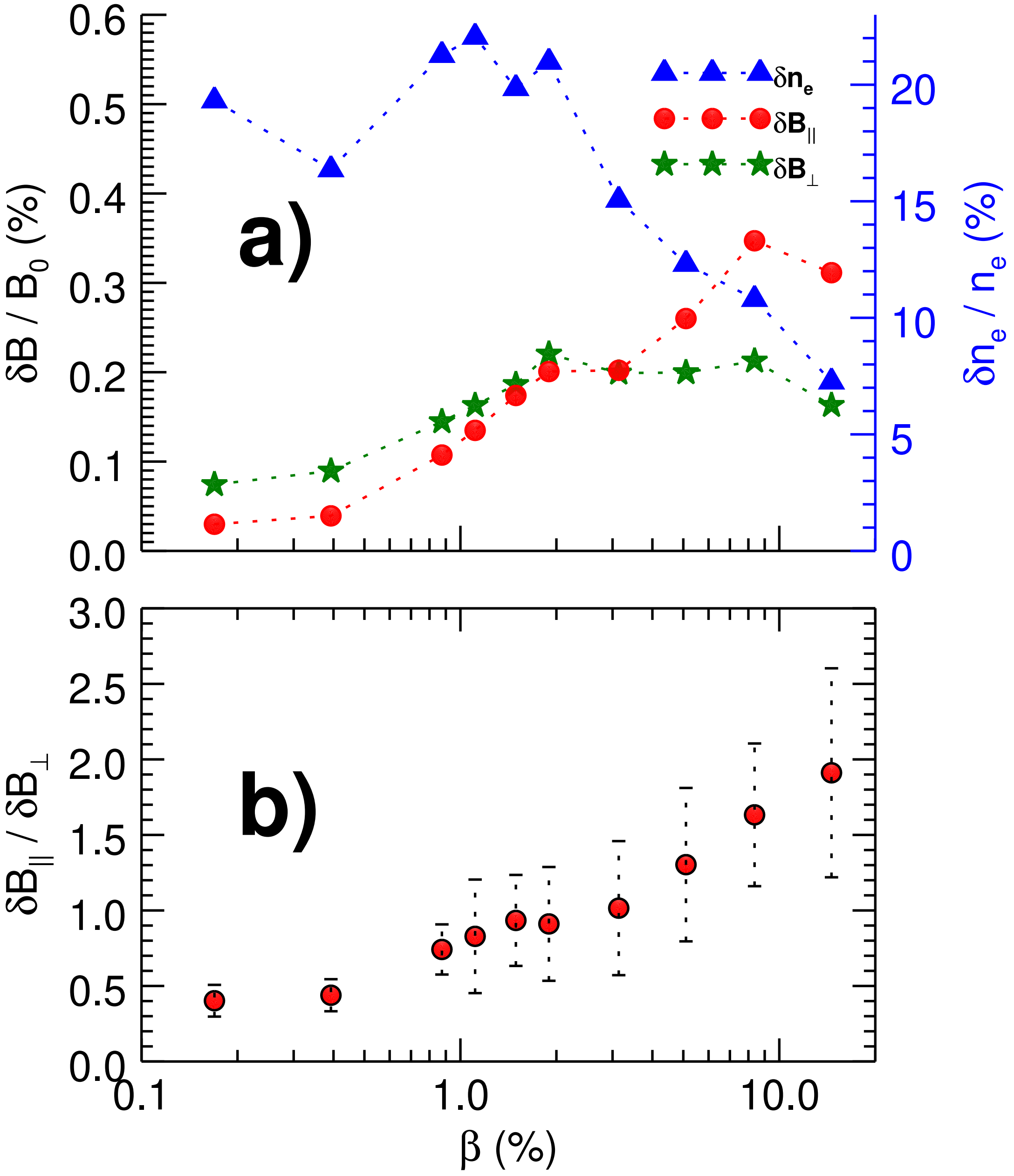

Figure 3.12: a) Peak RMS fluctuation levels for magnetics and density as a function of plasma β. Here $\delta B_{\parallel}$,$\delta B_{\perp}$ grow with β while δn_e decreases. b) Ratio of parallel to perpendicular magnetic peak RMS fluctuation power which also increases with β.

the observed fluctuations are low-m cylindrical eigenmodes by looking at the spectral 2D cross correlation C_{spec} between the different magnetic directions at the low frequency ($\frac{\omega}{\omega_{ci}} \ll 1$ where ω_{ci} is the ion cyclotron frequency) peaks seen in Fig. 3.13d). This zero time-delay correlation function is computed in terms of an integral over the cross-spectrum between the time series of a stationary reference probe (I_{ref}) and an axially offset moving probe (I_{mov}) for frequency bandwidths $[\omega - \delta, \omega + \delta]$. The function is as follows:

$$C_{spec}(x,y,\omega) = 2\int_{\omega-\delta}^{\omega+\delta} \|\tilde{I}_{ref}(x,y,\omega)\| \|\tilde{I}_{mov}(x,y,\omega)\| \cos(\theta)\gamma d\omega \tag{3.2}$$

whereby $C_{spec}(x,y,\omega)$ is normalized by C_{max} for the 2D plane, θ is the spectral crossphase between I_{ref} and I_{mov} fluctuations, and γ is the coherency between the two signals. Frequency bandwidths are small ($\delta = 0.0012\omega_{ci}$) in order to isolate specific modes.

Using this technique for $\beta = 1.1\%$, Figure 3.13a demonstrates that the $B_{\|}$ structure is localized to the gradient edge region of the plasma, consistent with an m = 1 eigenmode. This structure is coherent for higher frequency modes such as m = 2 and m = 3 seen in Figure 3.13b and Figure 3.13c respectively. Figure 3.14a shows $B_{\perp}$ fluctuation power localized to the core of plasma while computing the parallel current $J_{\|} = \nabla \times B_{\perp}$ in Figure 3.14b shows distinct current channels localized on the density gradient. These observations are consistent with previous observations of a low-m drift-Alfvén wave, see Figure 1.3, as will be shown in more detail below.

The ratios of relative amplitudes between potential and density fluctuations are also important for classifying the mechanism behind these fluctuations. For many of the common types of instabilities found in LAPD (Drift-waves, Kelvin-Helmholtz, Rotational interchange), it can be shown [24] that the ratio of $R = |\delta\phi/T_{e0}|/|\delta n_e/n_{e0}|$ varies. For drift-waves, this ratio should be ≤ 1 and for rotational interchange modes it should be > 1, while Kelvin-Helmholtz modes would be expected to have $R \gg 1$. It should be noted that these results are for linear modes and may not be accurate to compare to the saturated turbulence we measure in the steady-state region of the discharge.

In this experiment, measurements of plasma potential fluctuations ($\delta\phi$) were not able to be recorded directly so the floating potential fluctuations (δV_f) is used as a proxy. This approximation is valid provided that δT_e fluctuations are small. Figure 3.15 shows a radial profile of the ratio of

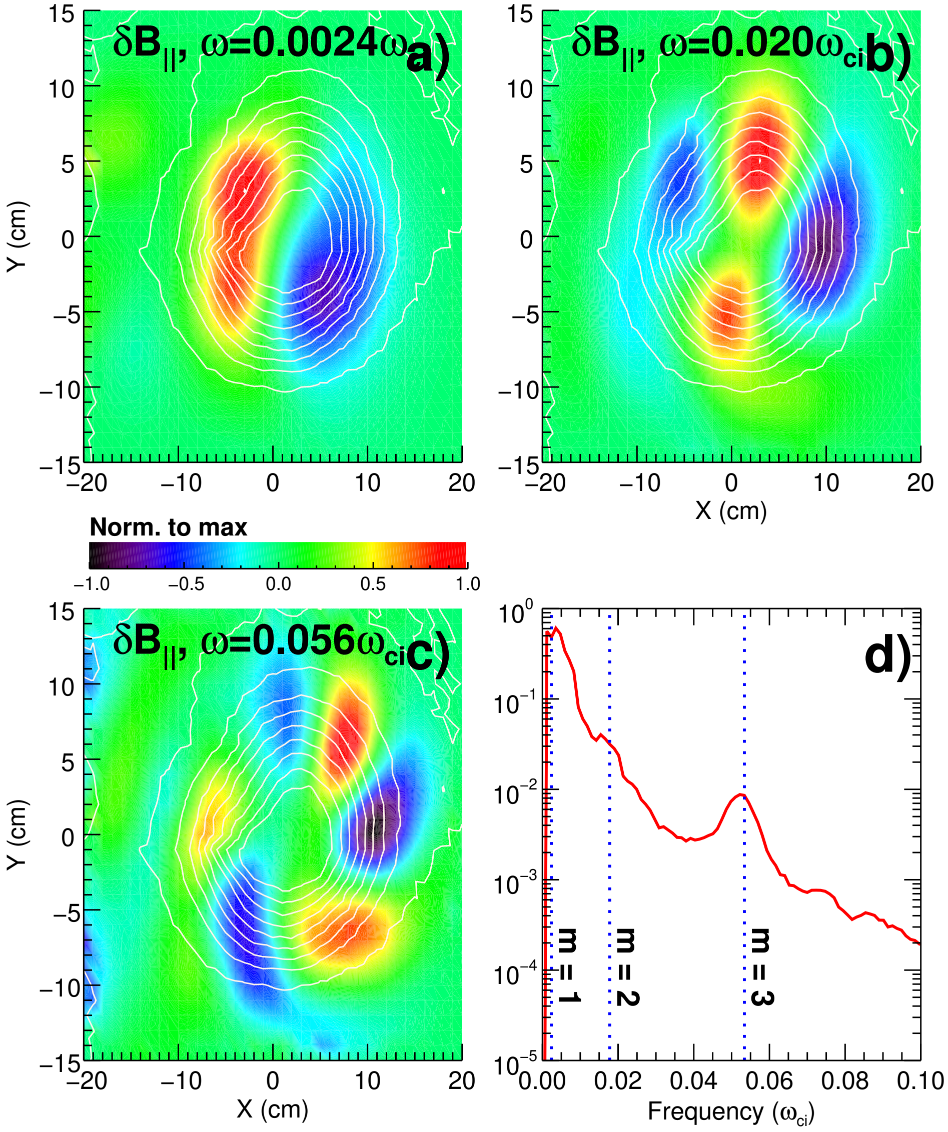

Figure 3.13: a) Cross-spectral power between a moving $B_{||}$ and stationary n_e probe at $\beta = 1.11\%$ for a) $\omega \approx 0.0024\omega_{ci}$ showing a coherent m = 1 structure, b) $\omega \approx 0.020\omega_{ci}$ showing an m = 2 structure, and c) $\omega \approx 0.056\omega_{ci}$ showing an m = 3 structure. The contour lines map out the density profile. A normalized FFT spectra of the stationary n_e fluctuations is provided in d) showing the locations in frequency-space of the different mode numbers.

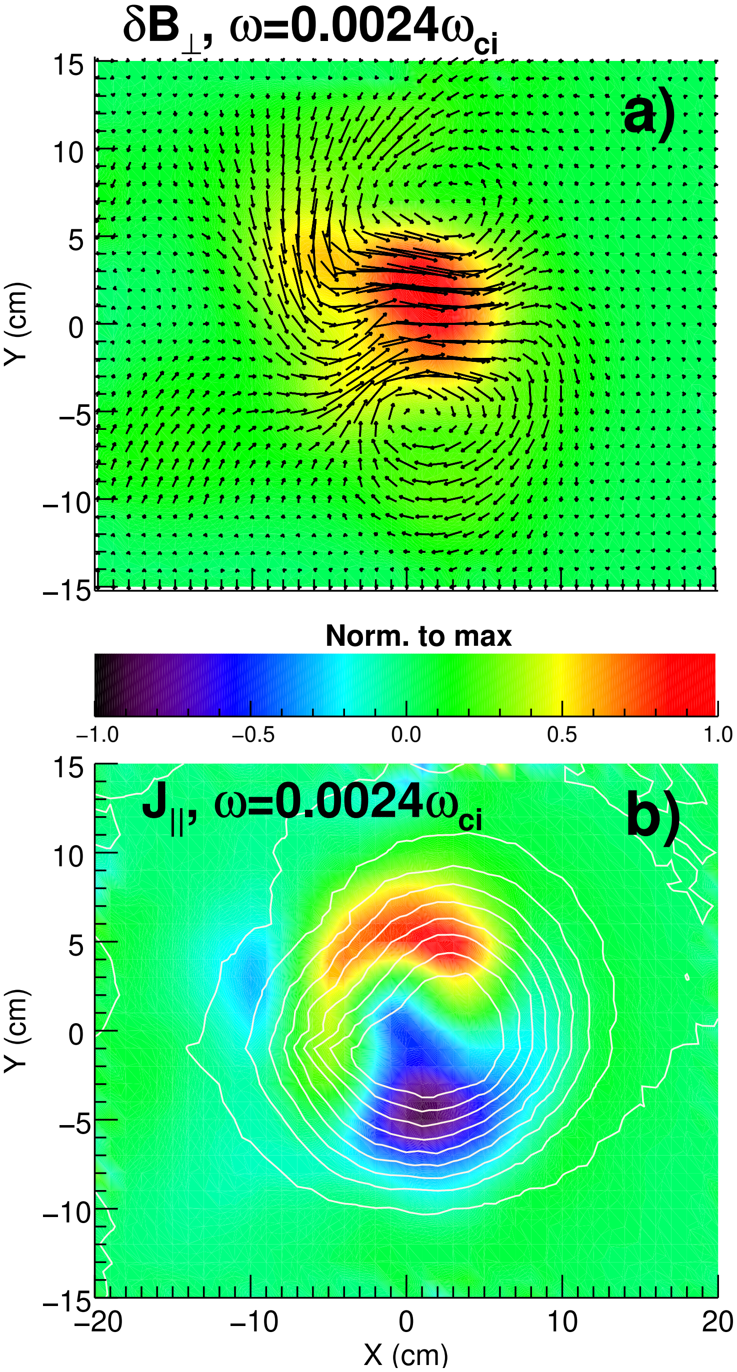

Figure 3.14: a) Cross-spectral power between a moving $B_\perp$ and stationary n_e probe at $\beta = 1.1\%$ for $\omega \approx 0.0024\omega_{ci}$ with B_x, B_y vectors on top. Pattern matches the expected core localization for a drift-Alfvén wave. b) Parallel current calculated from $\nabla \times \mathbf{B}_\perp$ that matches the expected current channels on the density gradient. The contour lines map out the density profile.

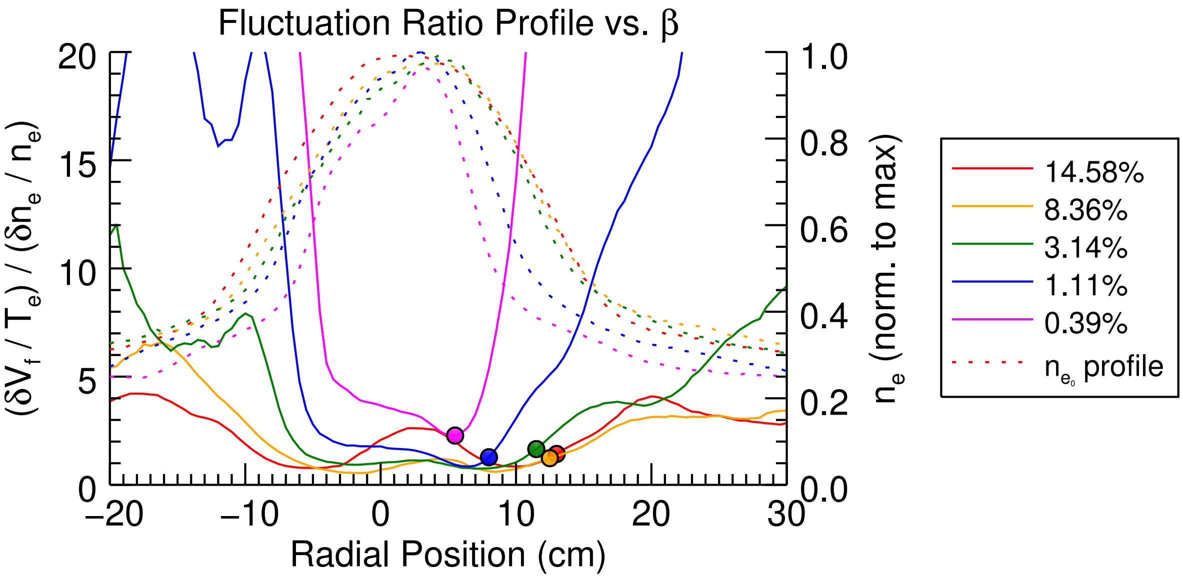

Figure 3.15: Radial profile of ratio of relative floating potential fluctuations to density fluctuations at different β. The dashed lines represent the density profiles for the respective β states normalized to the maximum density amongst all β. Points represent the radial location corresponding to the highest n_e fluctuations similar to Figure 3.2.

floating potential fluctuations scaled to the temperature profile over density fluctuations scaled to their respective density profiles. One can observe that this ratio is close to 1 for regions close to the core and gradient region for each β. At the the lower β conditions this ratio increases dramatically outside of the gradient region and is mostly due the lack of flaring at lower β that provides a substantial $T_e > 0$ further out radially for the higher β plasmas. One can now quantify how this ratio changes with β by picking out the value of the ratio $R = |\delta\phi/T_{e_0}|/|\delta n_e/n_{e_0}|$ for many different β conditions at their respective peak density gradient radial locations. As seen in Figure 3.16, starting at the lowest β the ratio is slightly greater than unity. However, as β is increased the fluctuation ratio decreases to a local minimum at $\beta = 2\%$ with $(\delta V_f/T_{e_0})/(\delta n_e/n_{e_0}) \approx 1$. As β increases even further the ratio has a slight increase while saturating close to ≈ 1.5. From the discussion of the significance of the ratios before [24], due to the ratio being close to unity, this instability has more resemblance to a drift-wave whereas had the ratio been much greater than unity (> 20), the instability may be classified more as Kelvin-Helmholtz or rotational interchange.

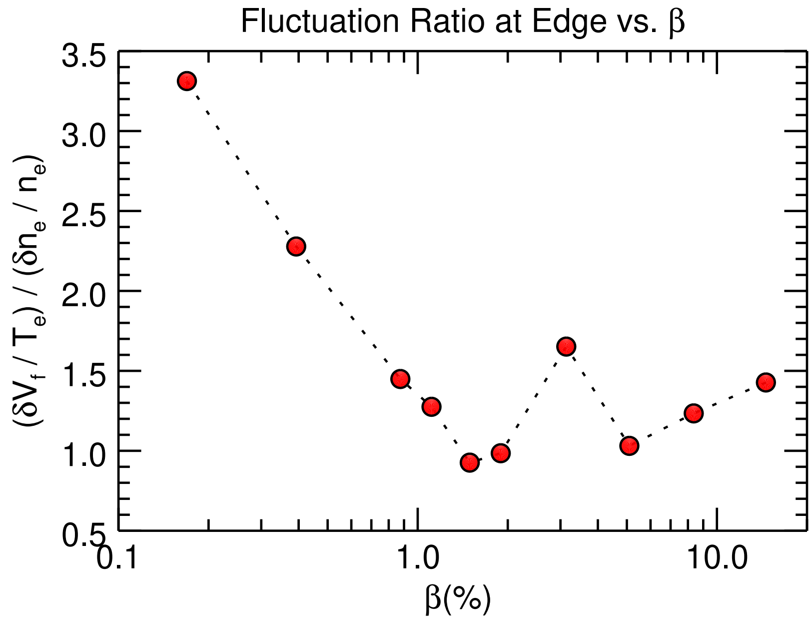

Figure 3.16: Ratio of floating potential fluctuations to density fluctuations vs. β. Ratio is taken at the radial position corresponding to the highest δn_e fluctuations, or the points in Figure 3.15

3.2.5 Spectral Analysis

Characterizing this unique growth of $B_{||}$ fluctuations, changes in fluctuation spectra at different β conditions are analyzed. Fig. 3.17 shows how low frequency fluctuations are dominant for all β conditions. At the lower β there are multiple higher frequency peaks which correspond to the higher m-number mode structures such as the m = 3 seen in Fig. 3.13b.As β increases, these multiple higher frequency peaks disappear and a single coherent peak at $\approx .02\ \omega_{ci}$ arises.

3.3 Transport Analysis

Another important metric for turbulent plasmas is the changes to transport with β. One can calculate the relative electrostatic particle flux by performing a spectral correlation between the density fluctuations δn_e and the radial velocity fluctuations δv_r due to azimuthal electric field fluctuations assuming $E \times B$ flow. This correlation can be written as follows:

$$\Gamma_{ES} =< \delta n_e \cdot \delta v_r >= 2 \int_0^\infty \|\tilde{\delta n}_e(\omega)\| \|\tilde{\delta v}_r(\omega)\| \cos(\theta) \gamma d\omega \tag{3.3}$$

whereby θ is the spectral crossphase, $\tilde{\delta n}_e$ and $\tilde{\delta v}_r$ are Fourier transform, and γ is the coherency between δn_e and δv_r. Using this technique for many different β, as seen in Figure 3.18, it is shown that electrostatic particle flux decreases rapidly as β is increased. Upon analysis of the individual components, this seems to mainly be due to the decrease in fluctuation power for both δn_e and δv_r while cross-phase and coherency remain mostly constant with increasing β.

However, as seen in Figure 3.8, such dramatic differences in transport do not appear to cause any variation in the mean pressure profiles with increasing β. Thus, one can hypothesize that there must be other sources of transport responsible for counteracting a steepening of the pressure profile with the decrease of electrostatic flux.

One of the additional sources of transport that was able to be analyzed with the available diagnostics was cross-field electromagnetic transport due to perturbed via ∇B drifts. Electromagnetic

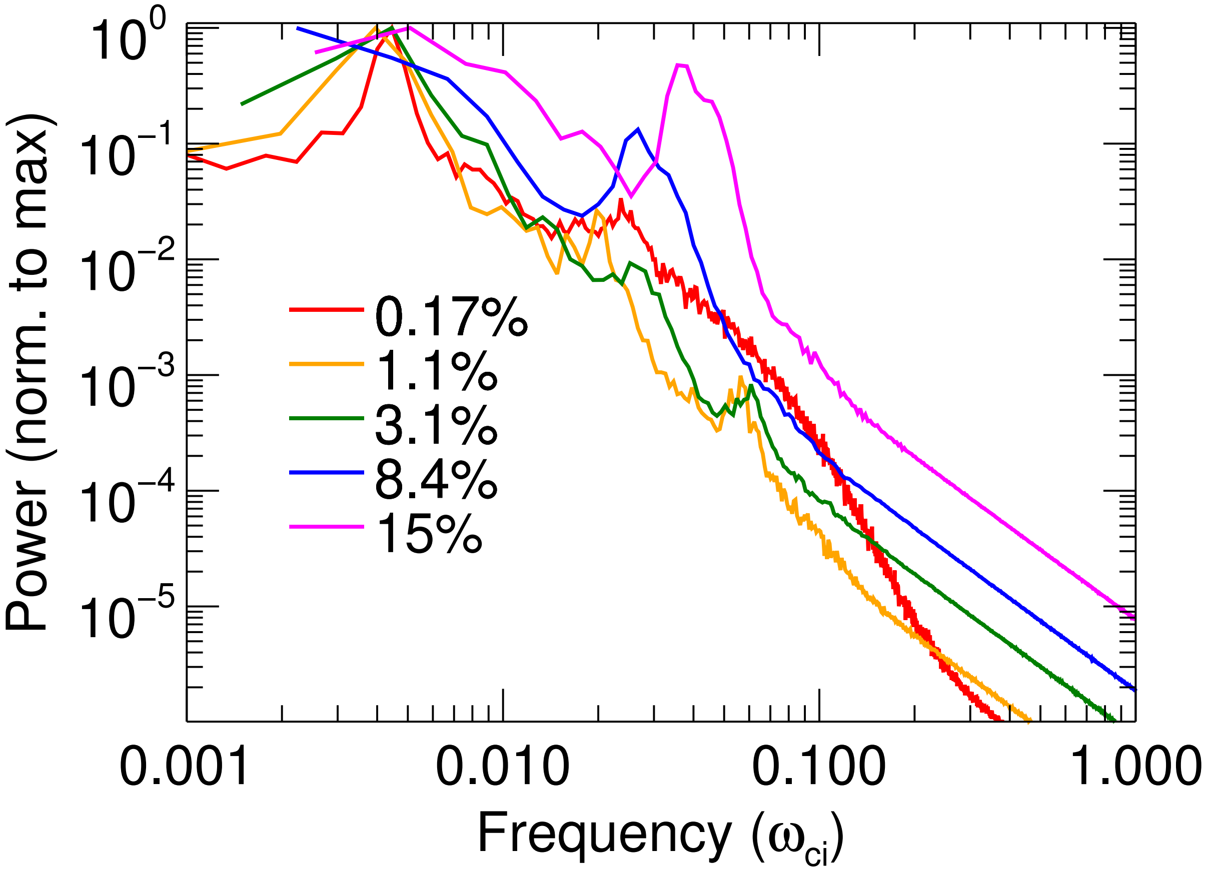

Figure 3.17: Power spectra of $\delta B_{\|}$ fluctuations for many β conditions. Most of the power is located at low frequency while peaks at higher frequencies grow in power with increasing β until the emergence a single higher frequency coherent peak ($\omega \approx 0.07\omega_{ci}$) at the highest β.

particle flux was calculated as follows:

$$\Gamma_{EM} = \frac{T_e}{B_0^2} \times < \delta n_e \cdot \delta B_{\parallel} > \tag{3.4}$$

whereby $< \delta n_e \cdot \delta B_{\parallel} >$ is the spectral correlation between density fluctuations δn_e and parallel magnetic fluctuations $\delta B_{\parallel}$, similar to Eq. 3.3, and T_e is the electron temperature in the gradient region. Eq. 3.4 is the simplified form of calculating $< \delta n_e \cdot v_{\nabla B} >$ whereby $v_{\nabla B}$ is the radial ∇B drift velocity defined as:

$$\mathbf{v}_{\nabla B} = -\frac{mv^2}{2qB^3} \nabla \delta B \times \mathbf{B}. \tag{3.5}$$

Since the zeroth order $\mathbf{B}$ points in the $\hat{z}$ direction, the component of $\nabla \delta B$ that points in the $\hat{\phi}$ direction is needed to determine $v_{\nabla B}$ in the radial direction. From Figure 3.13, it is seen that $\delta B_{\parallel}$ fluctuations are responsible for the azimuthal mode structure that would give rise to a finite $\nabla \delta B$ in the fluctuations. For these reasons one can use magnitude of $\delta B_{\parallel}$ as a proxy for $\nabla \delta B$.

Using this technique to calculate the electromagnetic flux for increasing β, as seen in Figure 3.19, shows an increase in electromagnetic flux that is counter to the electrostatic flux trend up to $\beta = 2\%$. While this supports the hypothesis that electrostatic and electromagnetic flux are inversely proportional to maintain the pressure profiles, it is unable to hold past $\beta = 2\%$ as the electromagnetic flux decreases and with a modest increase at the highest β. While it is not entirely known why this phenomena occurs, it could be due to FLR-effects as the Larmor radius approaches the size of plasma column such that theory of transport used in these calculations breaks down. Also at the highest β where the total flux is lower than expected, classical transport should dominate and be responsible for maintaining the pressure profiles.

3.3.1 Dynamic Pressure Balance

One physical mechanism for generation of parallel magnetic field perturbations is perturbed diamagnetic currents that arise due to density fluctuations in an increased β plasma. This mechanism is equivalent to dynamic pressure balance between the magnetic and plasma pressure fluctuations.

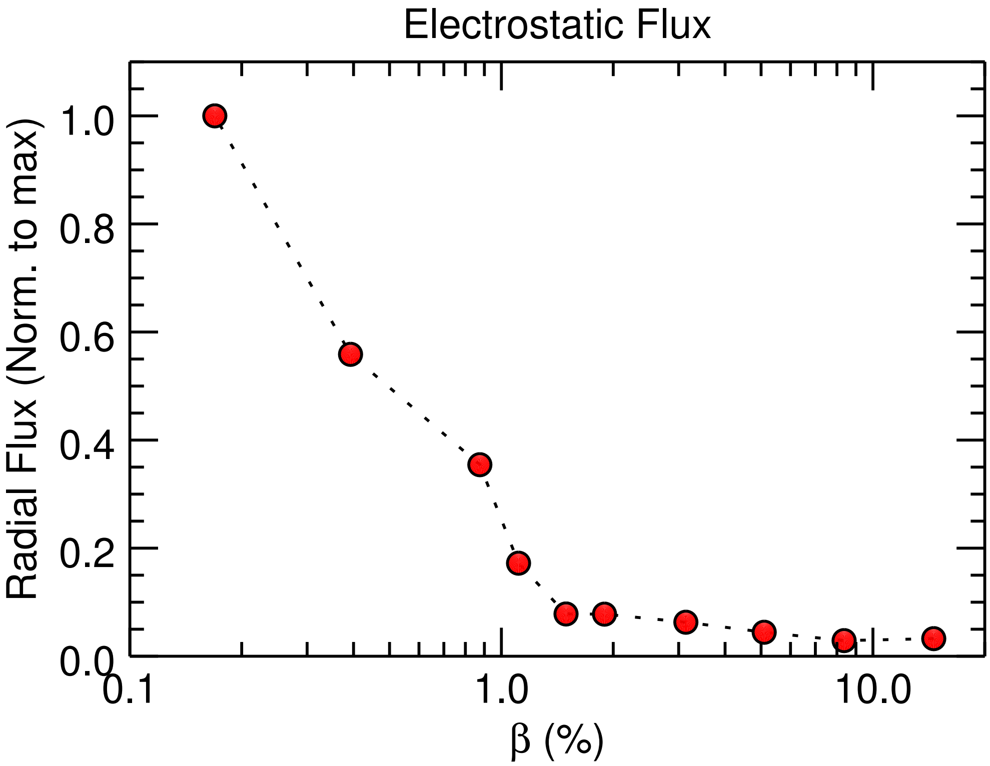

Figure 3.18: Normalized electrostatic particle flux, Γ_{ES}, from $< \delta n_e \cdot v_r >$ where v_r is the radial flow from $\delta E_\phi \times \mathbf{B_0}$

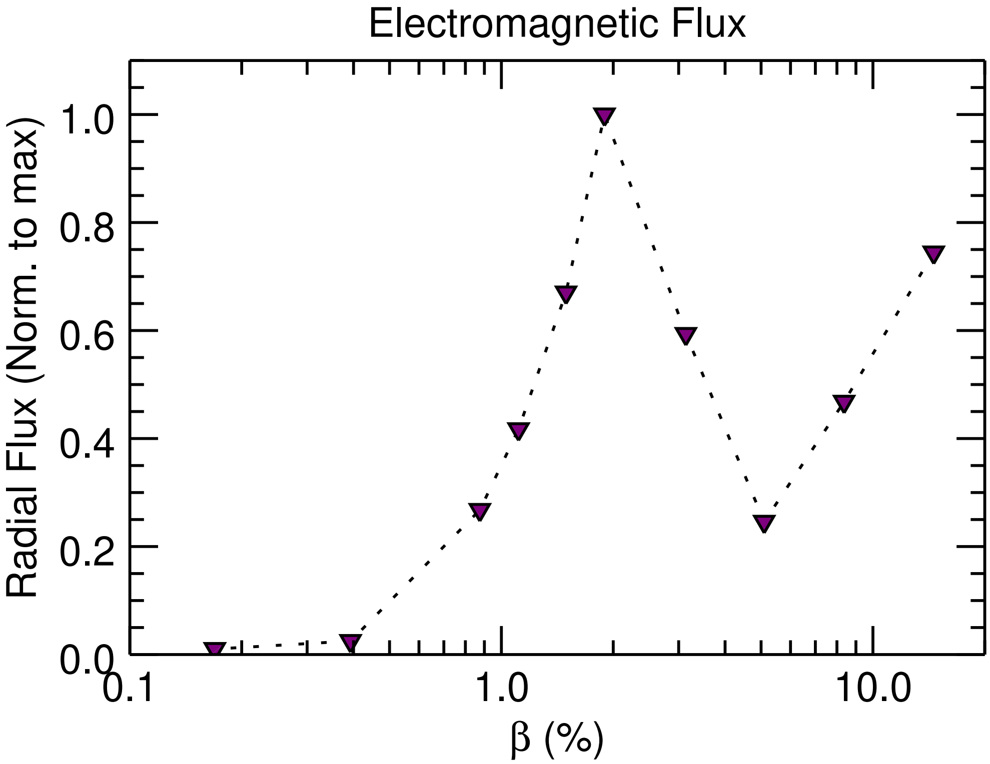

Figure 3.19: Normalized electromagnetic particle flux, Γ_{EM}, as calculated in Eq. 3.4.

For this experiment pressure balance is defined as

$$P_{plasma} + \frac{B_0^2}{2\mu_0} = constant, \tag{3.6}$$

which for fluctuating quantities implies that

$$\frac{\delta P}{B_0^2/\mu_0} = -\frac{\delta B_\parallel}{B_0} \tag{3.7}$$

such that

$$\frac{\delta(n_e T_e)}{B_0^2/\mu_0} = -\frac{\delta B_\parallel}{B_0}. \tag{3.8}$$

From Eq. 3.7 it is predicted that $B_\parallel$ and δP fluctuations should be out of phase by π radians with one another and that the left and right side should be on the same order of magnitude. Fig. 3.20 confirms this with $\delta P/(B_0^2/\mu_0)$ and $\delta B_\parallel/B_0$ having the correct sign and having a fairly good linear fit to the predicted 1:1 relationship.

The prediction in Eq. 3.8 can be further validated by looking at cross-correlation functions between $\delta B_\parallel$ and δn_e fluctuations. Fig. 3.21a) shows the same spectral band passed cross-correlation function, C_{spec}, from Fig. 3.13 between two n_e probes located 5 meters apart in the axial direction at $\beta = 1.1\%$. One probe is stationary on the density gradient at $r = 10$ cm while the other traverses the plasma column in the XY plane and the signals are correlated to one another using the same technique as Eq. 3.2.

The area outlined by the black dotted line indicates the location of the stationary probe $(x_{\text{ref}}, y_{\text{ref}})$ as it is the location of highest correlation. Fig. 3.21b) uses the same stationary probe as Fig. 3.21a) but is instead correlated to a moving $B_\parallel$ probe located 5.5m away axially. As seen from the outlined circle, which represents the position of the stationary n_e probe, the fluctuations between $B_\parallel$ and n_e appear to be highly anti-correlated. This is consistent with the theory of pressure balance.

One can now compute $C_{spec}(x_{\text{ref}}, y_{\text{ref}}, \omega)$ at the location of the stationary n_e probe for a larger frequency range. Doing so allows for the individual contributions such as the coherence γ and phase difference θ between $B_\parallel$ and n_e fluctuations at all frequencies to be quantified. As seen in Fig. 3.22a), there are a few semi-coherent peaks on top of a broadband spectrum which are primarily due to the corresponding peaks in cross-coherence between the two signals as seen in Fig. 3.22b).

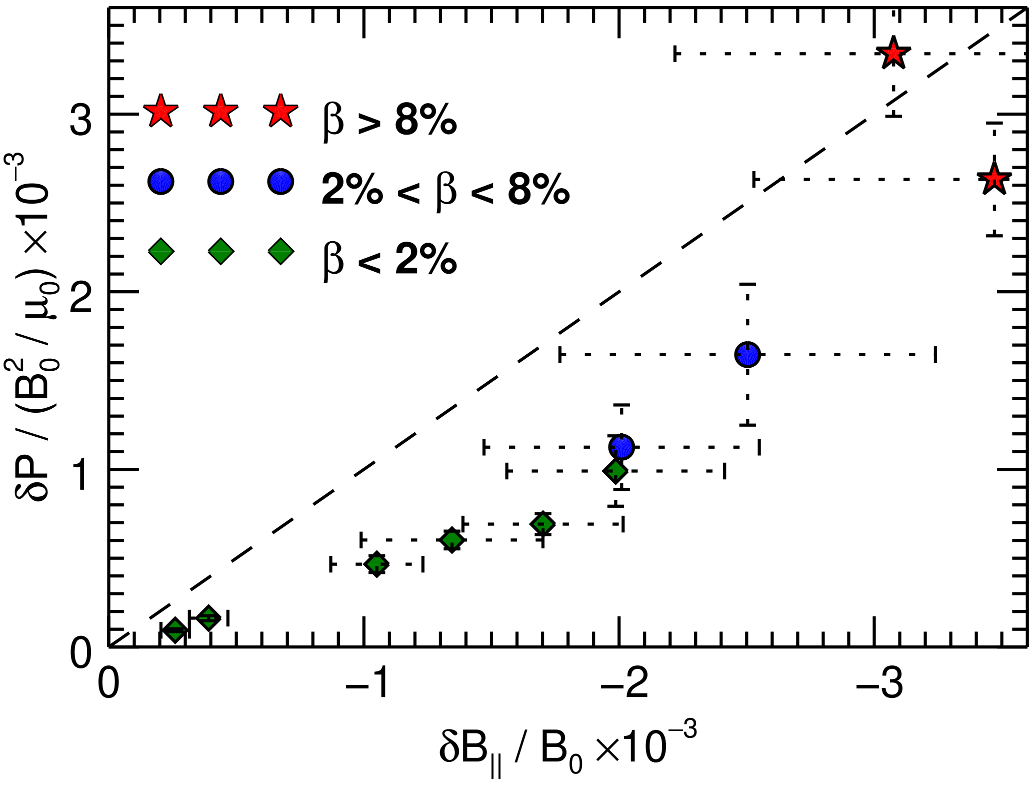

Figure 3.20: Pressure balance, $\delta P({B_0}^2/\mu_0)$ vs. $\delta B_{\|}/B_0$ for different β conditions. Dotted line represents the expected result for pressure balance which is qualitatively consistent and follows the correct trend for different β.

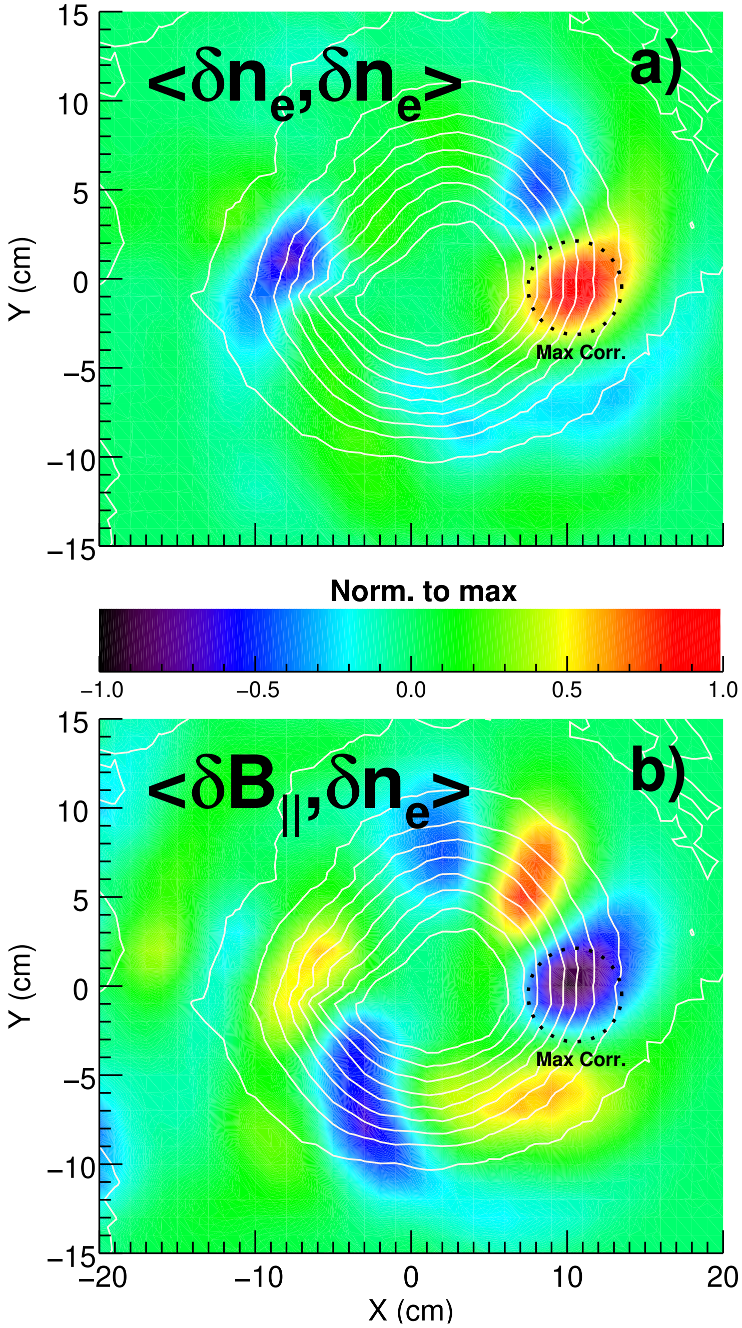

Figure 3.21: Strong anti-correlation at $\beta = 1.1\%$ of δn_e and $\delta B_\parallel$ fluctuations by showing a) cross correlation between a moving n_e and stationary n_e probe with b) correlation between a moving $B_\parallel$ and the same stationary n_e probe with the dotted circle indicating the location of maximum correlation from a). The contour lines map out the density profile.

From Fig. 3.22c) it is observed that for all low frequencies the cross-phase between n_e and $B_{\|}$ is π radians out of phase.

3.3.2 Polarization Analysis

Borrowing a technique frequently used in geophysics, one can use hodogram analysis to further classify the instability by decomposing the polarization of the instability to be either right-handed (rotating in the electron direction) or left-handed (rotating in the ion direction). A hodogram traditionally consists of a crossplot of two components of particle motion over a specific time window. For this dataset, simultaneous measurements of the perpendicular magnetic fluctuations, B_x and B_y, are made in the core of the plasma as the two components. The values of B_x and B_y are plotted on a crossplot at sequential time intervals such that one is able to observe the direction of the motion as time advances. This analysis also includes a frequency filter on the raw B_x/B_y time signals for $\omega < 0.1\omega_{ci}$ in order to allow the hodogram analysis to focus on displaying the polarization of the instability in question instead of extraneous high frequency noise.

Figures 3.23 and 3.24 show examples of this for both a high $\beta = 8.4\%$ and low $\beta = 0.39\%$ condition. The progression of time for the hodogram can be determined by looking at the advancement of color in trace. As the analysis progresses forward in time through the signal, so does the color progress in the pattern of a rainbow from red to purple. As seen in Figure 3.23, one can observe that the hodogram clearly moves in a clockwise-direction, while for Figure 3.24, it is in the opposite counter-clockwise direction.

While this difference in handedness is visually apparent for these low and high β, it becomes increasingly difficult to visually determine this difference for the intermediate β cases. Fortunately, Fourier analysis can be used to determine the polarization quantitatively and illuminate subtle trends that might exist as we vary β.

The analysis begins with first taking the Fourier transforms of $B_x(t)$ and $B_y(t)$ to be $\widetilde{B}_x(\omega)$ and

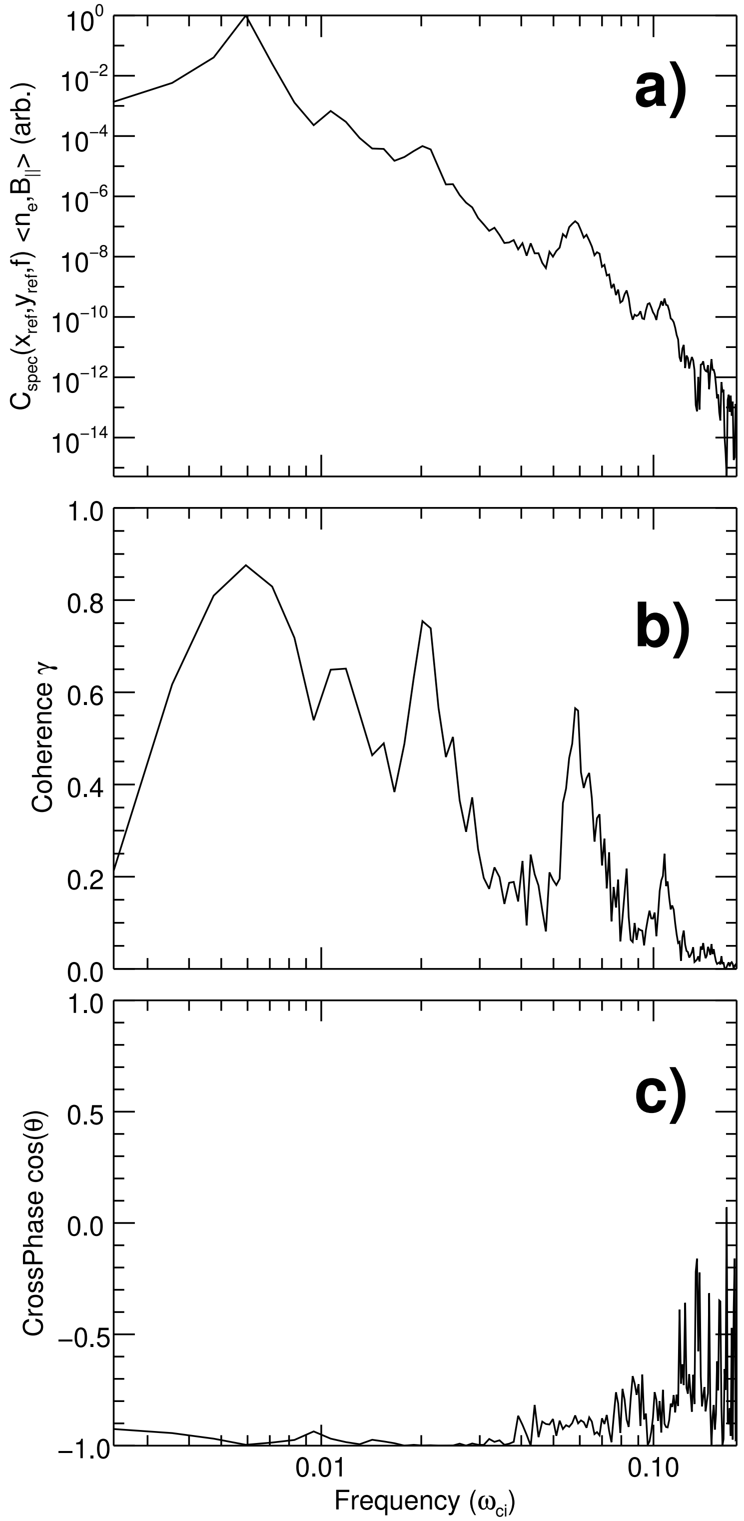

Figure 3.22: a) CrossPower ($C_{spec}(x_{\text{ref}}, y_{\text{ref}}, \omega)$), b) Cross-coherence ($\gamma$), and c) cross-phase ($\theta$) between δn_e and $\delta B_{\|}$ at $\beta = 1.1\%$. For all $\omega < .1\omega_{ci}$ the mode has a coherent $\frac{\pi}{2}$ phase difference.

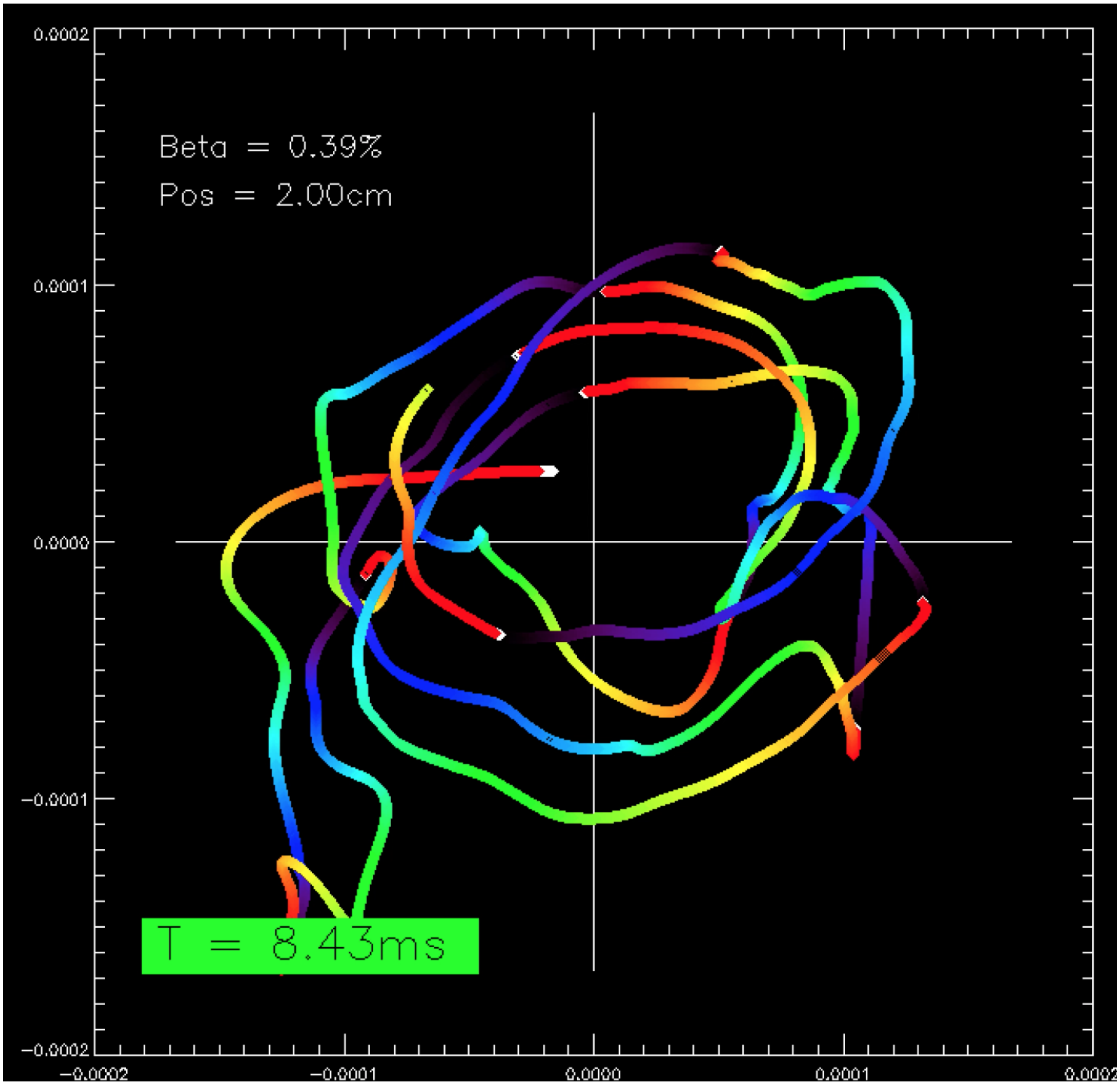

Figure 3.23: Hodogram of B_y/B_x at $\beta = 0.39\%$ showing clockwise progression Time advances for the plot by the same progression as the colors on a rainbow.

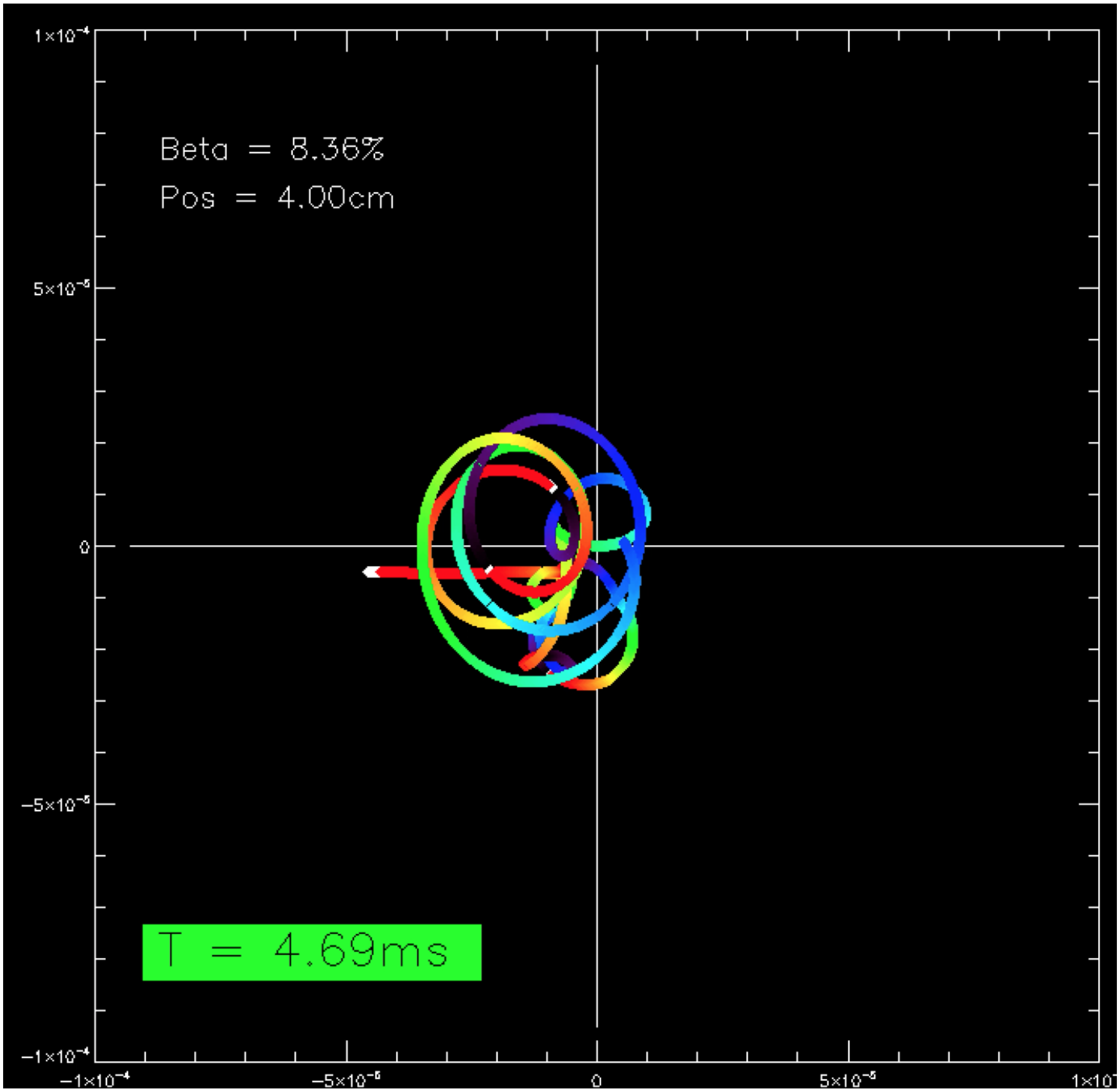

Figure 3.24: Hodogram of B_y/B_x at $\beta = 8.4\%$. Time advances for the plot by the same progression as the colors on a rainbow.

$\widetilde{B_y}(\omega)$ respectively.

$$\widetilde{B_x}(\omega) = \int_0^{t_f} B_x(t)e^{-i\omega t}dt \tag{3.9}$$

$$\widetilde{B_y}(\omega) = \int_0^{t_f} B_y(t)e^{-i\omega t}dt \tag{3.10}$$

These two components are then summed together in frequency space. This summation is performed with $B_y(t)$ being $+\frac{\pi}{2}$ out of phase with $B_x(t)$, corresponding to a right-handed polarization, or being $-\frac{\pi}{2}$ out of phase which corresponds to a left-handed polarization[56, 54].

$$\widetilde{B_L}(\omega) = \frac{1}{2}[\widetilde{B_x}(\omega) + i\widetilde{B_y}(\omega)] \tag{3.11}$$

$$\widetilde{B_R}(\omega) = \frac{1}{2}[\widetilde{B_x}(\omega) - i\widetilde{B_y}(\omega)] \tag{3.12}$$

Following this, $\widetilde{B_L}(\omega)$ and $\widetilde{B_R}(\omega)$ are transformed from frequency-space back to the time domain with the restriction of only transforming the positive frequencies.

$$B^\dagger{}_L(t) = \frac{1}{2\pi}\int_0^{\infty} \widetilde{B_L}(\omega)e^{i\omega t}d\omega \tag{3.13}$$

$$B^\dagger{}_R(t) = \frac{1}{2\pi}\int_0^{\infty} \widetilde{B_R}(\omega)e^{i\omega t}d\omega \tag{3.14}$$

The left-handed and right-handed summed time traces,$B^\dagger{}_L, B^\dagger{}_R$ are then subjected to another Fourier transform to get

$$\widetilde{B^\dagger{}_L}(\omega) = \int_0^{t_f} B^\dagger{}_L(t)e^{-i\omega t}dt \tag{3.15}$$

$$\widetilde{B^\dagger{}_R}(\omega) = \int_0^{t_f} B^\dagger{}_R(t)e^{-i\omega t}dt \tag{3.16}$$

From these one can analyze both power spectra $\left\|B^{\dagger}{}_{L}\right\|^{2}$ and $\left\|B^{\dagger}{}_{R}\right\|^{2}$. An example of these power spectra at different β can be seen in Figure 3.25. In order to determine quantitatively by what amount the instability is either left or right-hand dominant the percent power is defined by summing over frequencies ω as follows,

$$\% Left = \sum_{\omega} \frac{\left\|B^{\dagger}{}_{L}(\omega)\right\|^{2}}{\left\|B^{\dagger}{}_{L}(\omega)\right\|^{2} + \left\|B^{\dagger}{}_{R}(\omega)\right\|^{2}}. \tag{3.17}$$

$$\% Right = \sum_{\omega} \frac{\left\|B^{\dagger}{}_{R}(\omega)\right\|^{2}}{\left\|B^{\dagger}{}_{L}(\omega)\right\|^{2} + \left\|B^{\dagger}{}_{R}(\omega)\right\|^{2}}. \tag{3.18}$$

This analysis can be repeated for many different β conditions in order to illuminate any trends. Figure 3.26 shows this result when summing over all ω in Equations 3.17 and 3.18. From this figure it is concluded that the wave is predominantly left-handed for low β conditions. However, as β increases, there is a distinct shift where the turbulence changes to become more right-handed in nature. Since drift-Alfvén waves are typically left-hand polarized, this analysis further points to the turbulence being caused by a modified drift-Alfvén for the majority of β conditions studied in this experiment. The shift to right-hand polarized at the highest β conditions could indicate a new instability developing and explain the emergence of a single higher frequency coherent peak for $\beta > 8.4\%$ as seen in Fig. 3.17.

Digging deeper, when low frequency fluctuations ($\omega < .01\omega_{ci}$) are excluded from the hodogram analysis, a far more interesting trend appears with β. As seen in Figure 3.27, starting at the lowest β the same initial left-hand dominant behavior is present. However, as β increases up to $\beta \approx 2\%$, the instability changes to right-handed more rapidly than it did in Figure 3.26. The polarization then switches again to left-handed for $2\% < \beta < 6\%$ before returning to almost completely right-handed for $\beta > 6\%$.

An explanation for this sudden shift from left to right-handed polarization at $\beta \approx 2\%$ when low frequencies are excluded can be seen by looking at the spectra in Figure 3.25b). While left-handed power spectra is dominant for $\omega < .01\omega_{ci}$, a peak in right-handed power spectra around $\omega = 0.03\omega_{ci}$ dominates over the left-handed power spectra and is thus responsible for the percent power being

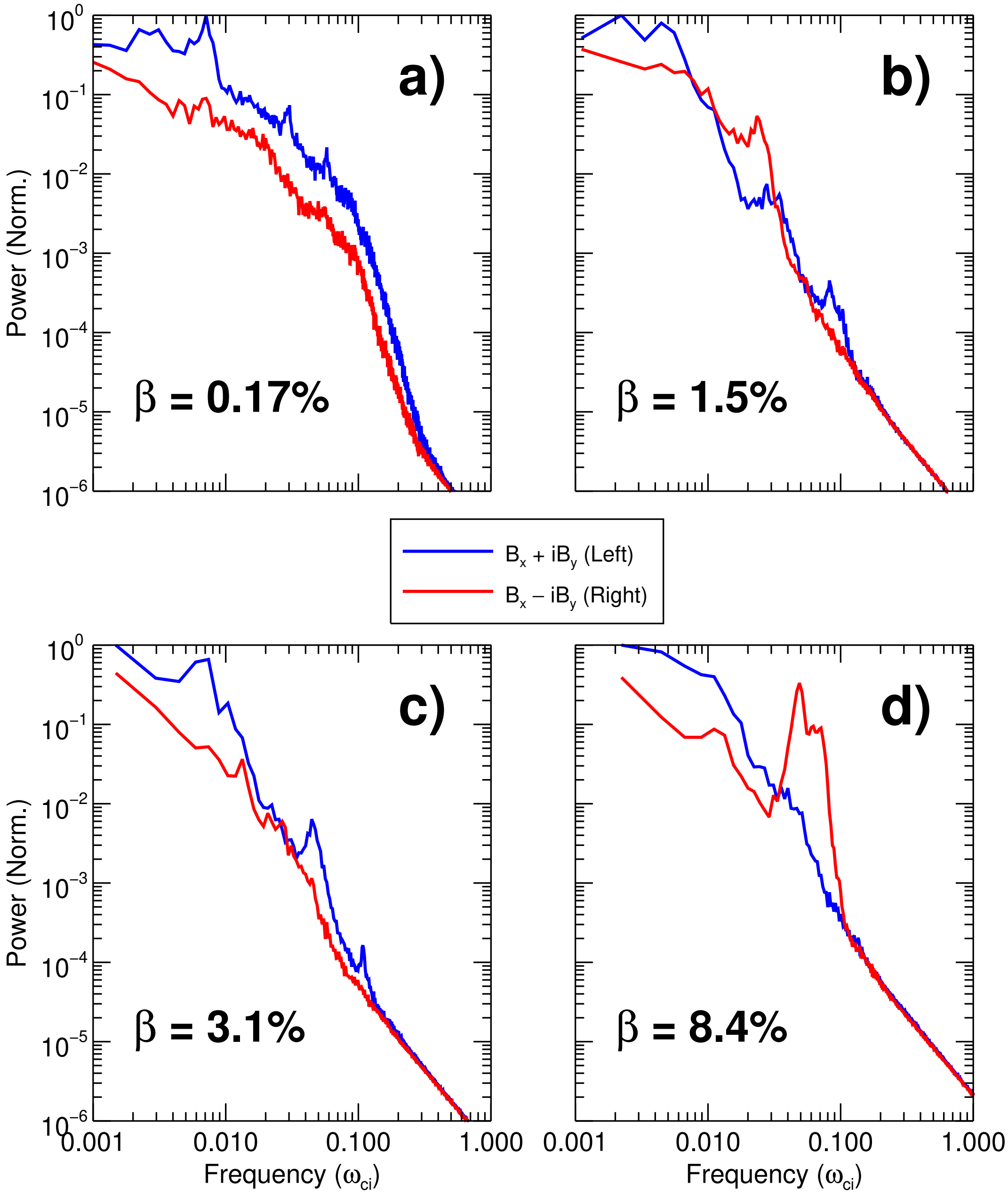

Figure 3.25: FFT of Left (Blue) and Right (Red) handed summations for determining polarization at a) $\beta = 0.17\%$, b) $\beta = 1.5\%$, c) $\beta = 3.1\%$, and d) $\beta = 8.4\%$.

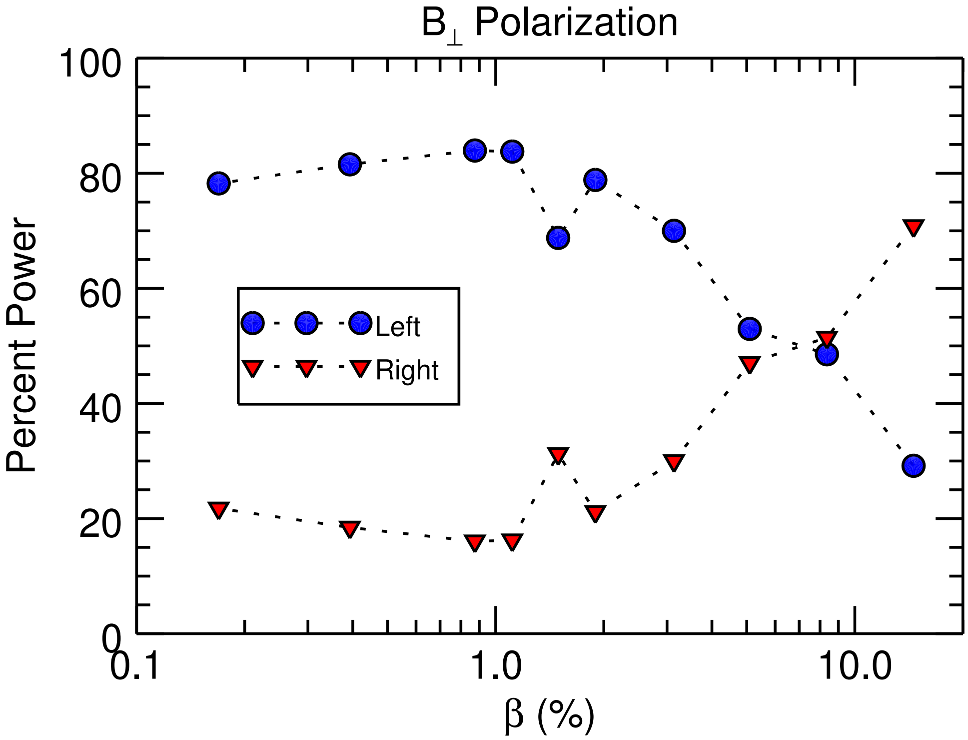

Figure 3.26: Power-weighted handedness of $\delta B_\perp$ fluctuations at various β conditions. Instability changes from left-handed to right-handed dominant with increasing β.

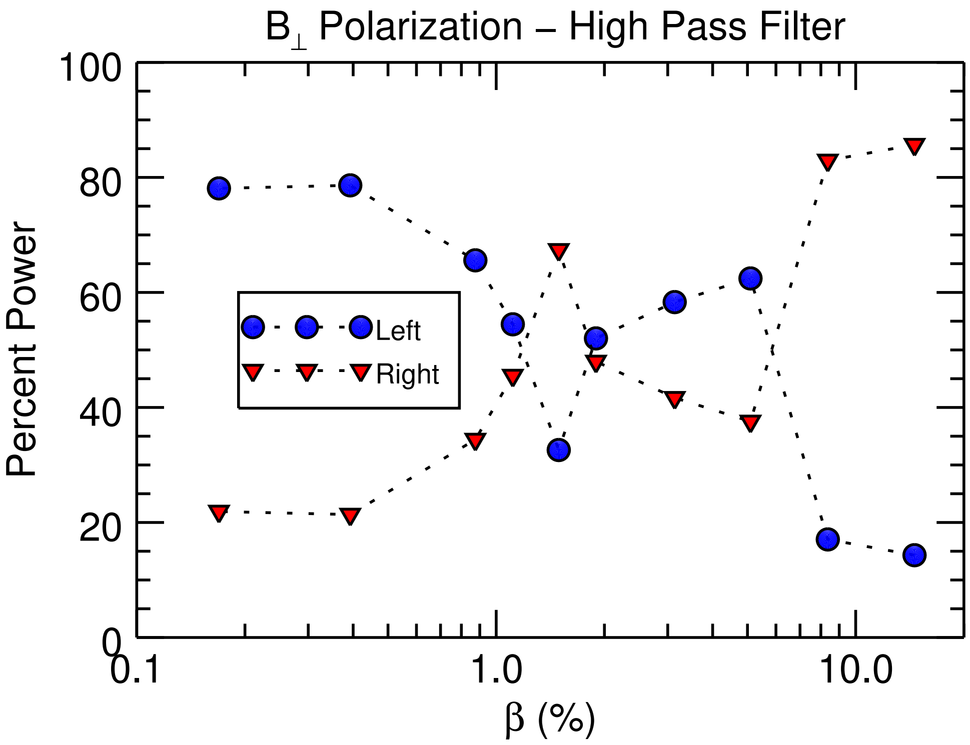

Figure 3.27: Power-weighted handedness of $\delta B_\perp$ fluctuations at various β conditions with a $\omega > .01\omega_{ci}$ high pass filter. Instability changes from left-handed to right-handed dominant with increasing β.

overall right-handed.

CHAPTER 4

Development of a Theoretical Model and Comparisons to Experiment

At lower β, the characteristics of the observed fluctuations are consistent with previous observations of low-m drift-Alfvén waves in LAPD. In particular, the mode pattern of correlated perpendicular magnetic and density fluctuations and the polarization of the perpendicular magnetic fluctuations are fully consistent. As β is increased, parallel magnetic fluctuations grow, correlated with the perpendicular magnetic and density fluctuations, an observation that is not consistent with the standard picture of the drift-Alfvén wave. This observation led to the proposal that the data could be the result of a new instability, the Gradient-driven Drift Coupling mode or GDC instability [43, 41, 40]. The GDC was originally observed in kinetic simulations of magnetic reconnection and had characteristics similar to those observed in the LAPD data, in particular correlated density and parallel magnetic field fluctuations with the magnetic field fluctuations out of phase with the density fluctuations. Kinetic simulations with LAPD pressure profiles and parameters indicated growth of the GDC in plasmas relevant to these experiments [58]. However, it was pointed out that the simulations that gave rise to the GDC as a new instability were run in out-of-equilibrium conditions, with pressure gradients but not including the gradients in the background magnetic field that should arise in pressure balance in finite β plasmas and are observed in this dataset. Exact force balance causes the GDC to become linearly marginally stable [46]. In addition, the GDC simulations do not predict correlated perpendicular magnetic fluctuations as observed in the experimental data. Recent simulations of the GDC in electron-positron plasmas indicate that the GDC can nonlinearly persist in plasmas where radial pressure balance exists (where gradients in the background field develop) [42] and as such this dissertation does not rule out the possibility that the GDC could play a role in the saturated turbulent state that was observed in the experiments. Nonetheless, given the similarity of the observed fluctuations in low β conditions to drift-Alfvén waves, the question naturally arises whether the observed modes are modified drift-Alfvén waves.

A local, slab-model linear theory has been developed, starting from a Hall-MHD derivation of drift-Alfvén waves outlined by Goldston [17]. Additional terms were added to include the experimental observations of significant fluctuations in the background magnetic field and including the non-uniform background field that arises due to diamagnetic effects at increased plasma β (see Section 3.2.1). The ordering of additional terms was determined by using experimental measurements of the amplitude of fluctuating quantities. The resulting linear model is detailed below.

4.1 A Simple Slab-Model Derivation

While there have been many derivations for drift waves in the electrostatic regime where β is negligible[5, 21, 23], the behavior of drift waves where electromagnetic effects are dominant is relatively unexplored. A simple dispersion relation can be derived for drift waves while keeping terms that are usually ignored when β is assumed to be small. Following Goldston's [17] analysis of drift waves, one can choose to use a slab model plasma with a non-uniform density $n(x)$ whereby equilibrium is maintained by a strong background magnetic field, B_0. The plasma is assumed to be at rest in the lab frame ($\mathbf{u} = 0$) but with a non-zero current density $J_y(x)$ which provides the $\mathbf{J} \times \mathbf{B}$ force to balance ∇P. A dispersion relation can be derived by first beginning with the perturbed equation of motion:

$$\begin{aligned} \rho_0 \partial_t \delta \mathbf{u} &= -\nabla \delta P + \delta(\mathbf{J} \times \mathbf{B}) \\ &= -\nabla \left(\delta P + \frac{\mathbf{B_0} \cdot \delta \mathbf{B}}{\mu_0} \right) + \frac{1}{\mu_0} \delta \left[(\mathbf{B} \cdot \nabla) \mathbf{B} \right]. \end{aligned} \tag{4.1}$$

If one assumes increased values of β such that the non-uniformity of $B(x)_0$ is significant and any perturbation quantity δN can be written as $\approx \delta N e^{(i\mathbf{k}\cdot\mathbf{r}-i\omega t)}$, the following components are obtained for Eq. 4.1:

$$
\begin{aligned}
-i\omega\rho_0\delta u_x &= -\partial_x\left(\delta P + \frac{B_0\cdot\delta B_\parallel}{\mu_0}\right) + \frac{ik_\parallel}{\mu_0}B_0\delta B_x \\
-i\omega\rho_0\delta u_y &= -ik_y\left(\delta P + \frac{B_0\cdot\delta B_\parallel}{\mu_0}\right) + \frac{ik_\parallel}{\mu_0}B_0\delta B_y \\
-i\omega\rho_0\delta u_\parallel &= -ik_\parallel\left(\delta P + \frac{B_0\cdot\delta B_\parallel}{\mu_0}\right) + \frac{ik_\parallel}{\mu_0}B_0\delta B_\parallel + \frac{\delta B_x}{\mu_0}\partial_x B_0
\end{aligned}
\tag{4.2}
$$

Assuming that any flow $\mathbf{u}$ that arises will be associated with an electric field $\mathbf{E}_\perp \approx \mathbf{u}\times\mathbf{B}$ that results in compression of $B_\parallel$ described by

$$
\begin{aligned}
\partial_t B_0 &\approx [\nabla\times(\mathbf{u}\times\mathbf{B})]_\parallel \\
-i\omega\delta B_\parallel &\approx -B_0\left(\partial_x\delta u_x + ik_y\delta u_y\right) - \delta u_x\partial_x B_0.
\end{aligned}
\tag{4.3}
$$

Now assume that $k_\parallel \ll k_y, k_x$ such that the divergence-free magnetic field condition is $\partial_x B_x + ik_y B_y = 0$, by combining Eq. 4.2 with δu_y from Eq. 4.3 one obtains

$$
\begin{aligned}
k_\perp^2\delta u_x = \frac{1}{B_0^2}\partial_x\delta u_x\partial_x B_0 + \frac{1}{B_0^2}\delta u_x\partial_x^2 B_\parallel - \frac{\delta u_x}{B_0^3}\left(\partial_x B_0\right)^2 \\
- \frac{k_\parallel\delta B_x}{\omega B_0}v_A^2\left(k_\perp^2 - \frac{k_x}{B_0}\partial_x B_0\right) + \omega k_x\frac{\delta B_\parallel}{B_0} + i\omega\frac{\delta B_\parallel}{B_0^2}\partial_x B_0
\end{aligned}
\tag{4.4}
$$

where $v_A^2 = \frac{B_0^2}{\mu_0\rho_0}$ is the Alfvén speed and $k_\perp^2 = k_x^2 + k_y^2$. In order to now link δu_x, δB_x, and $\delta B_\parallel$, one can combine Faraday's law ($\partial_t\delta B_\parallel = -\nabla\times\delta\mathbf{E}$) and Ampere's law ($\nabla\times\mathbf{B} = \mu_0\mathbf{J}$) with Ohm's law for first-order perturbed quantities ($\delta\mathbf{E} + \delta\mathbf{u}\times\mathbf{B} = \eta\delta\mathbf{J} + \frac{1}{ne}\delta[\mathbf{J}\times\mathbf{B} - \nabla P_e]$ where η is resistivity) to obtain

$$
\omega\delta B_x + k_\parallel B_0\delta u_x = -\frac{i\eta}{\mu_0}\delta B_x k_\perp^2 - \frac{k_y}{ne}\left(ik_\parallel\delta P_e + \frac{\delta B_x}{B_0}\partial_x P_e\right)
\tag{4.5}
$$

where it is assumed $\omega \ll \omega_{ci}$. If one also assumes that T_e is uniform along the field lines

($\mathbf{B} \cdot \nabla T_e = 0$) but can have a gradient across the field, then to first order one can write

$$ik_{\parallel}\delta T_e + \frac{\delta B_x}{B_0}\partial_x P_e = 0. \tag{4.6}$$

Now considering that the pressure profile to first order is $\delta P_e = n_e \delta T_e + T_e \delta n_e$ and combining with Eq. 4.6, one can manipulate the term in the bracket of Eq. 4.5 to become

$$ik_{\parallel}\delta P_e + \frac{B_x}{B_0}\partial_x P_e = T_e\left(ik_{\parallel}\delta n_e + \frac{\delta B_x}{B_0}\partial_x n_e\right). \tag{4.7}$$

From the continuity equation ($\partial_t n + \nabla \cdot n\mathbf{u} = 0$) it is assumed that the plasma behaves like an incompressible fluid in the perpendicular direction ($\nabla \cdot u_{\perp}$) to obtain an expression for $\delta u_{\parallel}$

$$ik_{\parallel} n_e \delta u_{\parallel} = i\omega \delta n_e - \delta u_x \frac{dn_e}{dx} \tag{4.8}$$

which can now be substituted into $\delta u_{\parallel}$ from Eq. 4.2 and with a significant amount of straightforward manipulation results in the following:

$$ik_{\parallel}\delta n_e + \frac{\delta B_x}{B_0}\partial_x n_e = \frac{\omega}{B_0}\partial_x n_e\left(\frac{\omega \delta B_x + k_{\parallel}\delta u_x B_0}{\omega^2 - c_s^2 k_{\parallel}^2}\right) + \frac{-k_{\parallel}^2 \delta B_x \partial_x B_0}{m\mu_0(\omega^2 - c_s^2 k_{\parallel}^2)} \tag{4.9}$$

where $c_s = \sqrt{\frac{T_e}{M}}$ is the plasma sound speed. Now substituting Eq. 4.9 into Eq. 4.5 results in

$$\left(\omega \delta B_x + k_{\parallel} B_0 \delta u_x\right)\left(1 - \frac{k_y \omega v_{de}}{\omega^2 - c_s^2 k_{\parallel}^2}\right) - \frac{k_y T_e}{n_e e}\frac{k_{\parallel}^2 \delta B_x \partial_x B_0}{m\mu_0(\omega^2 - c_s^2 k_{\parallel}^2)} = -i\eta \frac{\delta B_x k_{\perp}^2}{\mu_0} \tag{4.10}$$

where $v_{de} = \frac{T_e}{n_e e B_0}\partial_x n_e$. One must now determine an expression for δu_x by rearranging Eq. 4.4 to obtain:

$$\delta u_x = \frac{\omega k_x \left(\frac{\delta B_{\parallel}}{B_0}\right) + i\omega \frac{\delta B_{\parallel}}{B_0^2}\partial_x B_0 - \frac{k_{\parallel}\delta B_x}{\omega B_0} v_A^2 (k_{\perp}^2 - i\frac{k_x}{B_0}\partial_x B_0)}{k_{\perp}^2 - \frac{1}{B_0^2} i k_x \partial_x B_0 - \frac{1}{B_0^2}\partial_x^2 B_0 + \frac{1}{B_0^3}\left(\partial_x B_0\right)^2} \tag{4.11}$$

Which with pressure balance ($P+\frac{B_0^2}{2\mu_0} = \text{constant}$) and negligible temperature gradients ($\partial_x T_e = 0$) the first and second derivatives can be expanded as such that

$$\begin{aligned}
\partial_x P_e &= \frac{1}{2\mu_0}\partial_x B_0^2 \\
T_e \partial_x n_e &= \frac{B_0}{\mu_0}\partial_x B_0 \\
\partial_x B_0 &= \mu_0 n_e e \frac{T_e}{n_e e B_0}\partial_x n_e \\
&= -\frac{\mu_0 n_e e}{k_y}\omega^*
\end{aligned} \tag{4.12}$$

and

$$\begin{aligned}
T_e \partial_x^2 n_e &= \frac{1}{\mu_0}\partial_x(B_0 \partial_x B_0) \\
&= \frac{1}{\mu_0}(\partial_x B_0)^2 + \frac{B_0}{\mu_0}\partial_x^2 B_0 \\
&= \frac{1}{\mu_0}(\frac{\mu_0 n_e e}{k_y}\omega^*)^2 + \frac{B_0}{\mu_0}\partial_x^2 B_0 \\
&= (\frac{\sqrt{\mu_0} n_e e}{k_y}\omega^*)^2 + \frac{B_0}{\mu_0}\partial_x^2 B_0
\end{aligned} \tag{4.13}$$

such that

$$\partial_x^2 B_0 = \frac{\mu_0}{B_0} T_e \partial_x^2 n_e - \frac{\mu_0}{B_0}(\frac{\sqrt{\mu_0} n_e e}{k_y}\omega^*)^2 \tag{4.14}$$

where $\omega^* = k_y v_{de}$.

Eq. 4.11 can now be substituted into Eq. 4.10 and Eqs. 4.12, 4.13, 4.14 can be used to obtain the final dispersion relation

$$\underbrace{\left(\omega + \frac{k_\parallel \omega \frac{\delta B_\parallel}{\delta B_x}\left(k_x - i\frac{\mu_0 n_e e}{k_y}\omega^*\right) - \frac{k_\parallel^2}{\omega} v_A^2 \left(k_\perp^2 - ie\frac{B_0}{v_A^2}\frac{k_x}{k_y}\omega^*\right)}{k_\perp^2 + i\frac{e}{v_A^2}\frac{k_x}{k_y}\omega^* - \frac{\mu_0}{B_0^3} T_e \partial_x^2 n_e}\right)}_{\text{Shear Alfvén Wave (a)}} \times \underbrace{\left(1 - \frac{k_y \omega v_{de}}{\omega^2 - c_s^2 k_\parallel^2 chap:chapter5}\right)}_{\text{Drift Wave (b)}} = \underbrace{-\frac{c_s^2 k_\parallel^2 \omega^*}{\omega^2 - c_s^2 k_\parallel^2} - i\eta\frac{k_\perp^2}{\mu_0}}_{\text{Coupling Terms (c)}} \tag{4.15}$$

Eq. 4.15 is similar to the dispersion relation found in Goldston's original derivation (Eq. 4.16) with two distinct branches, one for the shear Alfvén wave (a) and one for the Drift wave (b).

$$\underbrace{\left(\omega - \frac{k_\parallel^2}{\omega} v_A^2\right)}_{\text{Shear Alfvén Wave (a)}} \times \underbrace{\left(1 - \frac{k_y \omega v_{de}}{\omega^2 - c_s^2 k_\parallel^2}\right)}_{\text{Drift Wave (b)}} = \underbrace{-i\eta \frac{k_\perp^2}{\mu_0}}_{\text{Coupling Term (c)}} \tag{4.16}$$

However, by assuming non-zero values of β we introduce a new secondary coupling term (c) as well as a new third term in the shear Alfvén wave (a) part of the dispersion relation.

The derivation of this dispersion relation is not yet complete as the fluctuating quantities $\delta B_\parallel$ and δB_x are also functions of ω and $k_\perp$. In order to determine this relationship one can start with the MHD equation of motion linearized to first order,

$$(\delta \mathbf{J} \times \mathbf{B}) + (\mathbf{J} \times \delta \mathbf{B}) - \nabla \delta P_e = \rho_0 \partial_t \delta \mathbf{u}. \tag{4.17}$$

If one assumes that the zeroth order $\mathbf{J}$ arises from the zeroth order diamagnetic drift $u_d \approx \nabla P \times \mathbf{B}$ and the pressure profile $P(x)$ only varies in the x direction and the zeroth order $\mathbf{B}$ is $B_\parallel$ which points in the z direction, this means $\mathbf{J}$ only points in the y direction. The $\hat{x}$ component of Eq. 4.17 can thus be written as:

$$\delta J_y B_0 - J_y \delta B_\parallel - \partial_x \delta P_e = -i\omega \rho_0 \delta u_x \tag{4.18}$$

Now using Ampere's law ($\nabla \times [\mathbf{B} + \delta \mathbf{B}] = \mu_0[\mathbf{J} + \delta \mathbf{J}]$) for both zeroth and first order one can obtain:

$$J_y = \frac{1}{\mu_0} \frac{d}{dx} B_\parallel \tag{4.19}$$

$$\delta J_y = \frac{1}{\mu_0}(ik_\parallel \delta B_x - ik_x \delta B_\parallel) \tag{4.20}$$

Both of these relations can now be substituted into Eq. 4.18 to result in

$$\frac{B_0}{\mu_0}(ik_{\parallel}\delta B_x - ik_x\delta B_{\parallel}) - \frac{\delta B_{\parallel}}{\mu_0}\partial_x B_0 - \nabla_x \delta P = -i\omega\rho_0\delta u_x \tag{4.21}$$

Now using the expression for δu_x from Eq. 4.11, one arrives at

$$\begin{split}\frac{B_0}{\mu_0}(ik_{\parallel}\delta B_x - ik_x\delta B_{\parallel}) - \frac{\delta B_{\parallel}}{\mu_0}\partial_x B_{\parallel} - \partial_x \delta P_e = \\ -i\omega\rho_0\left(\frac{\omega k_x\left(\frac{\delta B_{\parallel}}{B_0}\right) + i\omega\frac{\delta B_{\parallel}}{B_0^2}\partial_x B_0 - \frac{k_{\parallel}\delta B_x}{\omega B_0}v_A^2(k_{\perp}^2 - i\frac{k_x}{B_0}\partial_x B_0)}{k_{\perp}^2 - \frac{1}{B_0^2}ik_x\partial_x B_0 - \frac{1}{B_0^2}\partial_x^2 B_0 + \frac{1}{B_0^3}\left(\partial_x B_0\right)^2}\right)\end{split} \tag{4.22}$$

More work is needed on $\partial_x\delta P_e$ so beginning with the first order expansion one can arrive at

$$\begin{aligned}\partial_x\delta P_e &= \partial_x(n_e\delta T_e + \delta n_e T_e) \\ &= \delta T_e(\partial_x n_e + ik_x n_e) + \delta n_e(ik_x T_e + \partial_x T_e)\end{aligned} \tag{4.23}$$

which combined with Eqs. 4.6, 4.9, and 4.11 yields

$$\begin{split}\partial_x\delta P_e = \frac{i}{k_{\parallel}}\frac{\delta B_x}{B_0}\partial_x T_e\partial_x n_e - \frac{k_x}{k_{\parallel}}\frac{\delta B_x}{B_0}n_e\partial_x T_e \\ + \frac{\omega^2}{k_{\parallel}B_0(\omega^2 - c_s^2k_{\parallel}^2)}\partial_x n_e\left(k_x T_e + i\partial_x T_e\right)\delta B_x \\ + \frac{\omega}{(\omega^2 - c_s^2k_{\parallel}^2)}\partial_x n_e\left(k_x T_e + i\partial_x T_e\right)\left(\frac{\omega k_x\left(\frac{\delta B_{\parallel}}{B_0}\right) + i\omega\frac{\delta B_{\parallel}}{B_0^2}\partial_x B_0 - \frac{k_{\parallel}\delta B_x}{\omega B_0}v_A^2(k_{\perp}^2 - i\frac{k_x}{B_0}\partial_x B_0)}{k_{\perp}^2 - \frac{1}{B_0^2}ik_x\partial_x B_{\parallel} - \frac{1}{B_0^2}\partial_x^2 B_0 + \frac{1}{B_0^3}\left(\partial_x B_0\right)^2}\right) \\ - \frac{\omega k_{\parallel}}{(\omega^2 - c_s^2k_{\parallel}^2)}\frac{k_x T_e}{\omega m\mu_0}\delta B_x\partial_x B_0 - \frac{k_x T_e}{k_{\parallel}}\frac{\delta B_x}{B_0}\partial_x n_e + i\frac{\omega k_{\parallel}}{(\omega^2 - c_s^2k_{\parallel}^2)\omega m\mu_0}\delta B_x\partial_x T_e\partial_x B_0 \\ + i\frac{\partial_x T_e}{k_{\parallel}}\frac{\delta B_x}{B_0}\partial_x n_e\end{split} \tag{4.24}$$

Now taking Eq. 4.24 and plugging into Eq. 4.22 and grouping the δB_x and $\delta B_\parallel$ terms, one can arrive at the relation:

$$\frac{\delta B_\parallel}{\delta B_x} = \frac{\left(\begin{array}{c} \frac{ik_\parallel}{\mu_0}B_0 - \frac{i}{k_\parallel B_0}\partial_x T_e \partial_x n_e + \frac{k_x}{k_\parallel B_0} n_e \partial_x T_e \\ -\frac{\omega^2}{k_\parallel B_0(\omega^2 - c_s^2 k_\parallel^2)}\partial_x n_e \left(k_x T_e + i\partial_x T_e\right) \\ +\frac{\omega}{(\omega^2 - c_s^2 k_\parallel^2)}\partial_x n_e \left(k_x T_e + i\partial_x T_e\right)\left(\frac{\frac{k_\parallel}{\omega B_0} v_A^2 (k_\perp^2 - i\frac{k_x}{B_0}\partial_x B_0)}{k_\perp^2 - \frac{1}{B_0^2} ik_x \partial_x B_0 - \frac{1}{B_0^2}\partial_x^2 B_0 + \frac{1}{B_0^3}(\partial_x B_0)^2}\right) \\ +\frac{\omega k_\parallel}{(\omega^2 - c_s^2 k_\parallel^2)}\frac{k_x T_e}{\omega m \mu_0}\partial_x B_0 + \frac{k_x T_e}{k_\parallel B_0}\partial_x n_e - i\frac{\omega k_\parallel}{(\omega^2 - c_s^2 k_\parallel^2)\omega m \mu_0}\partial_x T_e \partial_x B_0 \\ -i\frac{\partial_x T_e}{k_\parallel B_0}\partial_x n_e - i\omega\rho_0\left(\frac{\frac{k_\parallel}{\omega B_0} v_A^2 (k_\perp^2 - i\frac{k_x}{B_0}\partial_x B_0)}{k_\perp^2 - \frac{1}{B_0^2} ik_x \partial_x B_0 - \frac{1}{B_0^2}\partial_x^2 B_0 + \frac{1}{B_0^3}(\partial_x B_0)^2}\right) \end{array}\right)}{\left(\begin{array}{c} \frac{ik_x}{\mu_0}B_0 + \frac{1}{\mu_0}\partial_x B_0 \\ +\frac{\omega}{(\omega^2 - c_s^2 k_\parallel^2)}\partial_x n_e \frac{(k_x T_e + i\partial_x T_e)}{\left(k_\perp^2 - \frac{1}{B_0^2} ik_x \partial_x B_0 - \frac{1}{B_0^2}\partial_x^2 B_0 + \frac{1}{B_0^3}(\partial_x B_0)^2\right)}\left(\frac{\omega k_x}{B_0} + \frac{i\omega}{B_0^2}\partial_x B_0\right) \\ -i\omega^2\rho_0\left(\frac{\left(\frac{k_x}{B_0}\right) + \frac{i}{B_0^2}\partial_x B_0}{k_\perp^2 - \frac{1}{B_0^2} ik_x \partial_x B_0 - \frac{1}{B_0^2}\partial_x^2 B_0 + \frac{1}{B_0^3}(\partial_x B_0)^2}\right) \end{array}\right)} \tag{4.25}$$

which can be substituted into Eq. 4.15 to obtain a final dispersion relation explicitly in terms of ω and k.

Using similar techniques from earlier in this Appendix, a relation between δn_e and $\delta B_\parallel$ can be derived by taking Eq. 4.22 and Eq. 4.6 to obtain:

$$\begin{aligned} &\frac{B_0}{\mu_0}(ik_\parallel \delta B_x - ik_x \delta B_\parallel) - \frac{\delta B_\parallel}{\mu_0}\partial_x B_0 \\ &\qquad - \left(\frac{i}{k_\parallel}\frac{\delta B_x}{B_0}\partial_x T_e(\partial_x n_e + ik_x n_e) + \delta n_e(ik_x T_e + \partial_x T_e)\right) \\ &\qquad = -i\omega\rho_0\left(\frac{\omega k_x\left(\frac{\delta B_\parallel}{B_0}\right) + i\omega\frac{\delta B_\parallel}{B_0^2}\partial_x B_0 - \frac{k_\parallel \delta B_x}{\omega B_0} v_A^2 (k_\perp^2 - i\frac{k_x}{B_0}\partial_x B_0)}{k_\perp^2 - \frac{1}{B_0^2} ik_x \partial_x B_0 - \frac{1}{B_0^2}\partial_x^2 B_0 + \frac{1}{B_0^3}(\partial_x B_0)^2}\right) \end{aligned} \tag{4.26}$$

Choosing to ignore the RHS and expand out terms to group the $\delta B_\parallel$ and δn_e terms one then arrives at

$$\delta B_{\parallel} = -\delta n_e \left(\frac{ik_x T_e + \partial_x T_e}{\frac{B_0}{\mu_0} ik_x + \frac{1}{\mu_0}\partial_x B_0} \right) - \frac{\frac{i}{k_{\parallel}} \frac{\delta B_x}{B_0} \partial_x T_e (\partial_x n_e + ik_x n_e) - \frac{B_0}{\mu_0} ik_{\parallel} \delta B_x}{\frac{B_0}{\mu_0} ik_x + \frac{1}{\mu_0}\partial_x B_0} \tag{4.27}$$

Since the ratio more important than the additive offset, one can ignore the second term on the RHS and rearrange such that

$$\delta B_{\parallel} = \frac{-\delta n_e \mu_0 T_e}{B_0} \times \frac{ik_x + \frac{1}{T_e}\partial_x T_e}{ik_x + \frac{1}{B_0}\partial_x B_0} \tag{4.28}$$

and multiplying by the complex conjugate will yield

$$\delta B_{\parallel} = \frac{-\delta n_e \mu_0 T_e}{B_0} \times \frac{-k_x^2 - \frac{1}{T_e B_0}\partial_x T_e \partial_x B_0 - ik_x \frac{1}{B_0}\partial_x B_0 + ik_x \frac{1}{T_e}\partial_x T_e}{-k_x^2 - \left(\frac{1}{B_0}\partial_x B_0\right)^2} \tag{4.29}$$

Using the algebraic expressions for the gradients:

$$\begin{aligned} \partial_x \log(B_0) &= \frac{1}{B_0}\partial_x B_0 \\ \partial_x \log(T_e) &= \frac{1}{T_e}\partial_x T_e \end{aligned} \tag{4.30}$$

and substituting into Eq. 4.29 yields

$$\delta B_{\parallel} = \frac{\delta n_e \mu_0 T_e}{B_0} \times \frac{-k_x^2 - \partial_x \log(B_0) \partial_x \log(T_e) - ik_x \partial_x \log(B_0) + ik_x \partial_x \log(T_e)}{k_x^2 + (\partial_x \log(B_0))^2} \tag{4.31}$$

which can now be rearranged to yield the normalized fluctuation amplitude ratio in terms of β

$$\frac{\delta B_{\parallel}/B_0}{\delta n_e/n_e} = \frac{\beta}{2} \times \frac{-k_x^2 - \partial_x \log(B_0) \partial_x \log(T_e) - ik_x \partial_x \log(B_0) + ik_x \partial_x \log(T_e)}{k_x^2 + (\partial_x \log(B_0))^2} \tag{4.32}$$

4.2 Comparing Theory and Experiment

Growth rates and instability characteristics of this model are computed using experimentally measured profiles for the lowest β condition and assuming $\lambda_{\parallel} = 2L_{\parallel}$ (where $L_{\parallel}$ is the axial length of the machine). First, roots of the dispersion relation from Eq. 4.15 are solved numerically using

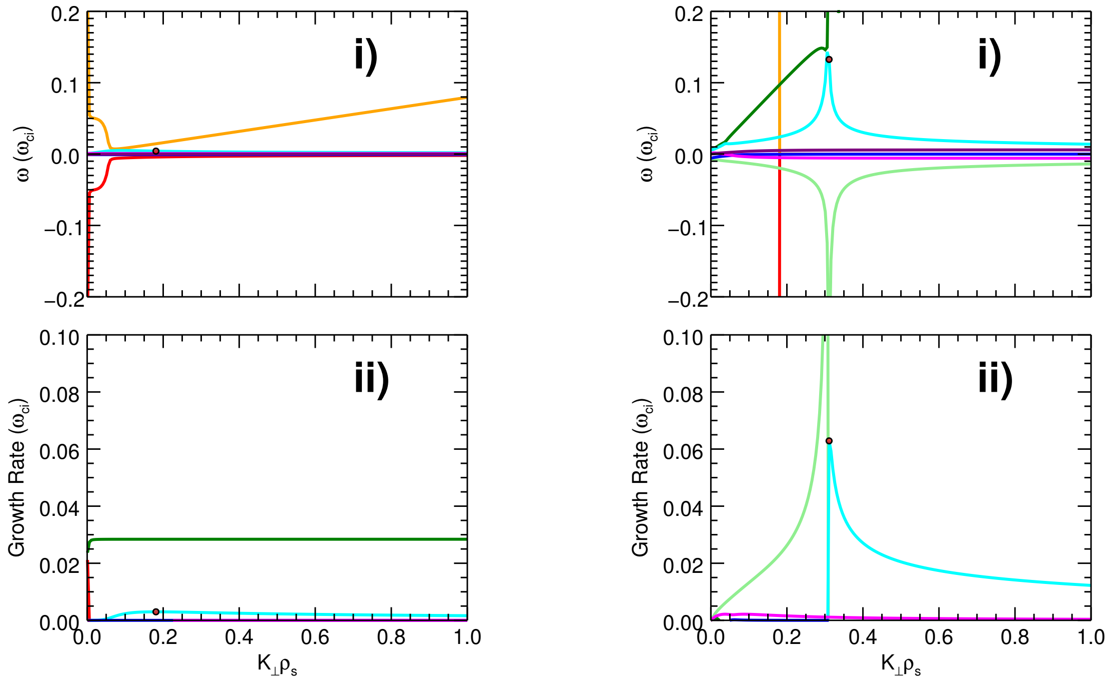

(a) $\beta = 0.17\%$

(b) $\beta = 8.4\%$

Figure 4.1: Real (i) and Imaginary (ii) components of ω for solutions to the modified dispersion relation Eq. 4.15 as a function of $k_\perp \rho_s$ at two different β. The red point marks the tracked fastest growing mode. Colors help identify the corresponding real and imaginary components for different solutions.

Mathematica in terms of $k_\perp$ and ω. This process is then repeated by then decreasing B_0 to perform a scan in plasma β. Third, special care is taken to track the fastest growing mode that persists continuously throughout the β scan while ignoring extraneous solutions. For each β, the peak growth rate (imaginary component of ω), real frequency (real component of ω), and normalized wavenumber ($k_\perp \rho_s$) are recorded. An example of this process for two different β can be seen in Figure 4.1a and 4.1b.

One can now plot the growth rate for the fastest growing mode as shown in Figure 4.2. Here it is seen that for all values of β there appears to be an unstable mode and the growth rate increases with β.

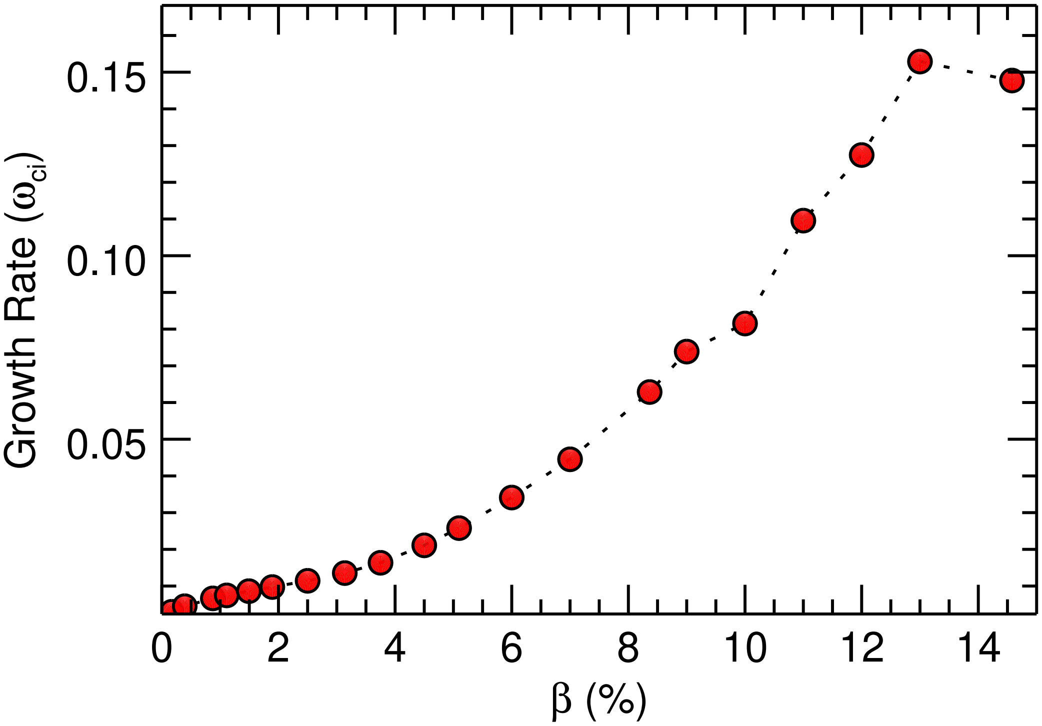

Figure 4.2: Growth rate of fastest growing mode from local theory at various β conditions.

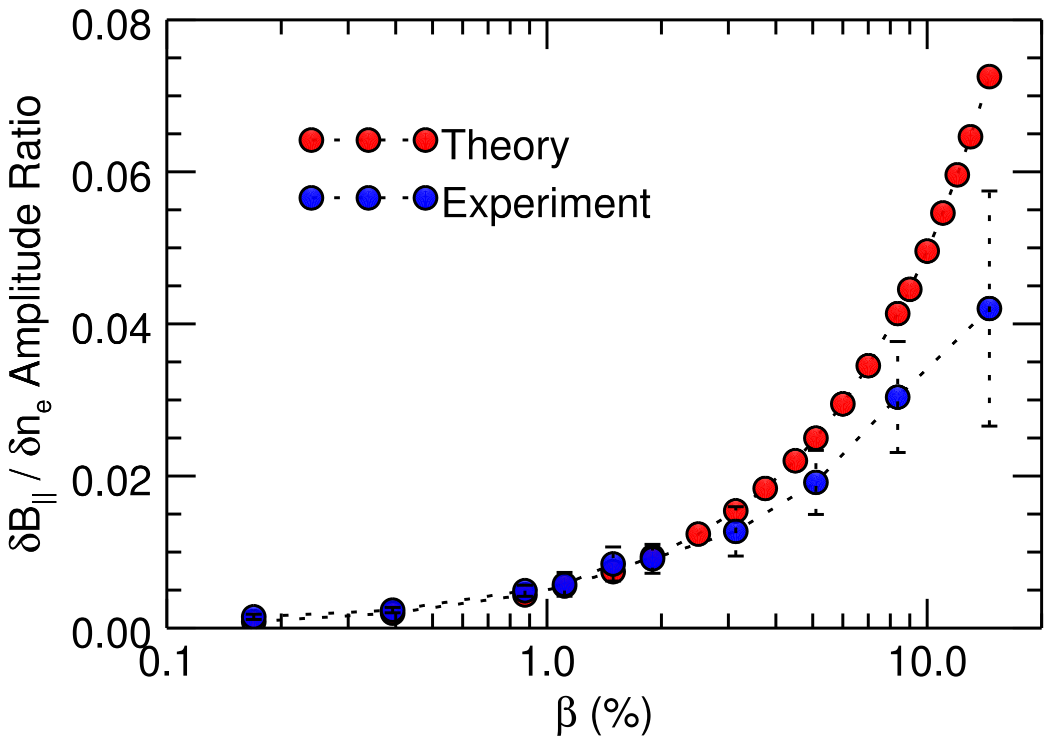

Figure 4.3: Ratio of parallel magnetic to density fluctuation amplitude as a function of β

In addition, this local theory can be used to compute ratios of amplitudes and phase differences for various fluctuating quantities in order to compare to experimental results. As detailed in Eq. 4.32, the amplitude ratio between $\delta B_{||}$ and δn can be be derived as follows:

$$\frac{\delta B_z/B_0}{\delta n_e/n_e} = \frac{\beta}{2} \times \frac{-k_x^2 - \partial_x \log(B_0)\partial_x \log(T_e) - ik_x\partial_x \log(B_0) + ik_x\partial_x \log(T_e)}{k_x^2 + (\partial_x \log(B_0))^2} \tag{4.33}$$

Figure 4.3 shows this ratio computed, using experimentally measured profiles and the ω and $k_\perp$ of the fastest growing mode for each β, along with experimental measurements. There is relatively good agreement between the linear theory prediction and experimental measurement for $\beta < 2\%$ with deviations at the higher β. As shown in Eq. 4.25, the ratio between $\delta B_{||}$ and $\delta B_\perp$ can also be computed from the model:

$$\frac{\delta B_{\|}}{\delta B_x}=\frac{\left(\begin{array}{c}\frac{ik_{\|}}{\mu_0}B_0-\frac{i}{k_{\|}B_0}\partial_xT_e\partial_xn_e+\frac{k_x}{k_{\|}B_0}n_e\partial_xT_e\\ -\frac{\omega^2}{k_{\|}B_0(\omega^2-c_s^2k_{\|}^2)}\partial_xn_e\left(k_xT_e+i\partial_xT_e\right)\\ +\frac{\omega}{(\omega^2-c_s^2k_{\|}^2)}\partial_xn_e\left(k_xT_e+i\partial_xT_e\right)\left(\frac{\frac{k_{\|}}{\omega B_0}v_A^2(k_\perp^2-i\frac{k_x}{B_0}\partial_xB_0)}{k_\perp^2-\frac{1}{B_0^2}ik_x\partial_xB_0-\frac{1}{B_0^2}\partial_x^2B_0+\frac{1}{B_0^3}(\partial_xB_0)^2}\right)\\ +\frac{\omega k_{\|}}{(\omega^2-c_s^2k_{\|}^2)}\frac{k_xT_e}{\omega m\mu_0}\partial_xB_0+\frac{k_xT_e}{k_{\|}B_0}\partial_xn_e-i\frac{\omega k_{\|}}{(\omega^2-c_s^2k_{\|}^2)\omega m\mu_0}\partial_xT_e\partial_xB_0\\ -i\frac{\partial_xT_e}{k_{\|}B_0}\partial_xn_e-i\omega\rho_0\left(\frac{\frac{k_{\|}}{\omega B_0}v_A^2(k_\perp^2-i\frac{k_x}{B_0}\partial_xB_0)}{k_\perp^2-\frac{1}{B_0^2}ik_x\partial_xB_0-\frac{1}{B_0^2}\partial_x^2B_0+\frac{1}{B_0^3}(\partial_xB_0)^2}\right)\end{array}\right)}{\left(\begin{array}{c}\frac{ik_x}{\mu_0}B_0+\frac{1}{\mu_0}\partial_xB_0\\ +\frac{\omega}{(\omega^2-c_s^2k_{\|}^2)}\partial_xn_e\frac{(k_xT_e+i\partial_xT_e)}{\left(k_\perp^2-\frac{1}{B_0^2}ik_x\partial_xB_0-\frac{1}{B_0^2}\partial_x^2B_0+\frac{1}{B_0^3}(\partial_xB_0)^2\right)}\left(\frac{\omega k_x}{B_0}+\frac{i\omega}{B_0^2}\partial_xB_0\right)\\ -i\omega^2\rho_0\left(\frac{\left(\frac{k_x}{B_0}\right)+\frac{i}{B_0^2}\partial_xB_0}{k_\perp^2-\frac{1}{B_0^2}ik_x\partial_xB_0-\frac{1}{B_0^2}\partial_x^2B_0+\frac{1}{B_0^3}(\partial_xB_0)^2}\right)\end{array}\right)} \tag{4.34}$$

By performing a comparison of the theoretical predictions to experimental results as seen in Fig. 4.4, the ratio of these fluctuations increase with β in a similar fashion to the experimental results for $\beta < 2\%$. While the parallel wavelength of the mode was not able to be measured directly, the theoretical predictions suggest that $\lambda_{||}$ is many machine lengths as seen with the improved agreement for larger $\lambda_{||}$

While the experimental data is consistent with the predictions of the slab-based local model at lower β, that agreement begins to break down at higher $\beta > 2\%$. This could be explained by finite Larmor radius (FLR) effects becoming important as lowering the background magnetic field to increase β also increases the ion gyroradius such that only a few ion gyroradii fit within the pressure gradients of the experiment. Future work will seek to address this through the development of a global kinetic model that includes significant $\delta B_{||}$ fluctuations in order to capture more of the physics involved with the predominantly low-m modes observed.

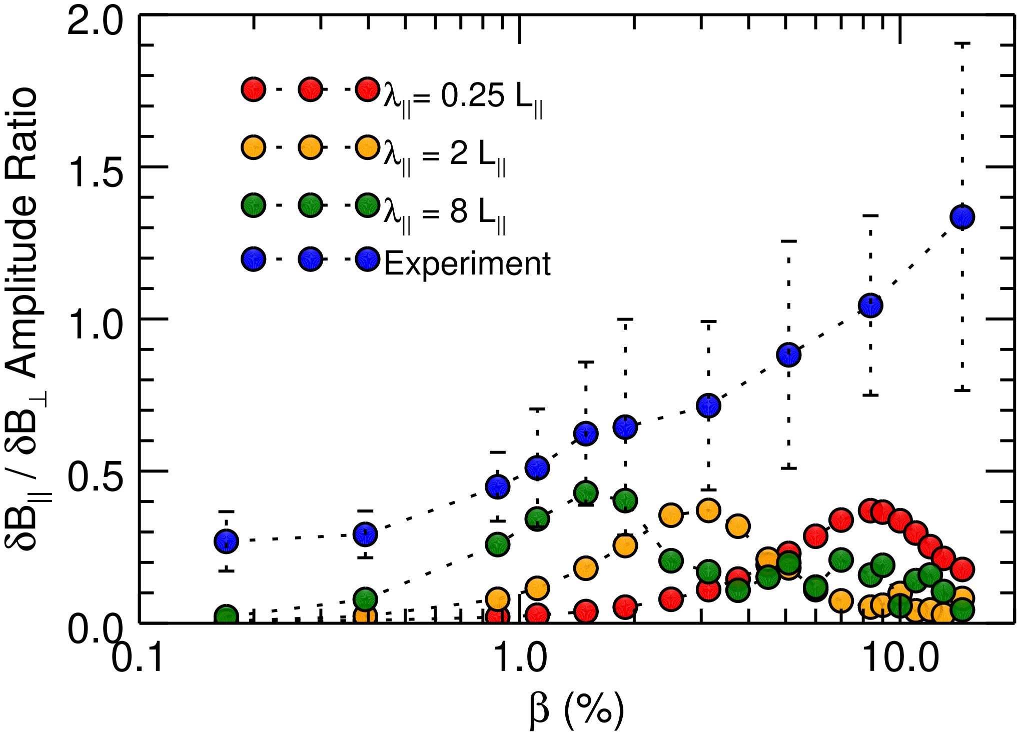

Figure 4.4: Ratio of parallel to perpendicular magnetic fluctuation amplitude for experimental data and using a theoretical model with different values of $\lambda_{||}$ where $L_{||}$ is the axial length of the machine. Ratio is seen to generally increase with increasing β with the best agreement between theory and experiment at higher $\lambda_{||}$

CHAPTER 5

Conclusions

This experiment sought to document the variation of pressure-gradient-driven turbulence and transport for a linear, magnetized plasma as β was increased. By utilizing a new LaB$_6$ source to increase plasma pressure in conjunction with lowering the background magnetic field to decrease magnetic pressure, β of up to $\approx 15\%$ was attained for the first time in LAPD. Taking advantage of the high-repetition rate and computer-controlled diagnostics on LAPD, a volumetric dataset was collected over the course of three experimental campaigns that each lasted two weeks.

Analyzing this data, it was observed that magnetic fluctuations grew substantially with increasing β. Specifically, that the parallel magnetic fluctuations were dominant at higher β, increasing up to $\delta B_{\|}/\delta B_{\perp} \approx 2$ with $\delta B/B_0 \approx 1\%$. Investigating this novel result further, it was shown that the parallel magnetic fluctuations were also strongly correlated with density fluctuations and out of phase with one another. 2D cross-correlation analysis between $\delta B_{\|}, \delta B_{\perp}$, and δn_e revealed a coherent measured mode pattern that was consistent with previous observations of drift-Alfvén waves with supporting evidence from polarization measurements. Comparisons were also made of fluctuation amplitude ratios between δn_e and $\delta B_{\|}$ and showed consistency with dynamic pressure balance ($P + \frac{B_0^2}{2\mu_0} = \text{constant}$).

In order to explain the experimental results of this data, a few approaches were taken to connect to theory. The first involved collaboration with an outside group that proposed the significant $\delta B_{\|}$ observed were indicative of a newly theorized instability called the GDC[40]. However, GDC did not include $\delta B_{\perp}$ which were significant and highly correlated to $\delta B_{\|}$ in the experiment. Furthermore, the zeroth order pressure balance observed within the experiment was later argued as incompatible with the GDC[46]. This being the case, a second approach was made to connect to theory by proposing the experimental results be compared to an electromagnetic, modified drift Alfvén wave. This motivated the development of a local slab-model theory for drift Alfvén waves that included the experimental observations of significant parallel magnetic fluctuations and diamagnetic corrections to the background field.

Numerical solutions to the the dispersion relation derived from this theoretical model revealed growing modes that increased in growth rate with β. Further comparisons of the turbulent fluctuation amplitudes between the theoretical model and experimental data showed promising agreement for $\beta < 2\%$ while disagreements at higher β showed limitations of the code for including all physical mechanisms such as finite Larmor radius (FLR) effects.

While this experiment aspired to be exploratory and document a wide range of phenomena related to increasing β in LAPD, there are still many more areas that can be examined. Firstly, the resolution and range of β scanned could be improved for $\beta > 2\%$. The resolution increase could be achieved by simply choosing more background magnetic fields to scan, while increasing the range of β would require some engineering advancements in the experimental device. As seen in this experiment, there are limits in trying to lower the background magnetic field further as FLR effects are most likely to become even more significant. However, during the writing of this dissertation there have been many upgrades made to LAPD, one of which is replacing the BaO source with a much larger LaB_6 source. This source should allow for even greater plasma pressure while also providing a wider plasma column such that many gyroradii can fit within the plasma and thus reduce the FLR limitations. It is worthy to note however that with increased plasma pressure from hotter sources comes the greater risks to damaging diagnostics. During the course of these experimental campaigns, there were many instances of probe failure due to prolonged exposure to high temperatures which caused delays and in some cases halted data collection. The development of more robust magnetic and Langmuir probes would thus also be necessary to effectively document the higher β cases.

Additional diagnostics should also be utilized in order to characterize the plasma at increased β. While not a focus of this experiment, previous studies have shown there to be spontaneous azimuthal flows within LAPD[48]. Rudimentary measurements of this flow at different β were made with triple Langmuir probes calibrated to swept measurements, but the accuracy of these results seemed questionable. A more focused campaign using emissive probes in conjunction with Mach probes would be beneficial for definitively determining the effect of β on flow as well as improving confidence in the plasma potential profiles.

Another area of investigation that could be improved would be in documenting variations to the 2D structure of the turbulence with additional cross-correlation datasets. The volumetric size of these datasets that require ≈ 20 hours each to collect meant that only a few β were able to analyzed in this dissertation. It should also be noted that significant variation in the radial location of peak $\delta B_{||}$ due to the flaring of B_0 can make it difficult to target the exact area of data collection. Thus, the development of a single reference probe with multiple magnetic and Langmuir tips at different radial locations would greatly reduce the trial and error of data collection and time spent to collect cross-correlation data. A single moving probe with simultaneous measurements of $\delta n_e, \delta v_f$, and δB would also reduce runtime by an additional 50%.

While the instability analysis using the model developed in this dissertation had reasonable agreement to experimental values for $\beta < 2\%$, the differences at higher β prompts the need for future theoretical work. Specifically, the development of a global kinetic model, with thorough analysis in regards to the ordering of terms, would be extremely helpful to illuminate whether the differences seen at $\beta > 2\%$ are the result of a new instability or just further modifications to a drift-Alfvén wave.

BIBLIOGRAPHY

[1] Steven A Balbus. Enhanced angular momentum transport in accretion disks. Annual Review of Astronomy and Astrophysics, 41(1):555–597, 2003.

[2] AT Burke, JE Maggs, and GJ Morales. Experimental study of fluctuations excited by a narrow temperature filament in a magnetized plasma. Physics of Plasmas, 7(5):1397–1407, 2000.

[3] J. Candy. Beta scaling of transport in microturbulence simulations. Physics of Plasmas, 12(7):072307, 2005.

[4] B. A. Carreras. Progress in anomalous transport research in toroidal magnetic confinement devices. IEEE Transactions on Plasma Science, 25(6):1281–1321, Dec 1997.

[5] Francis F Chen et al. Introduction to plasma physics and controlled fusion, volume 1. Springer, 1984.

[6] Sin-Li Chen and T. Sekiguchi. Instantaneous direct-display system of plasma parameters by means of triple probe. Journal of Applied Physics, 36(8):2363–2375, 1965.

[7] J Citrin, J Garcia, T Görler, F Jenko, P Mantica, D Told, C Bourdelle, D R Hatch, G M D Hogeweij, T Johnson, M J Pueschel, and M Schneider. Electromagnetic stabilization of tokamak microturbulence in a high- β regime. Plasma Physics and Controlled Fusion, 57(1):014032, 2015.

[8] CM Cooper, W Gekelman, P Pribyl, and Z Lucky. A new large area lanthanum hexaboride plasma source. Review of Scientific Instruments, 81(8):083503, 2010.

[9] E.J. Doyle. Chapter 2: Plasma confinement and transport. Nuclear Fusion, 47(6):S18, 2007.

[10] E. T. Everson, P. Pribyl, C. G. Constantin, A. Zylstra, D. Schaeffer, N. L. Kugland, and C. Niemann. Design, construction, and calibration of a three-axis, high-frequency magnetic probe (b-dot probe) as a diagnostic for exploding plasmas. Review of Scientific Instruments, 80(11):113505, 2009.

[11] JP Freidberg and JA Wesson. Minimum required beta in a tokamak reactor. Nuclear fusion, 25(7):759, 1985.

[12] B. Friedman, T. A. Carter, M. V. Umansky, D. Schaffner, and B. Dudson. Energy dynamics in a simulation of lapd turbulence. Physics of Plasmas, 19(10):102307, 2012.

[13] G Allen Gary. Plasma beta above a solar active region: Rethinking the paradigm. Solar Physics, 203(1):71–86, 2001.

[14] W Gekelman, H Pfister, Z Lucky, J Bamber, D Leneman, and J Maggs. Design, construction, and properties of the large plasma research device- the lapd at ucla. Review of scientific instruments, 62(12):2875–2883, 1991.

[15] W Gekelman, P Pribyl, Z Lucky, M Drandell, D Leneman, J Maggs, S Vincena, B Van Compernolle, SKP Tripathi, G Morales, et al. The upgraded large plasma device, a machine for studying frontier basic plasma physics. Review of Scientific Instruments, 87(2):025105, 2016.

[16] Walter Gekelman, S Vincena, B Van Compernolle, GJ Morales, JE Maggs, P Pribyl, and TA Carter. The many faces of shear alfvén waves. Physics of Plasmas, 18(5):055501, 2011.

[17] Robert J Goldston and Paul Harding Rutherford. Introduction to plasma physics. CRC Press, 1995.

[18] M Gryaznevich, R Akers, PG Carolan, NJ Conway, D Gates, AR Field, TC Hender, I Jenkins, R Martin, MPS Nightingale, et al. Achievement of record β in the start spherical tokamak. Physical review letters, 80(18):3972, 1998.

[19] Scott W Haney and Jeffrey P Freidberg. Desirability of approaches to achieving high beta. Nuclear fusion, 27(11):1827, 1987.

[20] C Hidalgo. Edge turbulence and anomalous transport in fusion plasmas. Plasma Physics and Controlled Fusion, 37(11A):A53, 1995.

[21] W Horton. Drift waves and transport. Reviews of Modern Physics, 71(3):735, 1999.

[22] W. Horton, Jean C. Perez, Troy Carter, and Roger Bengtson. Vorticity probes and the characterization of vortices in the kelvin–helmholtz instability in the large plasma device experiment. Physics of Plasmas, 12(2):022303, 2005.

[23] Wendell Horton. Nonlinear drift waves and transport in magnetized plasma. Physics Reports, 192(1-3):1–177, 1990.

[24] D. L. Jassby. Transverse velocity shear instabilities within a magnetically confined plasma. The Physics of Fluids, 15(9):1590–1604, 1972.

[25] Frank Jenko and Bruce D. Scott. Numerical computation of collisionless drift alfvén turbulence. Physics of Plasmas, 6(7):2705–2713, 1999.

[26] M Kikuchi. Prospects of a stationary tokamak reactor. Plasma Physics and Controlled Fusion, 35(SB):B39, 1993.

[27] Wonjae Lee, J.R. Angus, Maxim V. Umansky, and Sergei I. Krasheninnikov. Electromagnetic effects on plasma blob-filament transport. Journal of Nuclear Materials, 463:765 – 768, 2015.

[28] Paulett C. Liewer. Measurements of microturbulence in tokamaks and comparisons with theories of turbulence and anomalous transport. Nuclear Fusion, 25(5):543, 1985.

[29] W Mandl, RC Wolf, MG Von Hellermann, and HP Summers. Beam emission spectroscopy as a comprehensive plasma diagnostic tool. Plasma physics and controlled fusion, 35(10):1373, 1993.

[30] ME Mauel. The use of scaling laws for the design of high beta tokamaks. Nuclear fusion, 27(2):313, 1987.

[31] G J Morales, J E Maggs, A T Burke, and J R Peñano. Alfvénic turbulence associated with density and temperature filaments. Plasma Physics and Controlled Fusion, 41(3A):A519–A529, jan 1999.

[32] J. R. Myra, D. A. Russell, and D. A. D'Ippolito. Transport of perpendicular edge momentum by drift-interchange turbulence and blobs. Physics of Plasmas, 15(3):032304, 2008.

[33] D. C. Pace, M. Shi, J. E. Maggs, G. J. Morales, and T. A. Carter. Exponential frequency spectrum in magnetized plasmas. Phys. Rev. Lett., 101:085001, Aug 2008.

[34] J. R. Peñano, G. J. Morales, and J. E. Maggs. Drift-alfvÃ©n fluctuations associated with a narrow pressure striation. Physics of Plasmas, 7(1):144–157, 2000.

[35] MA Pedrosa, A López-Sánchez, C Hidalgo, A Montoro, A Gabriel, J Encabo, J De La Gama, LM Martınez, E Sánchez, R Pérez, et al. Fast movable remotely controlled langmuir probe system. Review of scientific instruments, 70(1):415–418, 1999.

[36] P Pribyl and W Gekelman. 24 ka solid state switch for plasma discharge experiments. Review of scientific instruments, 75(3):669–673, 2004.

[37] M. J. Pueschel, D. R. Hatch, T. Görler, W. M. Nevins, F. Jenko, P. W. Terry, and D. Told. Properties of high-β microturbulence and the non-zonal transition. Physics of Plasmas, 20(10):102301, 2013.

[38] M. J. Pueschel and F. Jenko. Transport properties of finite-β microturbulence. Physics of Plasmas, 17(6):062307, 2010.

[39] M. J. Pueschel, M. Kammerer, and F. Jenko. Gyrokinetic turbulence simulations at high plasma beta. Physics of Plasmas, 15(10):102310, 2008.

[40] M J Pueschel, G Rossi, D Told, P W Terry, F Jenko, and T A Carter. A basic plasma test for gyrokinetics: GDC turbulence in LAPD. Plasma Physics and Controlled Fusion, 59(2):024006, jan 2017.

[41] M. J. Pueschel, P. W. Terry, D. Told, and F. Jenko. Enhanced magnetic reconnection in the presence of pressure gradients. Physics of Plasmas, 22(6):062105, 2015.

[42] MJ Pueschel, RD Sydora, PW Terry, B Tyburska-Pueschel, M Francisquez, F Jenko, and B Zhu. Pair plasma instability in homogeneous magnetic guide fields. Physics of Plasmas, 27(10):102111, 2020.

[43] Moritz J Pueschel, F Jenko, D Told, and J Büchner. Gyrokinetic simulations of magnetic reconnection. Physics of Plasmas, 18(11):112102, 2011.

[44] Eliot Quataert, William Dorland, and Gregory W Hammett. The magnetorotational instability in a collisionless plasma. The Astrophysical Journal, 577(1):524, 2002.

[45] A. B. Rechester and M. N. Rosenbluth. Electron heat transport in a tokamak with destroyed magnetic surfaces. Phys. Rev. Lett., 40:38–41, Jan 1978.

[46] Barrett N. Rogers, Ben Zhu, and Manaure Francisquez. Gyrokinetic theory of slab universal modes and the non-existence of the gradient drift coupling (gdc) instability. Physics of Plasmas, 25(5):052115, 2018.

[47] S Sakakibara, KY Watanabe, Y Takemura, M Okamoto, S Ohdachi, Y Suzuki, Y Narushima, K Ida, M Yoshinuma, K Tanaka, et al. Characteristics of mhd instabilities limiting the beta value in lhd. Nuclear Fusion, 55(8):083020, 2015.

[48] D. A. Schaffner, T. A. Carter, G. D. Rossi, D. S. Guice, J. E. Maggs, S. Vincena, and B. Friedman. Turbulence and transport suppression scaling with flow shear on the large plasma device. Physics of Plasmas, 20(5):055907, 2013.

[49] A. Smolyakov, P. Diamond, and Y. Kishimoto. Secondary instabilities of large scale flow and magnetic field in the electromagnetic short wavelength drift-alfvén wave turbulence. Physics of Plasmas, 9(9):3826–3834, 2002.

[50] P. B. Snyder and G. W. Hammett. Electromagnetic effects on plasma microturbulence and transport. Physics of Plasmas, 8(3):744–749, 2001.

[51] EJ Strait. Stability of high beta tokamak plasmas. Physics of Plasmas, 1(5):1415–1431, 1994.

[52] Ulrich Stroth. A comparative study of transport in stellarators and tokamaks. Plasma Physics and Controlled Fusion, 40(1):9–74, jan 1998.

[53] Yasuhiro Suzuki, Kiyomasa Watanabe, Hisamichi Funaba, Satrou Sakakibara, Noriyoshi Nakajima, Nobuyoyshi Ohyabu, LHD Experiment Group, et al. Effects of the stochasticity on transport properties in high-β lhd. Plasma and Fusion Research, 4:036–036, 2009.

[54] Toshio Terasawa, Masahiro Hoshino, Jun-Ichi Sakai, and Tohru Hada. Decay instability of finite-amplitude circularly polarized alfven waves: A numerical simulation of stimulated brillouin scattering. Journal of Geophysical Research: Space Physics, 91(A4):4171–4187, 1986.

[55] P.W. Terry, D. Carmody, H. Doerk, W. Guttenfelder, D.R. Hatch, C.C. Hegna, A. Ishizawa, F. Jenko, W.M. Nevins, I. Predebon, M.J. Pueschel, J.S. Sarff, and G.G. Whelan. Overview of gyrokinetic studies of finite- β microturbulence. Nuclear Fusion, 55(10):104011, 2015.

[56] Martin S. Weidl, Dan Winske, Frank Jenko, and Chris Niemann. Hybrid simulations of a parallel collisionless shock in the large plasma device. Physics of Plasmas, 23(12):122102, 2016.

[57] J. Weiland and A. Hirose. Electromagnetic and kinetic effects on the ion temperature gradient mode. Nuclear Fusion, 32(1):151, 1992.

[58] G. G. Whelan, M. J. Pueschel, and P. W. Terry. Nonlinear electromagnetic stabilization of plasma microturbulence. Phys. Rev. Lett., 120:175002, Apr 2018.

[59] G. Zimbardo, S. Perri, P. Pommois, and P. Veltri. Anomalous particle transport in the heliosphere. Advances in Space Research, 49(11):1633 – 1642, 2012. Advances in theory and observation of solar system dynamics - I.